Design and Test Status of the SIS100 Dipole Magnet

E. Fischer
P. Schnizer

9. February 2010

GSI Helmholtzzentrum für Schwerionenforschung, Darmstadt, Germany
e.fischer@gsi.de
p.schnizer@gsi.de

Abstract

The SIS 100 will be the world's second fast ramped synchrotron for heavy ion research using superconducting magnets. In this report we summarise shortly the main results obtained on Nuclotron model magnets during the R&D period. We present the design choices made for the main dipole as well as its expected performance predicted on models verified by the measurement data obtained on the first full size dipole.

The main design components of the magnet are outlined. Special attention is given to demonstrate the intensive effort made to clarify the following crucial topics for safe and effective operation of the magnets: mechanical stability of the coil windings, magnetic steel, field design, temperature field, AC losses and the vacuum chamber. The complexity of the topic can not be given here in all detail due to the limited volume of the report. Full details are available in the referenced papers.

We conclude that the present dipole design is consolidated and near to series production. It will be finalised after building and testing the curved single layer dipole described here.

Contents

Acknowledgement

The authors are greatly indebted to all members of GSI and our collaborating institutes (JINR/Dubna, IHEP/Protvino, FZK/Karlsruhe) for their dedicated work.

Chapter 1

Introduction

SIS100 started of as an "back of the envelope" idea of: "adapting an existing superconducting machine" to the needs of the "Zukunftsprojekt" now known as the FAIR project. SIS100, as the work horse, could start on the rich developments, acquired during the Nuclotron project, and seemed to be just a copy, requiring only with small minor modifications. The different beam dynamics requirements (increased aperture, improved field quality) as well lattice layout (increased magnet length) soon showed that it was not a copy but rather a fully fledged new magnet development project. Sound R&D, not neglecting available options, showed that the required dipole can be designed and built, if one lets oneself lead by the ideas behind the original design choices, which let to the Nuclotron dipole, then by the chosen solutions.

Design principles

These design principles were:

- a simple magnet design
- a coil cooled by a two phase forced helium flow with low enough hydraulic resistance to provide sufficient cooling power for the superconducting coil as well as a sufficient temperature margin
- a straightforward robust magnet yoke design, but not neglecting the available options to minimise the AC loss.

The R&D started in 2000 with a hand-waiving analysis of the existing Nuclotron magnet design, followed by a model magnet built and measurement campaign of

about ten model modifications, next to qualifying commercially available programs and mathematical studies for calculating the expected magnetic field next to the AC losses [1, 2, 3]. Here fast progress was made changing the carbon steel brackets and end plates with stain less steel ones, followed by slits and minimising the coil end loop reducing the eddy current effects in the yoke laminations of the magnet end.

Considering the obvious hydraulic limits, even of the new wire and coil design, an improved high current cable was built next to a single layer dipole [4, 5]. However the author's design choice was not accepted in the first approach, leading to ready full size magnets, not able to provide the machine cycles required to satisfy the experimentalist demands of fast ramped cycles with an repetition rate of above 0.5 Hz up to the maximum field.

Nevertheless the built and tested full size model magnet allowed to verify the predictions (field strength, field quality, AC losses, temperature field, mechanical stability) and the excellent performance, which can be obtained for these superferric magnets [6, 7, 8, 9, 10]. In parallel the potential advantages of a magnet design based on a high current cable and on a single layer coil were continuously worked out and partially tested since March 2002 as summarised in chapter 8 (page 86).

After all this work the authors present the design of the dipole with all its features, its expected performance and show that this magnet is able to satisfy the requirements for SIS100.

Requirements

The requirements for the main bending magnets were:

- a field strength curvature of $B\rho$ = 100 Tm. (The particles in a synchrotron have to circulate. This product $B\rho$ depends on the particle momentum and is a constant).
- good field region: an ellipse with a = 57.5 mm b = 30 mm,

The required operation cycles are given in Table 1.1 and are depicted in Fig. 1.1 [11]. In addition, any other cycle with 4 T/s should be possible

As high charge state ions (Uranium up to U^{28+}) will be transported in these machines, the vacuum has to be better than 10^{-12} *mbar* [12]. So the vacuum chamber has to provide the following functionality:

1. a cold surface to work as an cryogenic adsorption pump to reach a vacuum pressure better than 10^{-12} *mbar* operating over 20 years, infinitely refreshable

Table 1.1: The main demanded operation cycles. $/\backslash$ ... triangular cycle, t_f ... flat top time, t_c ... cycle period

cycle	$B_{max}\,[T]$	$t_f\,[s]$	$t_c\,[s]$
1	1.2	0.1	1.4
2a	1.2	0.1	1.4
2b	0.5	0.1	1.0
2c	1.9	0.1	1.735
3a	1.2	1.3	2.6
3b	0.5	1.0	1.9
3c	1.9	1.7	3.4
4	1.9	0.1	5.0
5	1.9	0.1	5.0
$/\backslash$	1.9	0.	0.835

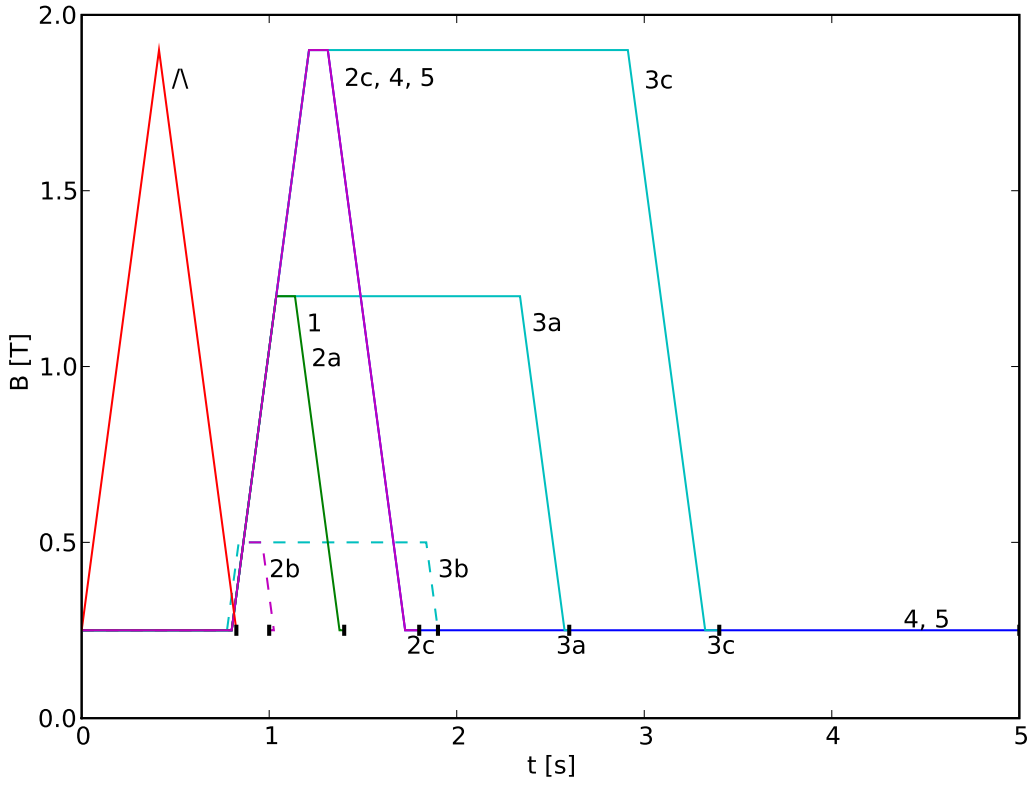

Figure 1.1: The cycles illustrated. The magnetic induction of the dipole is given versus the time.

2. minimise the eddy currents induced by the ramped field to an acceptable level so that the field distortion and the dissipated power are tolerable (by geometrical design and material choice)

3. be sufficiently mechanical stable to sustain a pressure of 1 bar so that a break of the vacuum pressure will not damage the whole machine
4. provide a return path for the beam image current
5. shield the beam from the outside (skin depth)

The vacuum chamber design was based on [13].

Chapter 2

Main magnet components

The principal design elements of a main magnet are: the coil with its end loops, the laminated yoke, the mechanical support structure consisting of the brackets and the yoke the helium headers and the beam pipe (see Fig. 2.1). Superferric accelerator magnets are built of a coil with its cooling channels, the field forming iron yoke, the

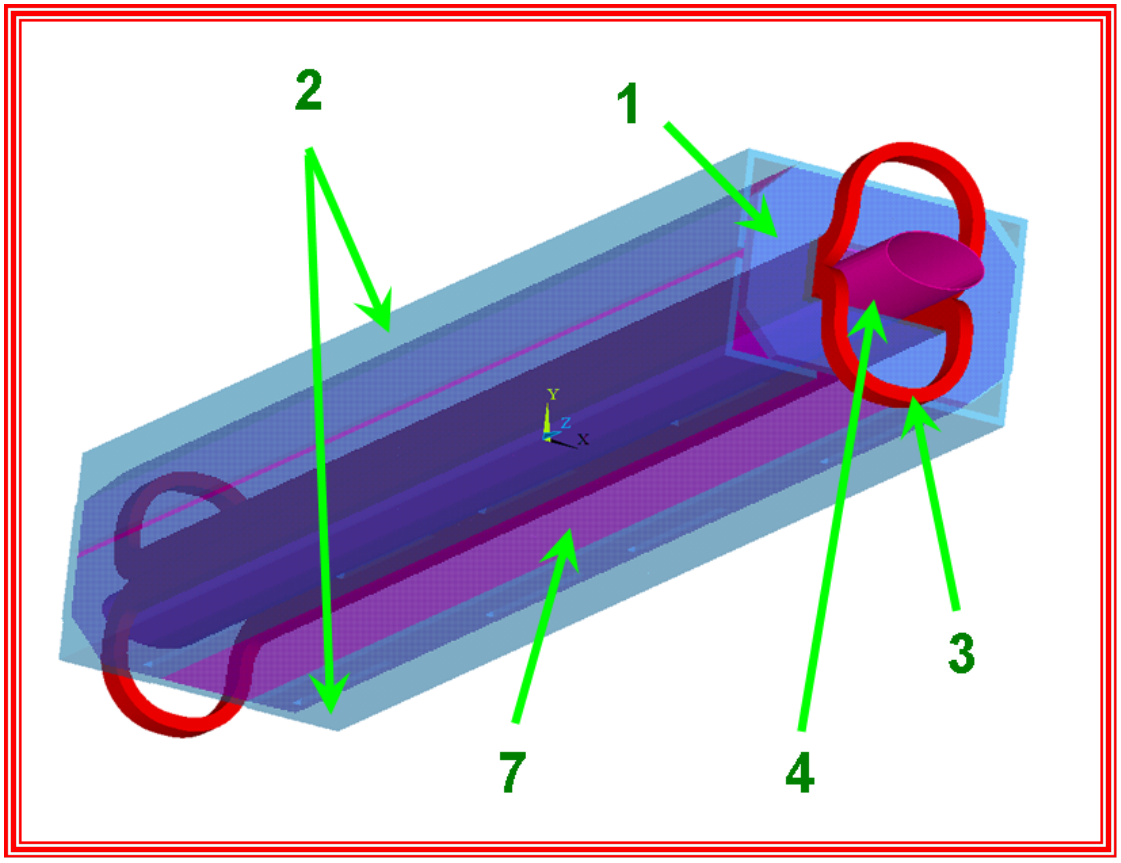

Figure 2.1: Components of a magnet illustrated on an ANSYS model. 1 – yoke end plate, 2 – brackets, 3 – coil end loop, 4 – beam pipe, 7 – laminated yoke

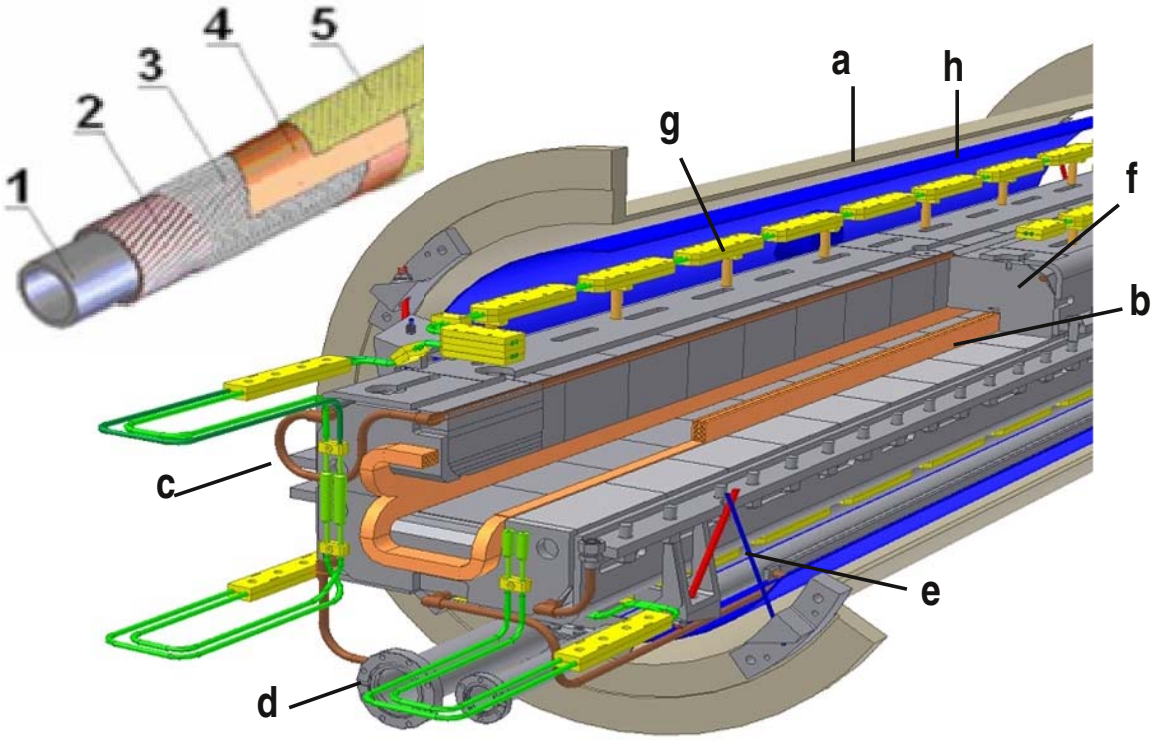

Figure 2.2: The structure of the Nuclotron cable (inset top left) and the main features of the magnet design of the first full size dipole. 1 – cooling tube, 2 – superconducting wire (multiflament NbTi/Cu), 3 - Nichrome wire, 4 – Kapton tape, 5 – adhesive Kapton tape, a – cryostat vessel, b – cable and half coil ($2 \cdot 4$ windings), c – yoke cooling pipes, d – LHe lines, e – suspension rods, f – soft iron yoke, g – bus bars, h – thermal shield

mechanical reinforcement structure consisting of the brackets and the end plates. Finally a beam pipe is inserted. The three bus bars for the quadrupoles as well as the one for the dipole are mounted on the magnet as these are built of superconducting cable as well (see Fig. 2.2).

2.1 Curved single layer dipole

The SIS100 main dipole is a curved magnet with a single layer coil with 8 coil turns (CSLD). Its main properties are listed in table 2.1. The cable is made of a Nuclotron type cable [14] (see table 2.2, inset in Fig. 2.2 and Fig. 2.3), i.e. a CuNi tube, cooled by a forced two phase helium flow, with superconducting wires wrapped around. The NiCr wire tightly fixes them to the tube. Layers of Kapton insulate the wire from the coil pack and the other turns. For SIS100 the coil windings (see Fig.2.4) are reinforced in a coil pack made of machined glass fibre epoxy. It is machined precisely so that it is well clamped by the wedge formed by the end of the pole

Table 2.1: The main parameters of the SIS100 main dipole

number of magnets	108 + 1 reference magnet	
design	window-frame, laminated cold iron yoke, lamination thickness 1mm, one layer with 8 turns	
max. field B_{max}	1.9	T
min. field B_{min}	0.23	T
bending angle	3 1/3	Deg.
edge angles (entrance / exit)	1.665 / -1.665	Deg.
orbit curvature radius, R	52.632	m
effective magnetic length, L	3.062	m
coil aperture	$165 \cdot 68$	mm^2
useable aperture	$120 \cdot 60$	mm^2
good field region	$115 \cdot 60$	mm^2
field quality target	600	ppm
current at max. field	12745	A
inductance	0.55	mH
ramp rate	4	T/s
cycle 2c		
cycle length	1.735	s
high field flat top duration	0.1	s
low field flat top duration	0.8	s
Total AC loss per @ 4.2K per magnet (cycle 2c)	50 ± 5	W
overall magnet length (slot length)	3.3	m
overall width (cryostat)	1.0	m
overall height (cryostat)	1.0	m
overall weight	1850	kg

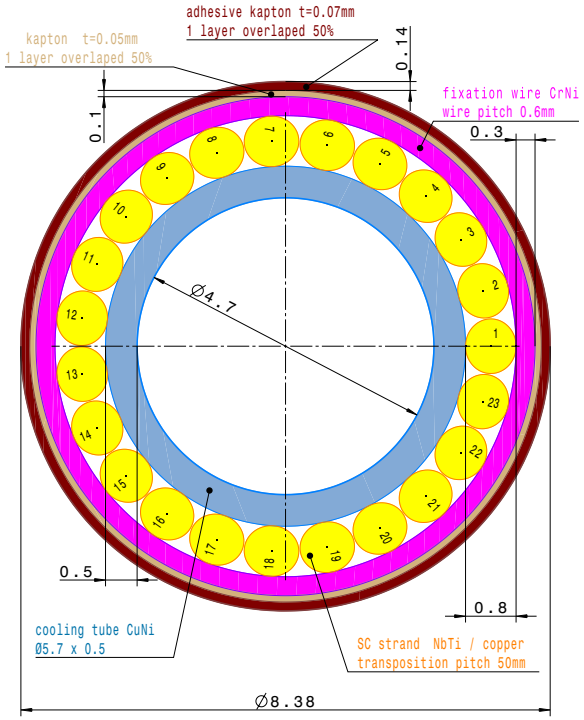

Figure 2.3: The high current cable for the curved single layer dipole.

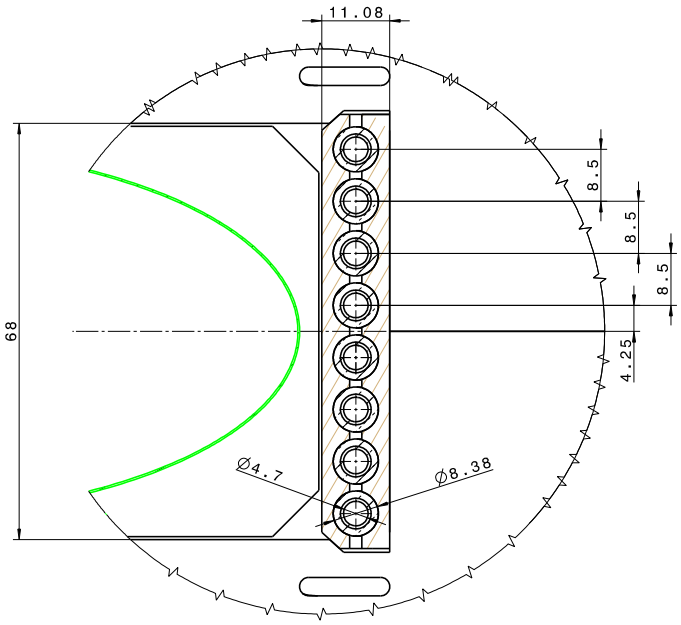

Figure 2.4: Zoom of the aperture of the magnet. The individual coil turns (8 in a single layer) are visible next to the G11 reinforcement structure and the shape of the yoke firmly holding it in place.

Table 2.2: Main parameters of the dipole cable

strands			
number of strands		23	
transposition pitch		50	mm
critical current @ 2.1 T, 4.2 K		19840	A
cooling tube			
material		CuNi	
outher diameter		5.7	mm
wall thickness		0.5	mm
insulation			
1^{th} insulating layer	with epoxy impregnation		
material	Kapton	tape	2 layers
thickness / layer		50	μm
2^{nd} insulating layer	with epoxy impregnation		
material	Kapton	tape	2 layers
thickness / layer		70	μm
wire			
strand diameter		0.8	mm
filament diameter		≈ 3	μm
number of filaments		32831	
filament twist pitch		6	mm
superconducting material		NbTi	
matrix		Cu/CuMn	
matrix to superconductor ratio		1.4	
linear wire resistance	$T_L = 10K$	2.05	$m\Omega/m$
linear wire resistance	$T_L = 293K$	69	$m\Omega/m$
fixation of the strands			
material	CrNi wire		
diameter		0.3	mm
transposition length		0.6	mm
coating	epoxy compound		
critical current density J_c @ 5 T, 4.2 K		2550	A/mm^2
critical current density J_c @ 2 T, 4.2 K		4600	A/mm^2

(see Fig. 2.4). A 3D view of the coil support structure is shown in Fig. 2.5 and in Fig. 2.6 the coil within the support structure. The coil ends will be supported by a G11 reinforcement as well (similar to [1, 15, 16]).

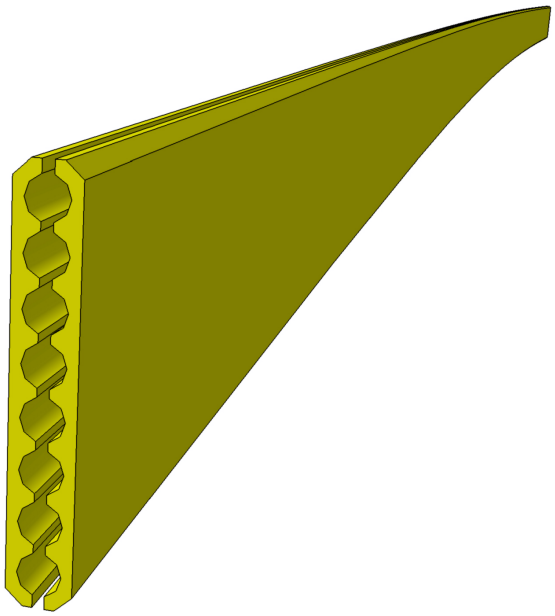

Figure 2.5: 3D view of the coil support structure

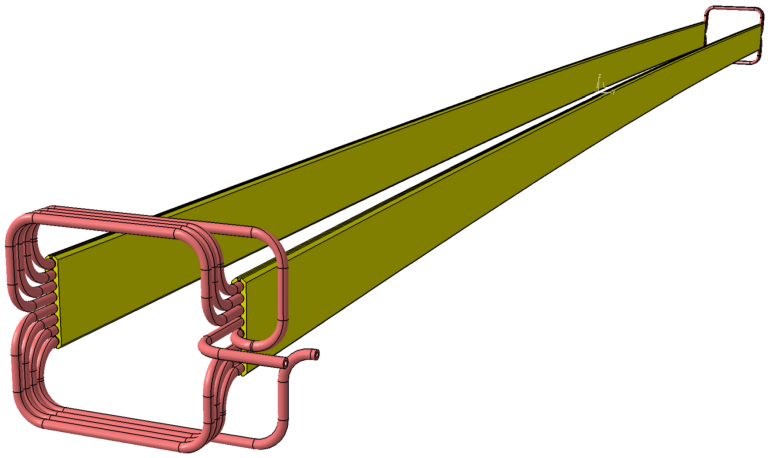

Figure 2.6: 3D view of the coil support structure with the coil inside

The 2D lamella is given with all its details in Fig. 2.7. The lamellae in the end of the yoke are slitted to reduce the AC losses (see Fig. 2.8). The expected 2D and 3D field strength and quality are described in chapter 5 page 55 (see also Figs. 5.1 to 5.3 page 58). The AC losses are described in section 6.4.2.

The cross section in the middle is given in Fig. 2.9 and the whole magnet is

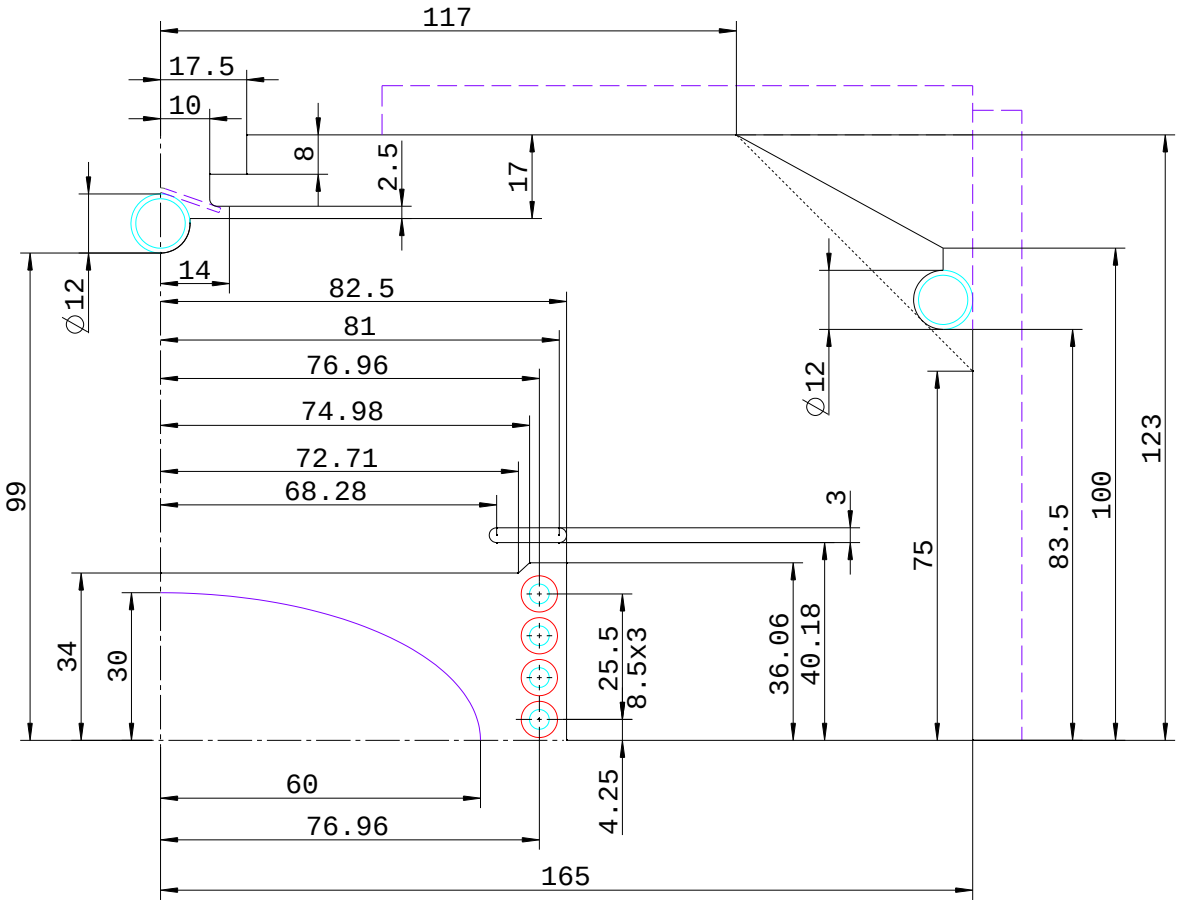

Figure 2.7: The lamella of the curved single layer dipole. (The dashed lines indicate the brackets (which are of stainless steel for SIS 100).

sketched in Fig. 2.10.

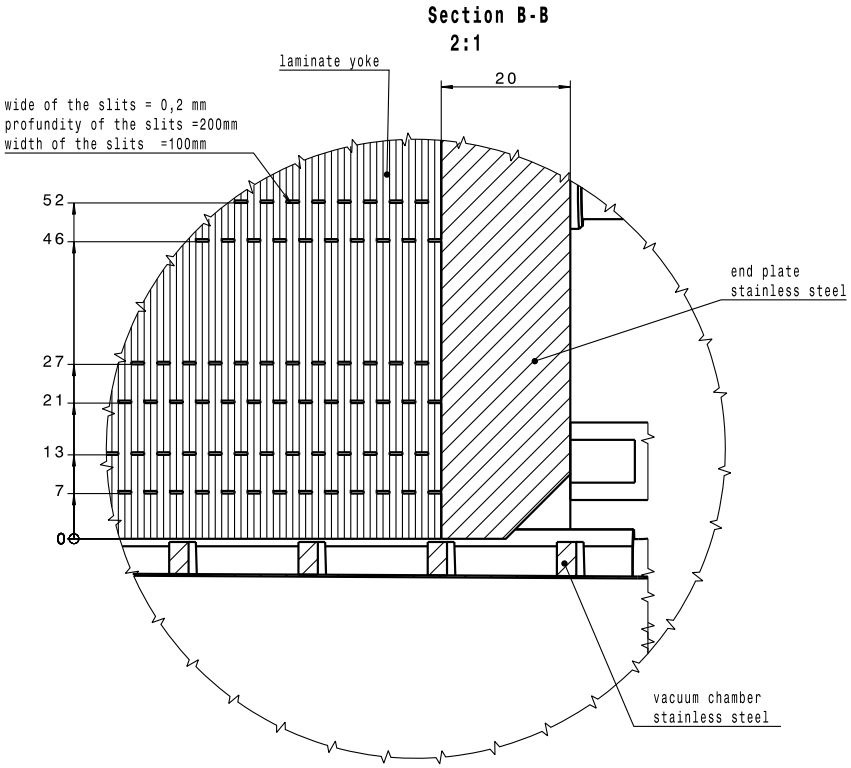

Figure 2.8: The end block design of the single layer dipole. The silts reduce the eddy currents in the end block significantly.

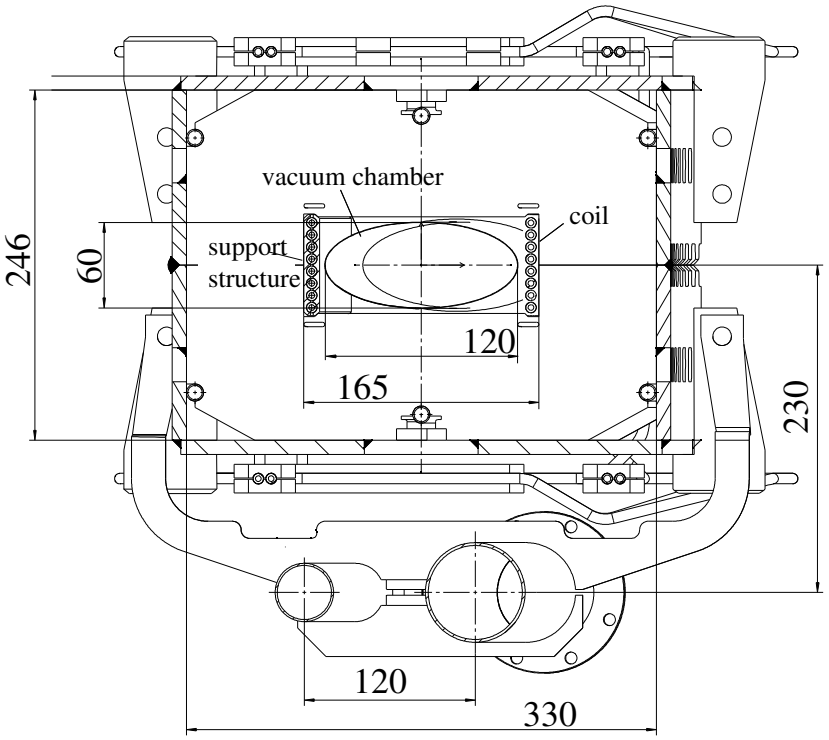

Figure 2.9: The cross section of the curved single layer dipole CSLD.

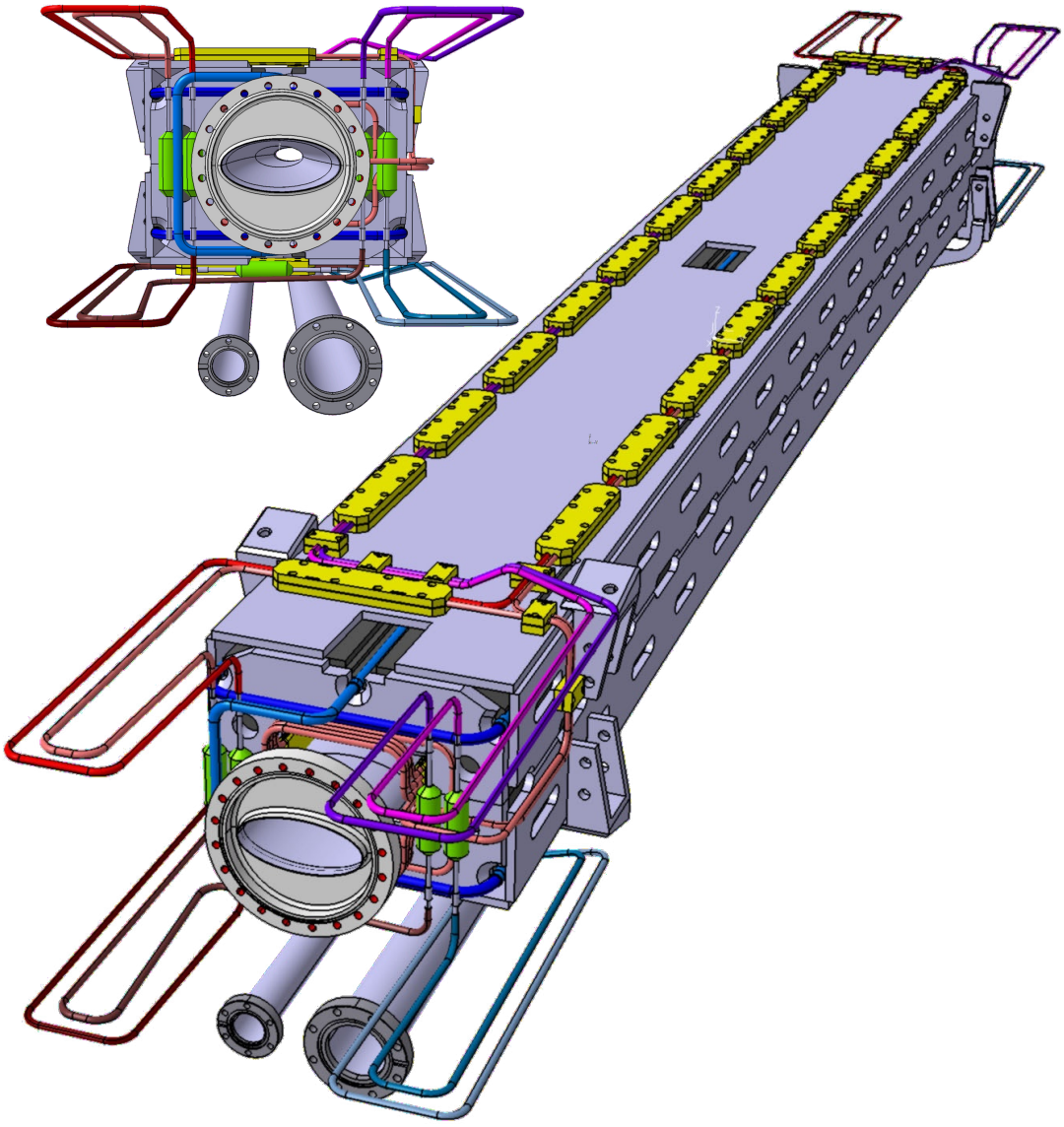

Figure 2.10: 3D sketches of the curved single layer dipole including the vacuum chamber (inset as seen form the front).

2.2 First full size dipole

Several small but interesting items are not yet designed in full details as these have to be done by the manufacturer. Therefore these items are presented as designed and fabricated for the first full size magnet.

The cable for the first full size dipole was fabricated with the cable machine newly installed at BNG (see Fig. 2.11). This machine features

- active and adjustable back rotation of the SC wire supply coils for all strands, avoiding torsion for all individual wires and for the cable,
- active control of the winding force (including emergency stop) for all strands to avoid wire break and to keep winding force constant,
- constant and adjustable torque (during operation) of CrNi wire spinning device to keep winding force of CrNi wire constant,
- insulation with polyimide tape (up to 8 layers, with to different pitches) online,
- flexible adjustment to different designs (number and size of strands, size of cooling tube, . . .),

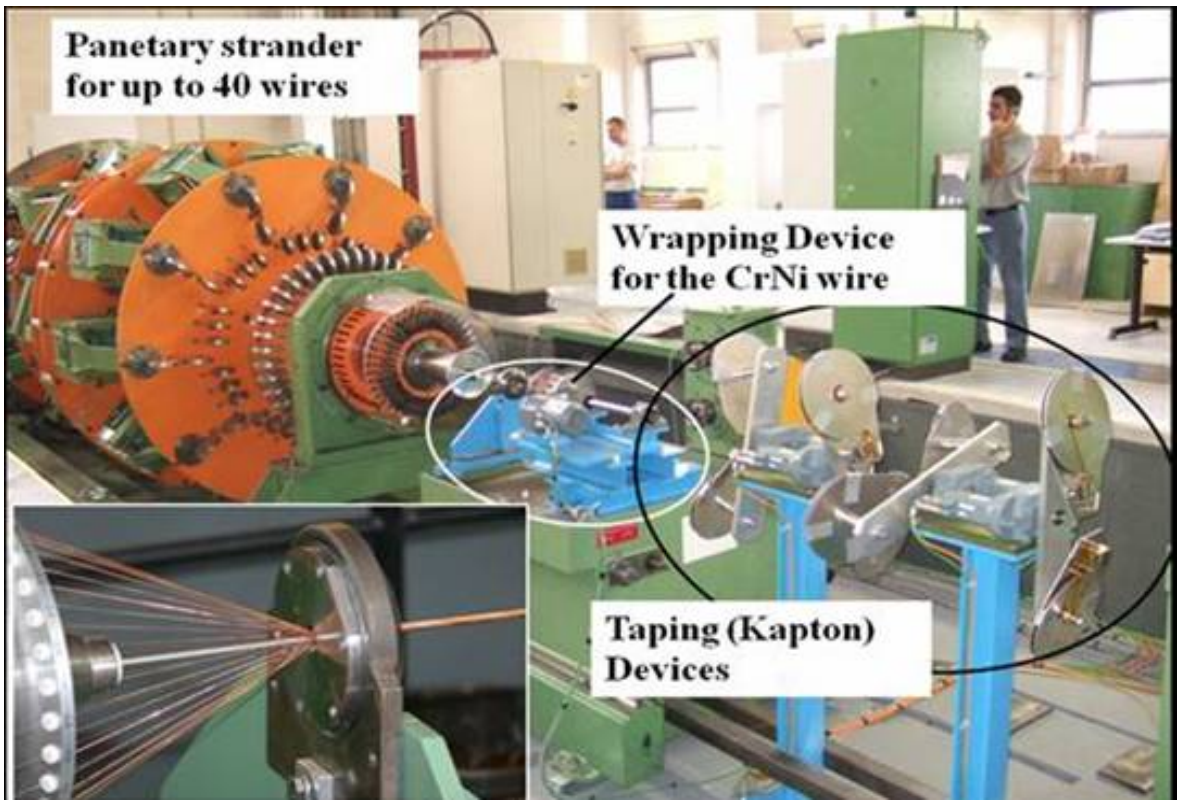

Figure 2.11: The cabling machine at Babcoeck Noell GmbH

- all actual machine values for winding forces, torques, speeds, and pitches can be recoded for the quality documentation.

The 2D lamella is given in Fig. 2.12 [17, 18].

The fabricated coil reinforcement is presented in Fig. 2.14. The coil end design is presented in Fig. 2.15 and Fig. 2.16. The coil ends during fabrication are given in Fig. 2.17. And the final magnet in its cryostat are given in Fig. 2.18.

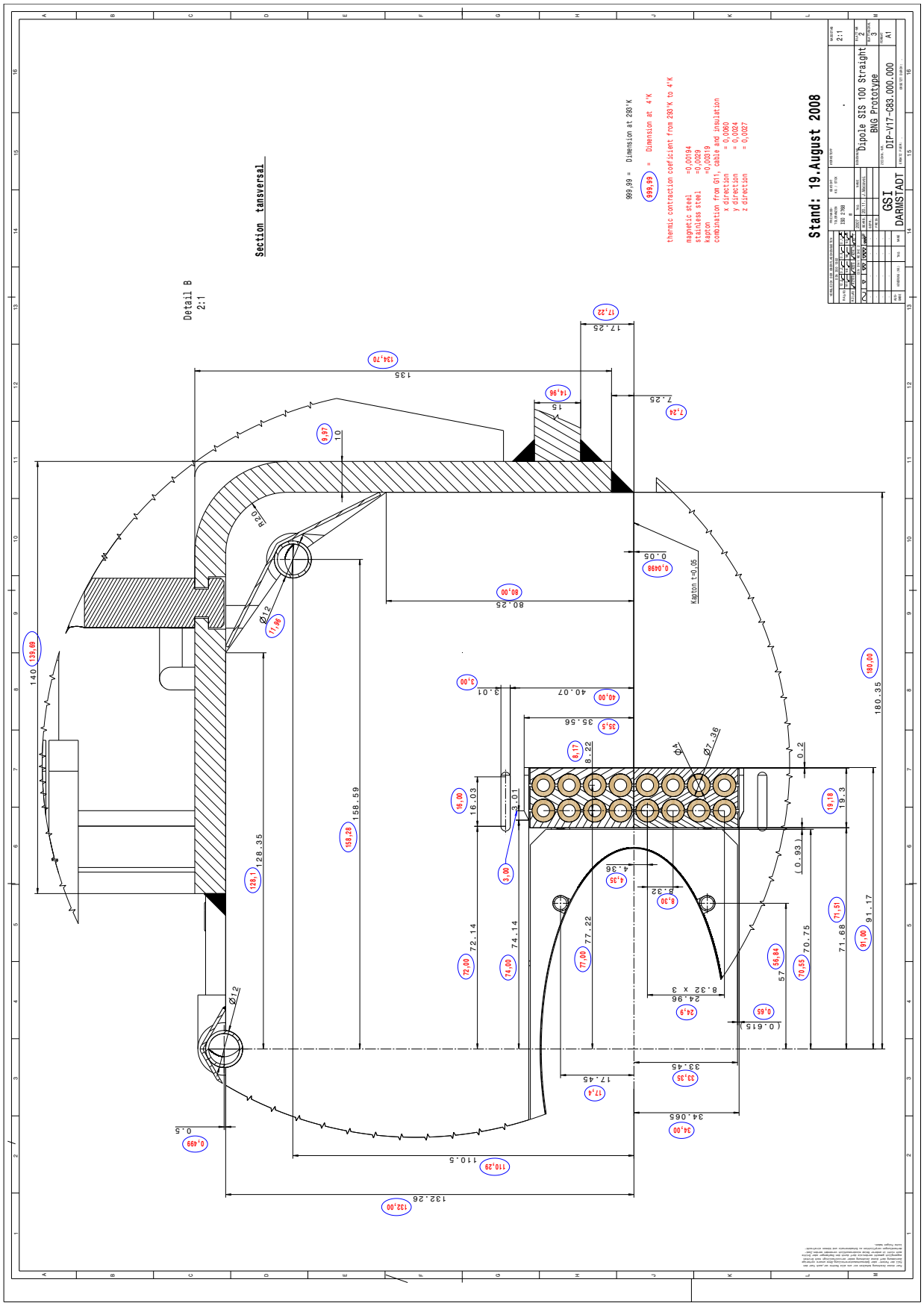

Figure 2.12: The lamella of the SIS 100 first full size dipole. The dimensions at cold are given in red.

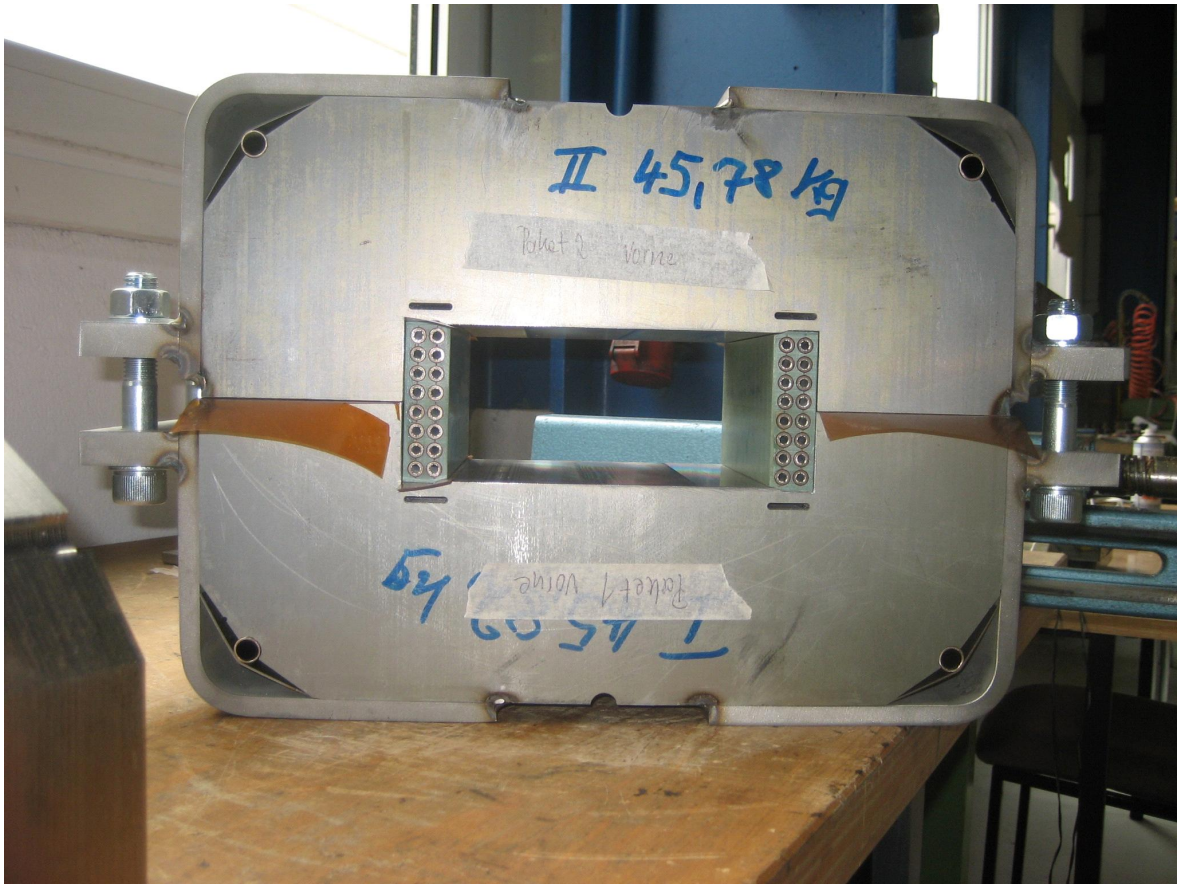

Figure 2.13: Photo of the cross section of the BNG magnet.

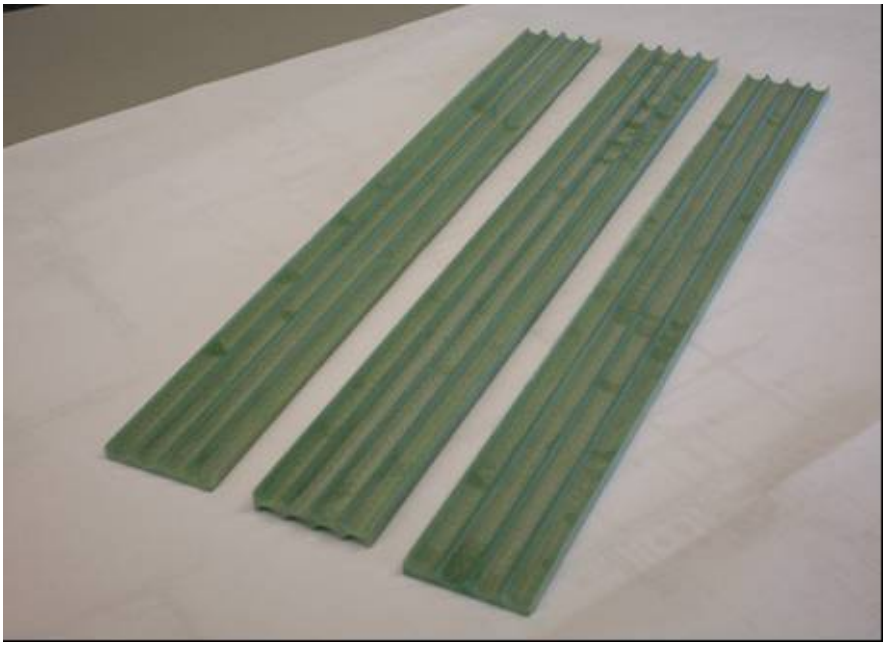

Figure 2.14: One of the combs forming the coil reinforcement.

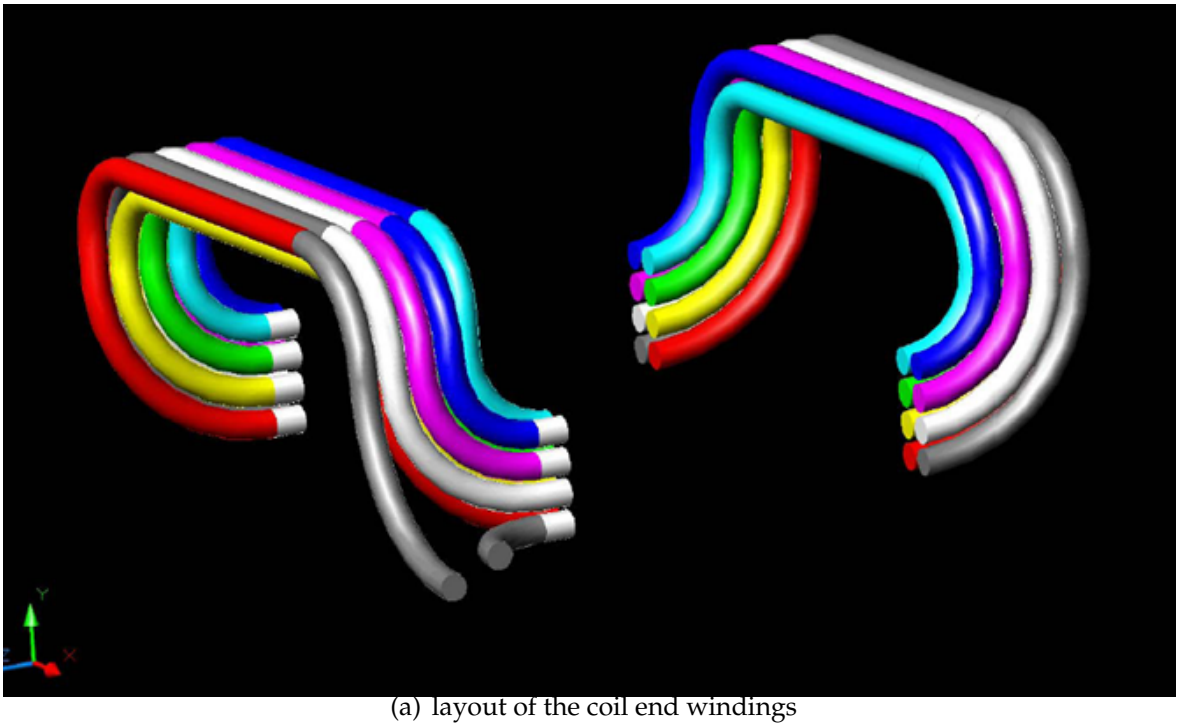

(a) layout of the coil end windings

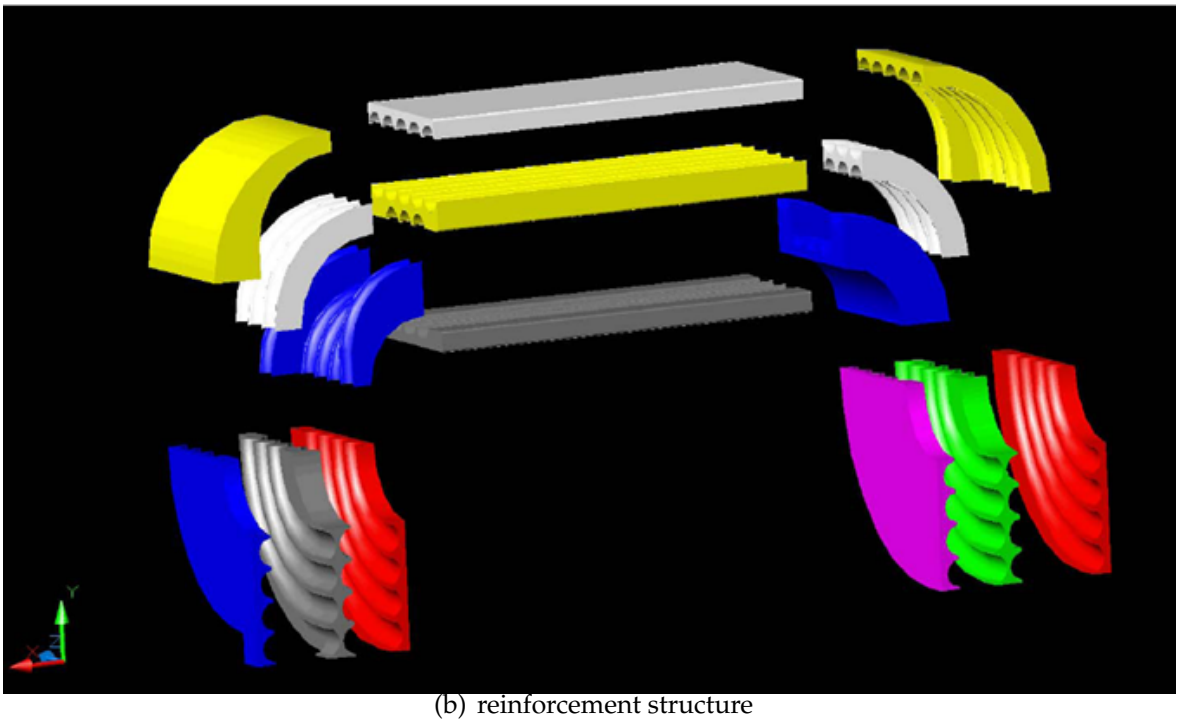

(b) reinforcement structure

Figure 2.15: The reinforcement structure of the coil end. CAD View. The individual windings are given on top while the associated pieces of the reinforcement structure are given at the bottom. Courtesy of Babcock Noell GmbH.

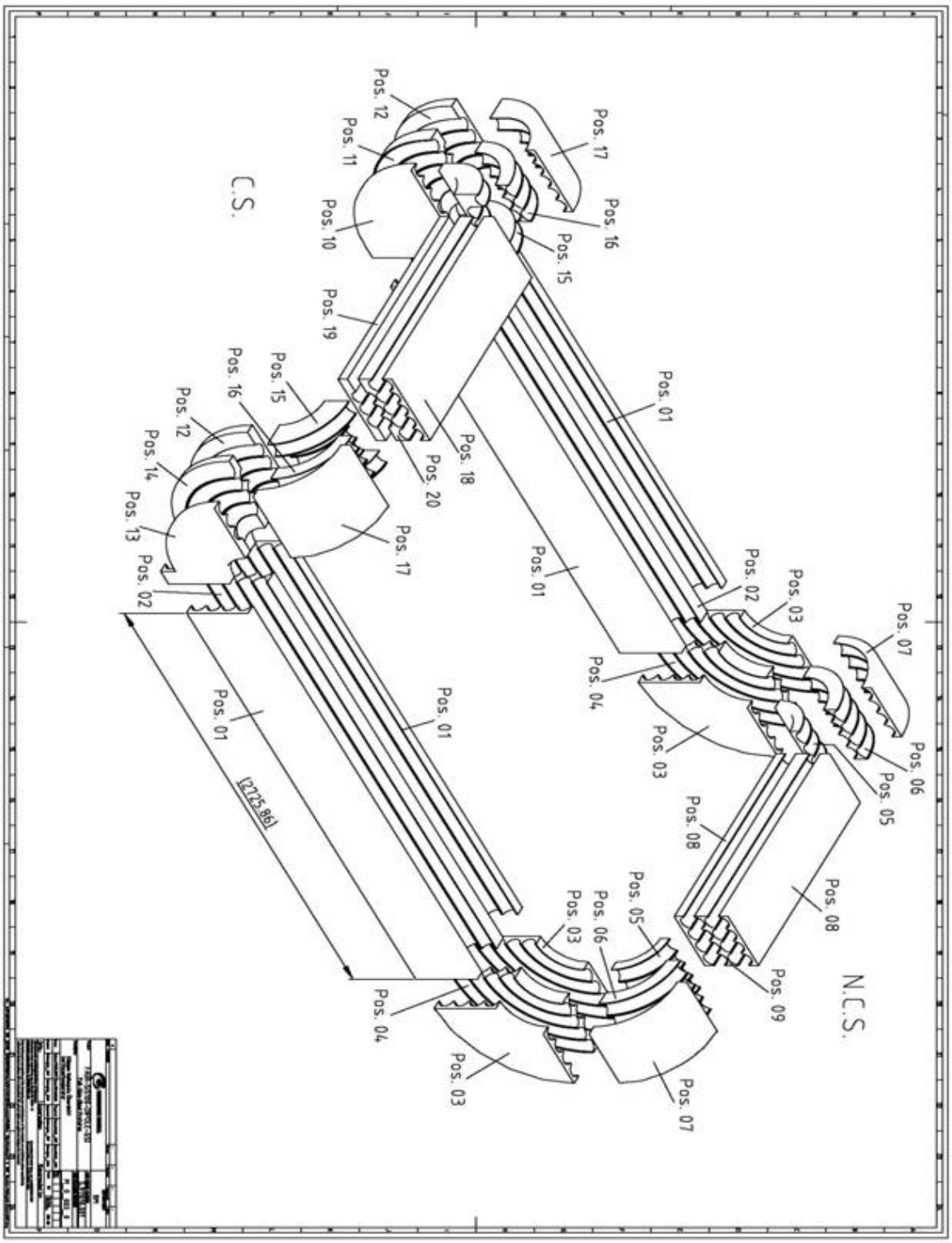

Figure 2.16: Coil end support structure drawing.

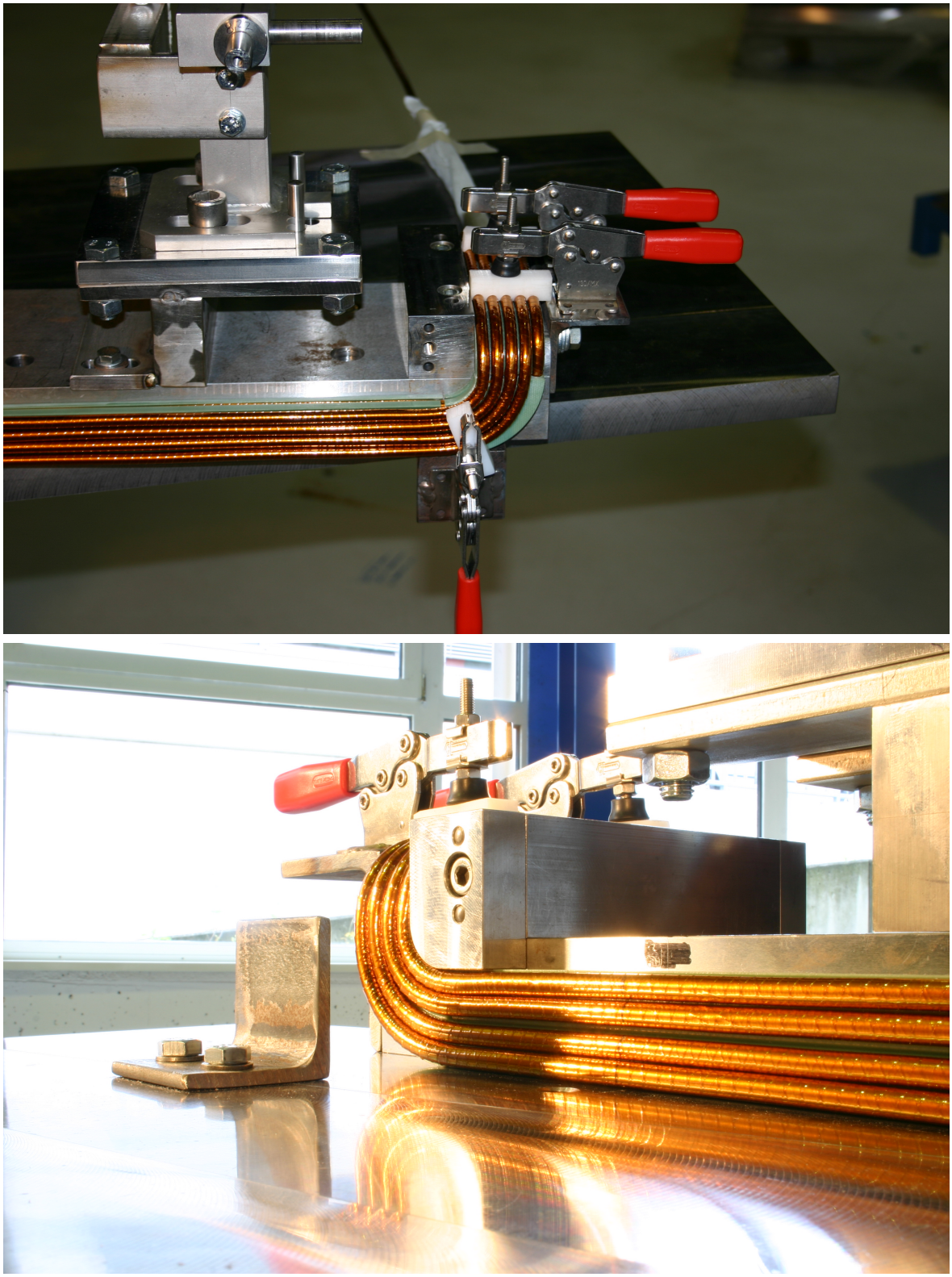

Figure 2.17: The coil ends during fabrication. One can see the coil winding (copper red) and its bend in the tooling. On top one can see the G11 structure (green) behind the winding. Courtesy of Babcock Noell GmbH.

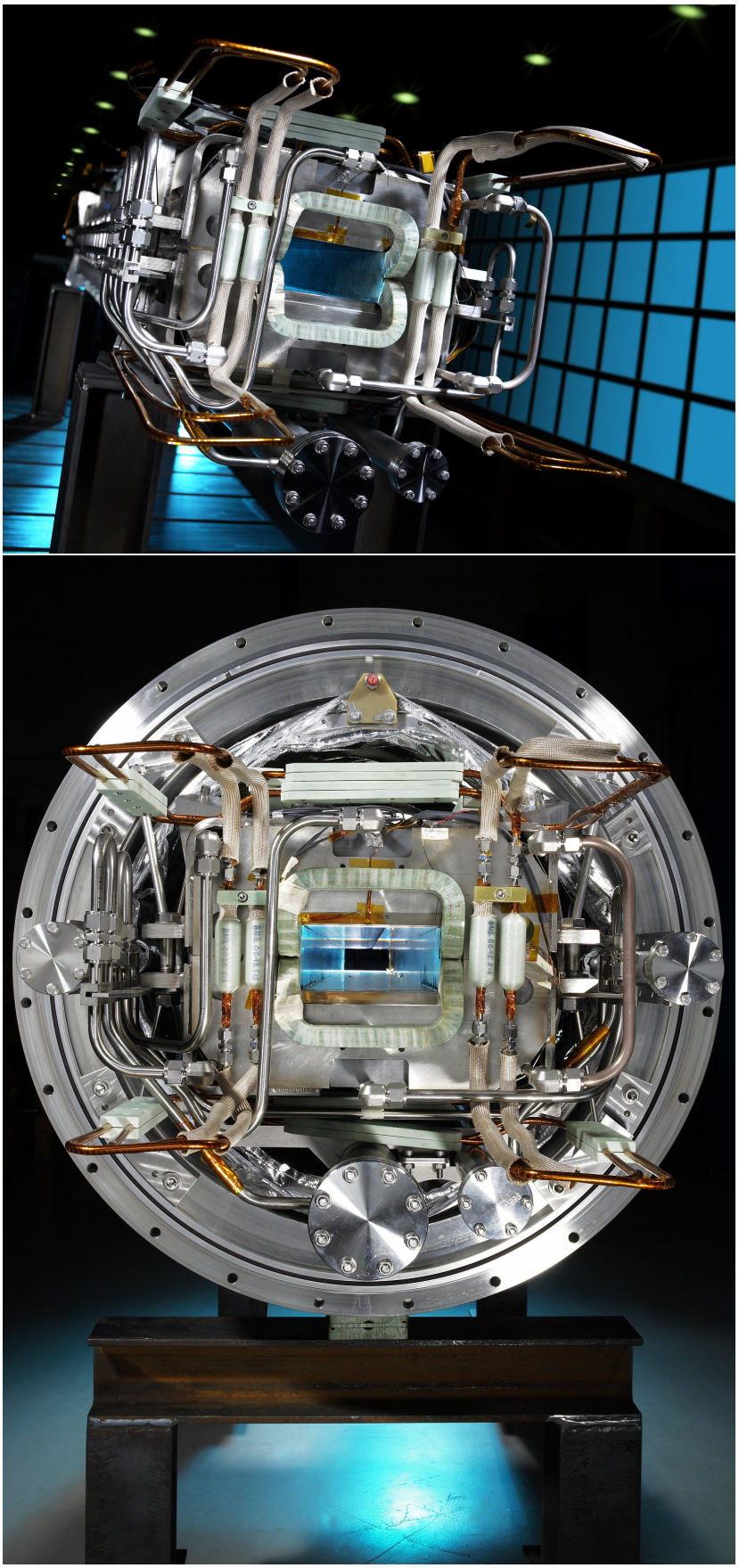

Figure 2.18: Photos of the first full size dipole magnet. Courtesy of Babcock Noell GmbH.

2.3 Built full size magnets: technological variations

3 Dipoles and 1 Quadrupole magnet have been built for SIS100. The first dipole was built by Babcock Noell GmbH (BNG, Würzburg). It is a straight dipole with a double layer coil. The isotropic steel M700-100 was used for the yoke (lamination thickness 1 mm).

A second straight dipole with the same dimensions as the one built by BNG was manufactured by the Joint Institute for Nuclear Research (JINR, Dubna). The yoke was fabricated using the anisotropic steel ET3414 with a lamination thickness of 0.5 mm.

The third dipole was fabricated by the Budker Institute for Nuclear Physics (BINP, Novosibirsk). The dipole yoke is curved and fabricated using the anisotropic steel ET3414 with a lamination thickness of 0.5 mm.

Further a quadrupole was manufactured by JINR using the the anisotropic steel ET3414 with a lamination thickness of 0.5 mm.

Chapter 3

Mechanical stability of the coil windings

3.1 Investigation of the cable mechanics

The following measurements were conducted:

1. fatigue crack growth rate of the CuNi-material.
2. thermal expansion coefficients
3. tensile strength at 4K and 300K
4. leak test after mechanical load
5. G11 material of the coil support structure modulus in different directions
6. stress-strain curves before and after 2 million cycles
7. leak test before and after 3 million cycles
8. thermal expansion coefficients and leak test before and after thermal cycles

The material presented here was published in [16, 19, 20].

Paris law

Paris law relates the stress intensity factor range to sub-critical crack growth under a fatigue stress regime. Some material is loaded periodically. Then one defines the

$$\Delta K = K_{max} - K_{min} \tag{3.1}$$

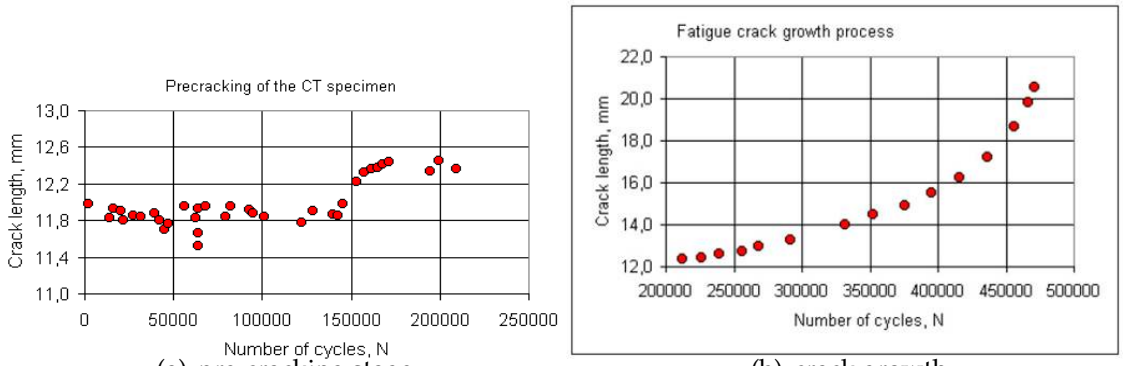

(a) pre-cracking stage (b) crack growth

Figure 3.1: Measurements on the fatigue crack growth at 7K. The left shows the obtained crack growth readings as red plots during the pre-cracking stage. On the right the obtained crack growth is shown as as red plots during the crack propagation stage of the measurement.

as the range of the stress intensity factor (i.e. the difference between the stress intensity factor at maximum and minimum loading) with K_{max} and K_{min} are the maximum and minimum stress factor. Further one defines the initial crack length a_i and the critical crack length a_c at which fracture occurs.

These factors are related by Paris law

$$\frac{\mathrm{d}a}{\mathrm{d}N} = C\Delta K^m \,. \tag{3.2}$$

with $\mathrm{d}a = a_c - a_i$, N the number of load cycles, and C and m, material constants.

3.1.1 Fatigue test of CuNi material

This investigation is performed using an ASTM proportional compact tension specimen with the size 45 mm · 43 mm · 4 mm and a starting a/W (a is the crack length and W is the width of compact tension specimen, which is 36 mm here) ratio of 0.33. Figure 3.1(a) shows the pre-cracking of the electro discharge notched specimen at 7 K. From the obtained plots of Fig. 3.1 the fatigue crack growth rate of the material CuNi can be computed using a special software to determine the crack length/cycle versus cycle number performance. The results of this computation are shown in Fig. 3.2. The determined pre-exponential constant C with $9.28 \cdot 10^{-12}$ (mm/cycle) and the exponent m = 4.5 are the so-called Paris constants describing the stage II linear portion of the curve in double logarithmic diagram.

The load ratio ($\Delta K_{min}/\Delta K_{max}$) was held constant with 0.1 during the entire test procedure. The structural analysis following the determined results with the Paris

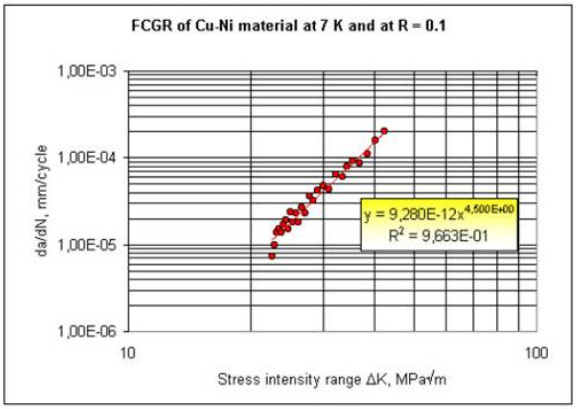

Figure 3.2: da/dN versus Δ K diagram of the CuNi material at 7 K.

coefficients can be ready applied to the tube enclosed inside the winding pack using the given boundary conditions as follows:

The life of a tube under cyclic loading is estimated by Paris law as given by ASM page 28

$$a_f = \frac{1}{\pi}\left(\frac{KIC}{\Delta\sigma YS}\right)^2 \tag{3.3}$$

with the input data $C = m/cycles = 9.28 \cdot 10^{-15}$, Y the geometry factor which 1.2 for surface cracks and S the safety factor set to 2. As initial crack length d is assumed to $0.2\,mm$. The "half size crack" is then $a_0 = d/2 = 0.1\,mm$. For the fracture toughness KIC a value of 50 MPa·m$^{1/2}$ is assumed as a worst case approximation. The number of cycles N_f is given by Paris Laws

$$N_f = \int_{a_0}^{a_f} \frac{1}{C\left(YS\Delta\sigma\sqrt{\pi a}\right)^m}\,\mathrm{d}a \approx 250 \cdot 10^6\,, \tag{3.4}$$

with $\Delta\sigma$ to 50 MPa which is 5 times the nominal pressure. So the tube will sustain more than 250 million cycles under the given conditions These computations show that a crack growth through the wall thickness of the tube during the lifetime of the magnet is more than unlike according to the present findings.

3.1.2 Thermomechanical tests

The stress strain measurements were done on samples (see Fig. 3.3), treated differently. The first (K_t) was annealed in Argon gas, the second (K_c) was measured after 100 rapid thermal cycles (80 to 300 K) and the third one was measured after annealing and 100 thermal cycles (K_v) (see Fig. 3.4 and Table 3.1). One can see that the

Figure 3.3: Test setup for the stress-strain measurement of the CuNi Tube

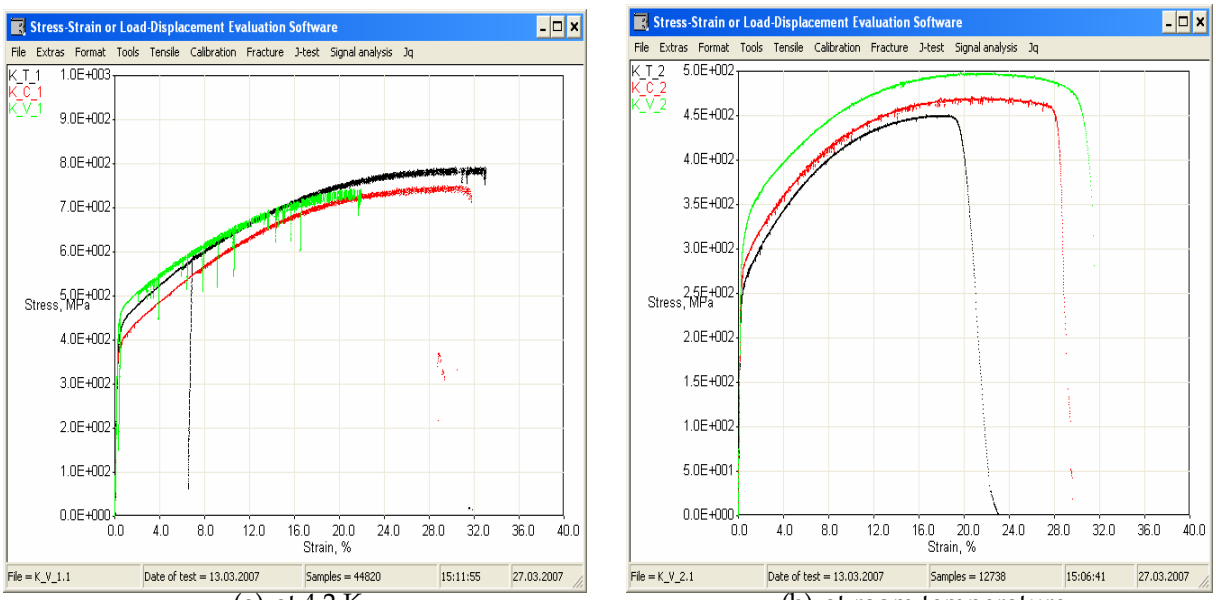

(a) at 4.2 K (b) at room temperature

Figure 3.4: Stress strain measurements on the CuNi Tube

Table 3.1: Stress Strain parameters for the different measurements. E-modul ... Youngs modulus, Y_S ... yield strength, UT_S ... ultimate tensile strength, E_U ... uniform elongation, E_T ... total elongation,

Measurement Sample	T [K]	E-modul [GPa]	Y_S [MPa]	UT_S [MPa]	E_U [%]	E_T [%]
K_t	4.2	163	414	792	32.1	33.1
K_t	RT	165	250	451	18.6	23.1
K_c	4.2	156	385	751	28.8	31.6
K_c	RT	154	274	471	21.8	29.9
K_v	4.2	161	379	743	21.0	21.9
K_v	RT	155	300	498	19.7	32.2

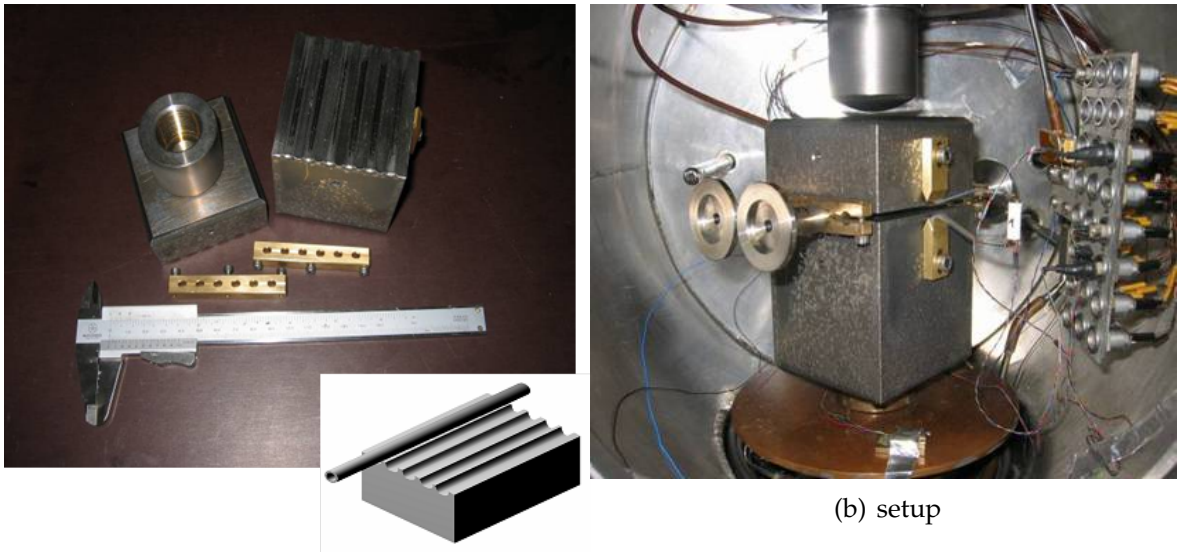

(a) sample holder

(b) setup

Figure 3.5: Setup of the leak tests.

Table 3.2: leak rate test for cycling with F_{max} = 800 N and T $<$ 7 K

sample	1	2	3	4	5	6	
before cycling	1.3	1.7	92	1.5	3.3	2.8	[10^{-9} mbar l / s]
after cycling	1.2	2.1	2.8	1.5	6	3.2	[10^{-9} mbar l / s]

stress and strains increase at cold and provides a significant large strength even if mistreated.

3.1.3 Leak rate measurements

The leak rate of the helium tube was tested before cycling it with F_{max} = 800 N, characteristic for the expected Lorentz forces, at T $<$ 7 K before and after $2.6 \cdot 10^6$ cycles (see Fig. 3.5 and table 3.2). At a level of 10^{-9} mbar $\cdot$ l/s no impact of the cycling on the leak rate was found for the NiCu-tube of the cable.

3.1.4 Fatigue calculations

As the magnet can not be tested on its $2 \cdot 10^8$ cycles, calculations were started to investigate the impact of the load cycles on the coil pack. The cable in its compound has been modelled in ANSYS in 2D. The results show that the tube will survive 20 years of operation [21]. For further analysis of the thermo-mechanical properties and physical accurate modelling 3D-ANSYS models of the cable were built to study

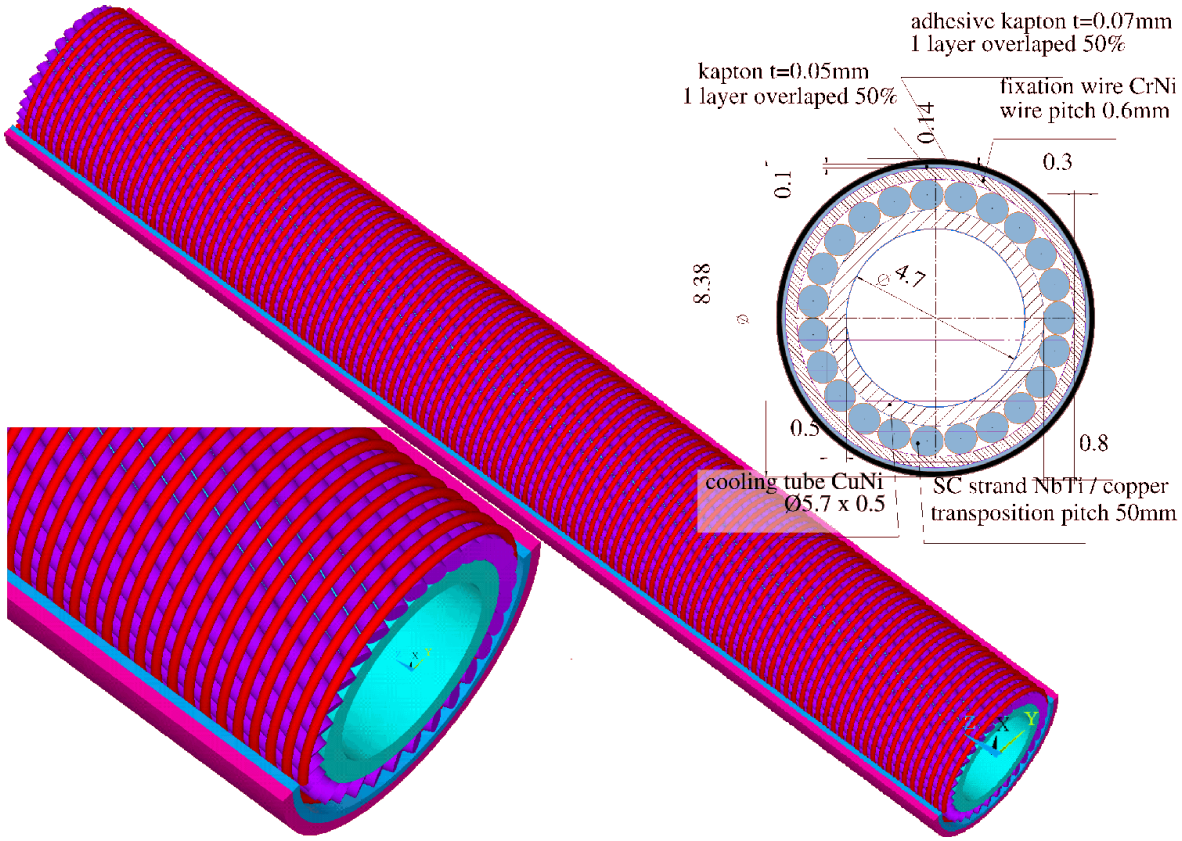

Figure 3.6: The FEM model of the Nuclotron type cable as used for the curved single layer dipole. On the top right the 2D design of the cable is shown. The full model is shown in the middle and on the left bottom a zoom of the model start.

in detail its structural integrity, and first trial calculations were started. We hope to report soon on the mechanical stability of the cable and the stresses and strains it will be exposed to [22, 3, 23].

3.2 Mechanical tests on the dipole coil

During the R&D phase the coil design was optimised for industrial cable production and higher coil stability [24, 25, 15]. A coil support structure made of G11 was introduced into the coil package to reduce the ”line” forces between the individual cable turns as well as to position them precisely. The mechanical properties of G11 specimens were measured along with the tests on mockups and test coils (see Fig. 3.7(b) and Fig. 3.8). Several tests were performed on samples extracted from a cable package. These tests are: thermal expansion in all three directions (x, y, z) on the cable package itself and on G11 material extracted from the test coil. This test coil was thermocycled before (room temperature → 4K → room temperature).

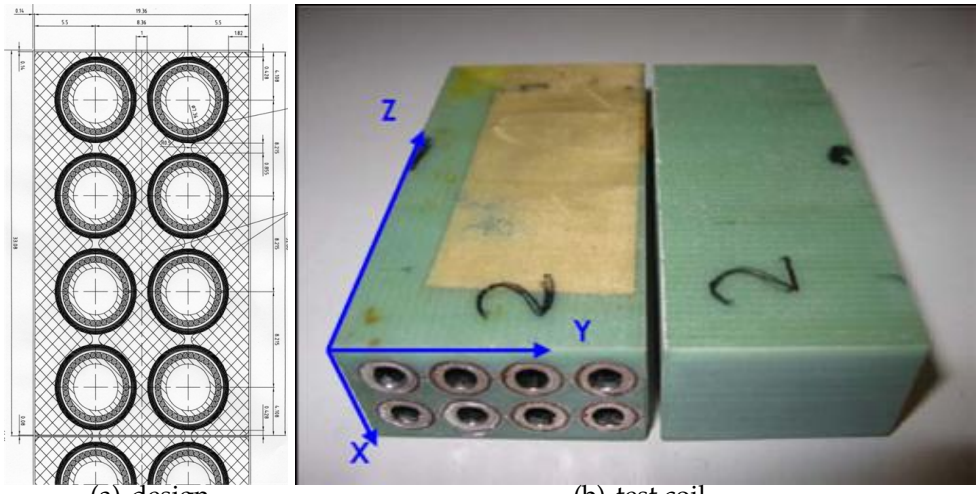

(a) design (b) test coil

Figure 3.7: The cable support structure. The left shows the design and the right shows a sample of the half coil ready for mechanical measurements after a first cool down.

Figure 3.8: Test of the support structure material.

Table 3.3: Compression modulus C_M and maximum Stress S_{max} of the coil pack

direction	C_M [GPA]	S_{max} [MPA]
x	35.2	699
y	20.9	1047
z	30.3	587

Fig. 3.9 presents the thermal expansion results.

Compression tests were performed on G11 material in all three directions. The compression modulus for G11 is given in Table 3.3. The Inter Laminar Shear Stress (ILSS) was investigated for the G11 material too (Fig. 3.10, and table 3.4). The stress strain behaviour was measured in x-direction of the cable package (see Fig. 3.7). A

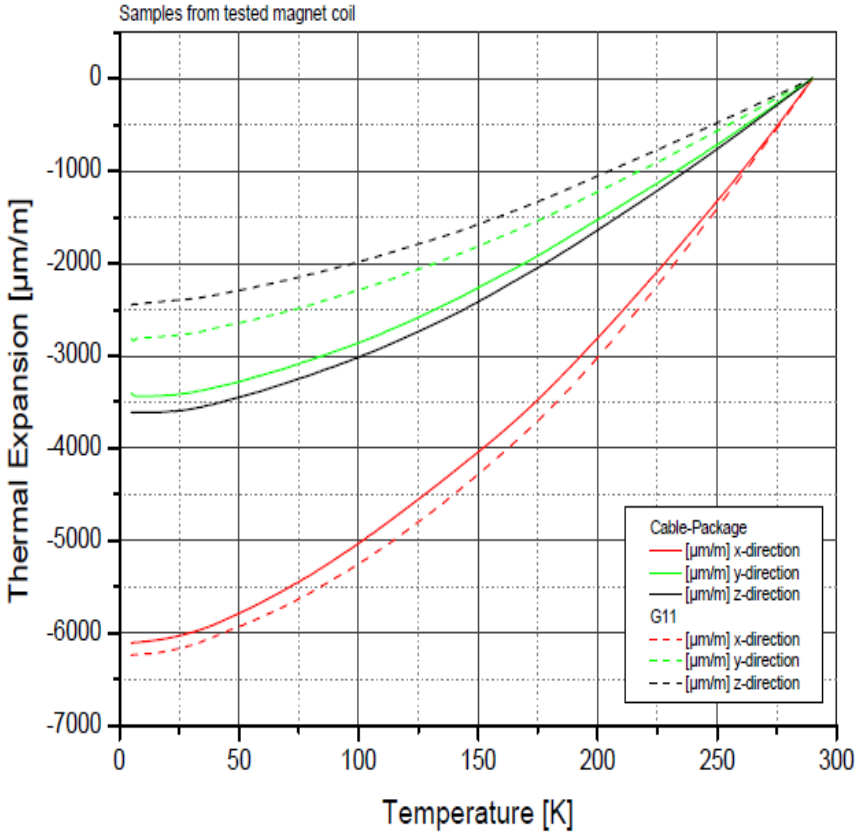

Figure 3.9: Measurement results of the thermal expansion for the coil pack.

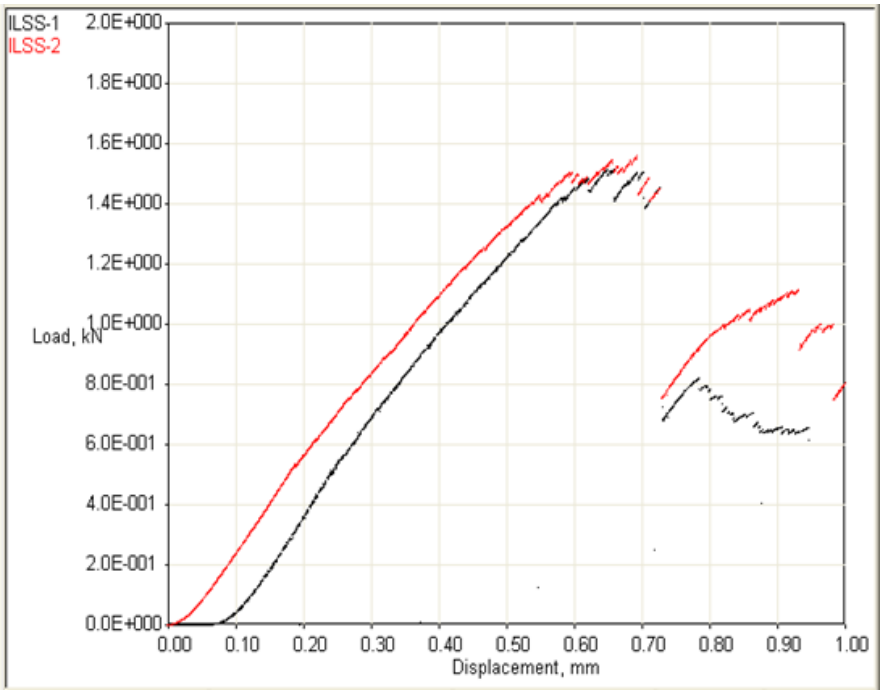

Figure 3.10: Measurement of the interlaminary shear stress

Table 3.4: Flexural modulus and shear stiffness

sample	T [K]	Stiffnees [MPa]	E-modul [GPa]	F_{max} [N]	ILSS [MPa]
sample 1	7	162.8	32.9	1.515	57.8
sample 2	7	163.9	33.1	1.559	59.1

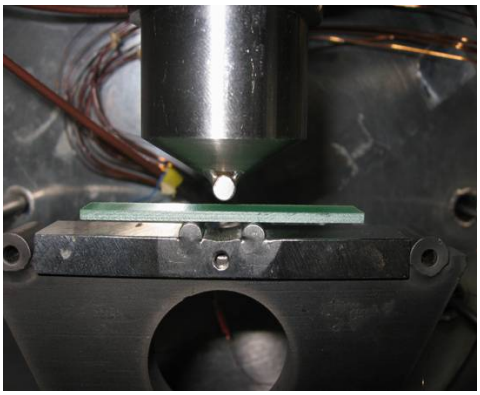

Figure 3.11: Measurement setup for measuring the flexural modulus

Table 3.5: The stiffness of the coil pack measured for two samples at room temperature and at cold. P_{max} = 2 MPa equals 9.3 kN for the sample area of 4650 mm^2.

	temperature [K]	stiffness @ P_{max} [kN/mm]	CuNi Tube @P_{max} [μm / kN]
WP2SRT	295	561	0.238
WP2SRT	295	509	0.235
WP-ST1	7	453	0.209
WP-S4-7K	7	440	0.285
WP-S5-7K	7	493	0.261

second sample was fatigue tested, examining the He-leak before and after thermal and mechanical cycling. The flexural modules was tested as well (see Fig. 3.11 and table 3.4). The method is described in [26].

3.3 Coil pack test

The thermal expansion of the coil pack was measured (see Fig. 3.12 for the setup) at room temperature (marked with "S2RT" and "S3RT"), at cold before cycling (marked with "ST1") and after cycling ("S4-7K" and "S5-7K") (see Fig. 3.13). The measured stiffness is summarised in table 3.5. The leak rate before fatique test was $2 \cdot 10^{-10}$ to $4 \cdot 10^{-10}$ mbar l/s and increased modestly to $5 \cdot 10^{-10}$ to $8 \cdot 10^{-10}$ mbar l/s. The stiffness of the coil pack is a bit lower at low temperature. The coil

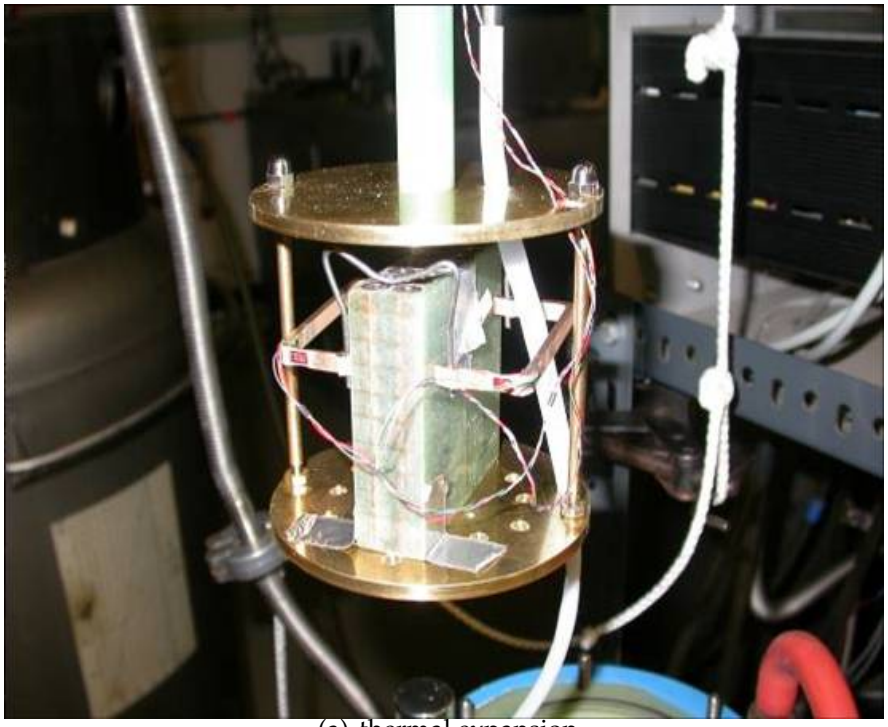

(a) thermal expansion

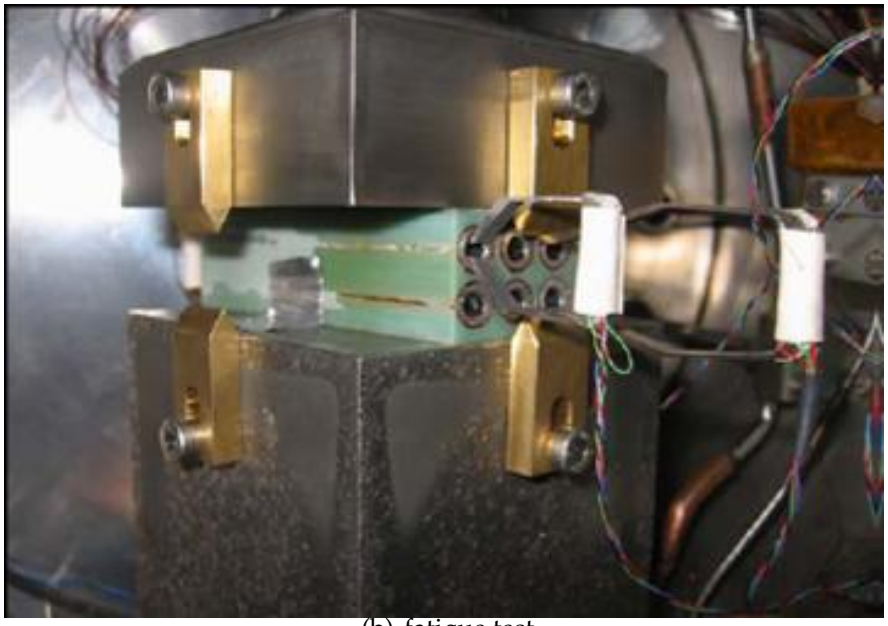

(b) fatique test

Figure 3.12: Thermal expansion and stress-strain measurements on the coil pack.

pack was stress-strain cycled for $\approx 10^6$ cycles for an force of up to 2 MPa (Lorentz force) and afterwards destructively tested. For the cycling a compression modulus of 5.8 GPa was found while for the destructive test a compression modulus of 4.8 GPa was found. This gives a movement of less than 5 μm of the coil windings in the

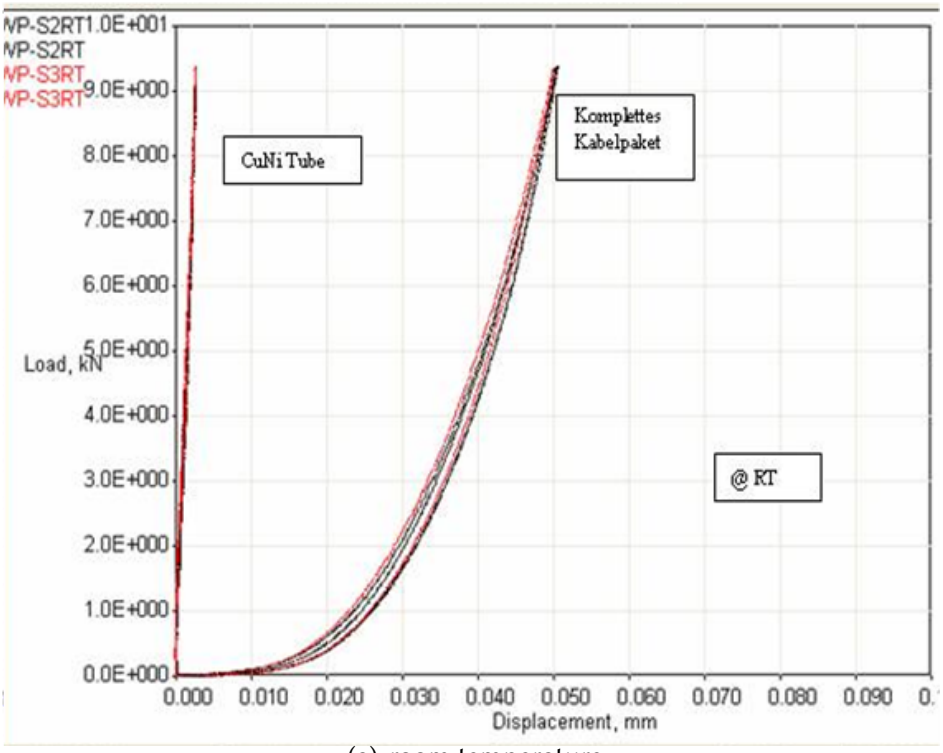

(a) room temperature

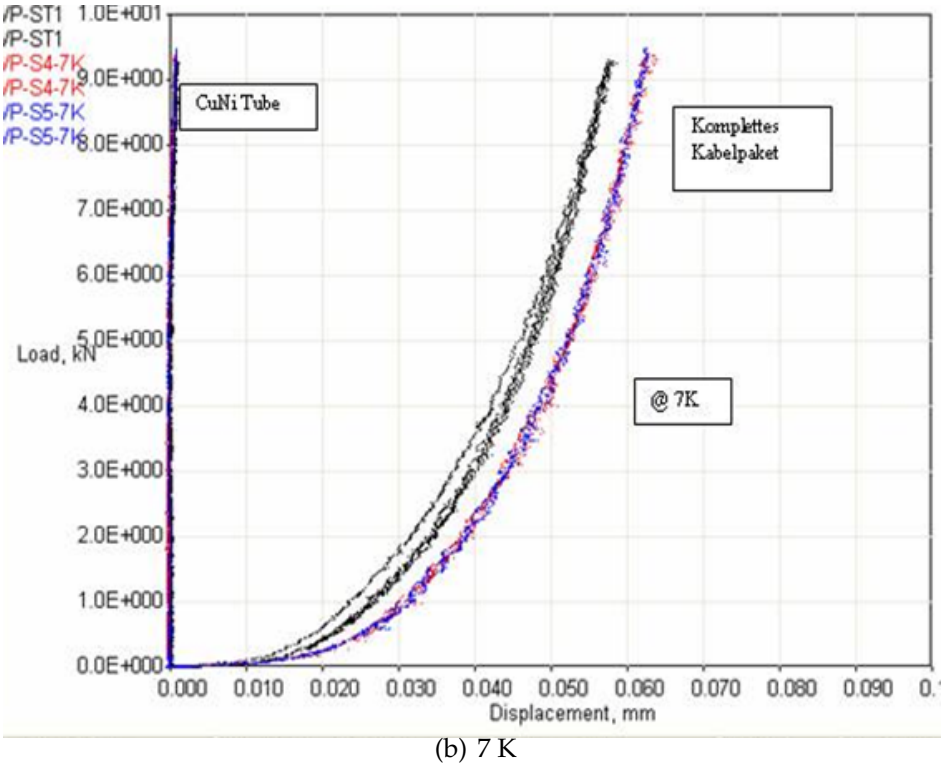

(b) 7 K

Figure 3.13: Measurement of the coil pack stiffness at room temperature and at 7 K. Komplettes Kabepaket . . . complete coil pack.

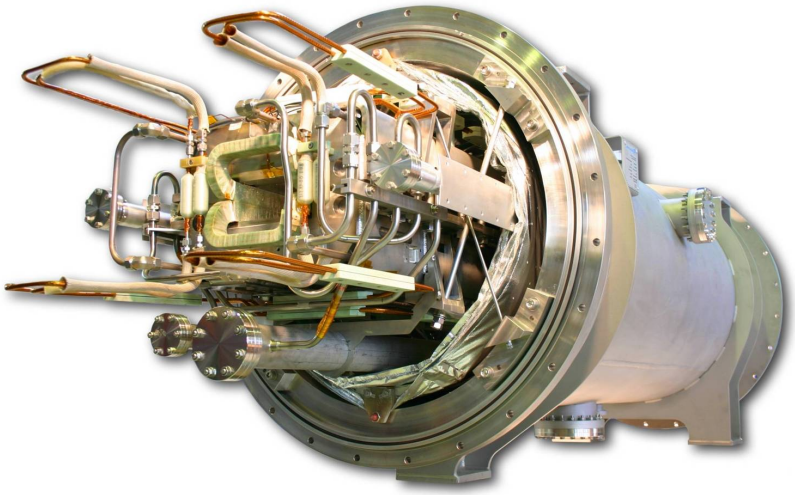

Figure 3.14: The first SIS100 dipole magnet within its cryostat

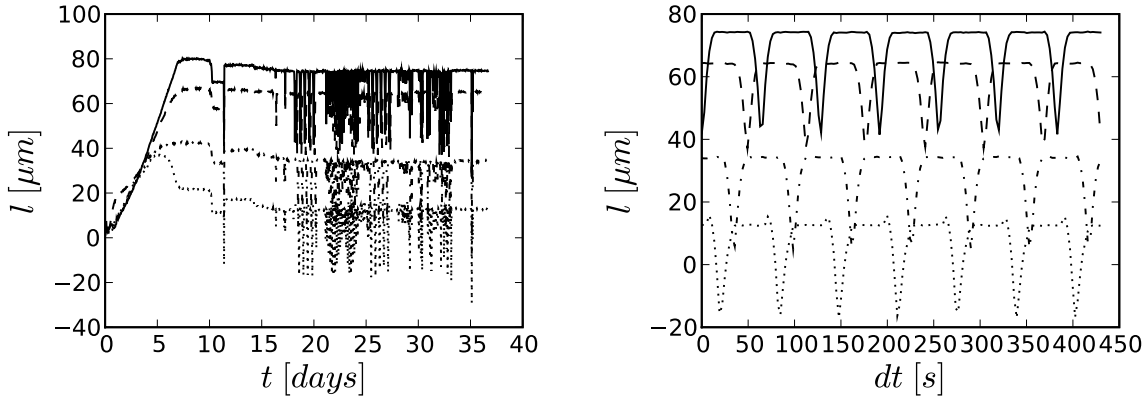

(a) coil movement; all

(b) coil movement; cycle

Figure 3.15: Movement of the coil end as measured on the magnet delivered by BNG during cool down and cycling.

magnet at maximum field.

3.4 Integral test results for the first prototype dipole magnet

The integral verification of the coil design was tested during measurements on our first BNG prototype dipole at GSI (see Fig. 3.14) [6, 8]. The movement of the coil ends versus the yoke was measured during cool down (see Fig. 3.15), as well as while cycling the magnet. The contraction factors of the coil pack (2.7‰) and the yoke

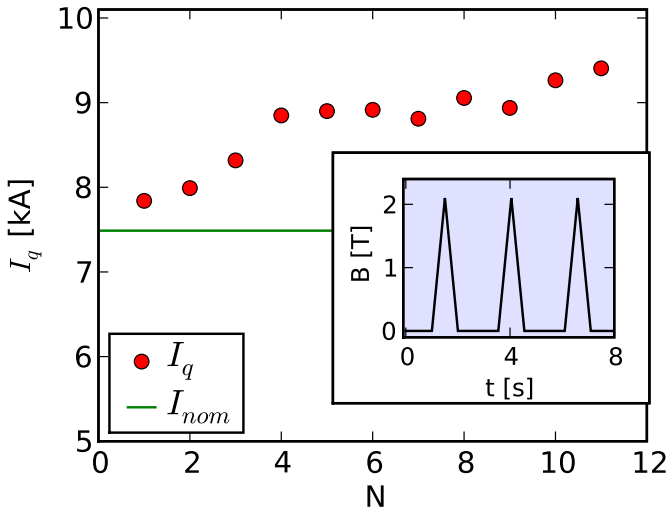

Figure 3.16: DC Quench training next to the maximum cycle of the magnet (insert).

(2.41‰) differ significantly, thus a effect during cool down is expected ($\approx 0.8mm$). One can see that the coil end moves only little versus the yoke $< 0.1\,mm$, which shows that the coil pack is hold firmly by the yoke and it does not move at all. This is safely in the elastic regime (which would allow a relative strain of tens of millimetre). The end movement of 20 μm during cycling is also very small.

The magnet had shown an excellent short training behaviour of the coil, high critical current (near to short sample limit), as well as its weak ramp rate dependence. These results are clear experimental proofs that the actual technology for cable and coil manufacturing is sound and ready for serial production.

3.5 Quench training and cycling

The magnet training curve is given in Fig. 3.16 with the first training quench above the nominal current. The ramp rate dependent training showed no significant decrease in the magnet performance. During the test campaign the magnet was 7 times thermocycled (room temperature $\rightarrow$ 4.5 K $\rightarrow$ room temperature) and was exposed to more than half a million power cycles. These results demonstrate experimentally that the new ”dry” technology for cable manufacturing is sound and ready for serial production.

Chapter 4

Magnetic steel

4.1 The main magnetic properties

Two parameters control the magnetic properties of steel at different parts of the B-H curve:

- H_c — before the knee, depends on the structure (Carbon and Si, annealing, heat treatment – temperature and duration, stress, strain, tension)
- M_s — after the knee (saturation); structure independent, only on the chemical content

Additionally the AC losses depend on W_h, the specific hysteresis losses, and on the specific electric resistivity ρ. For the symbols, used in this chapter, see table 4.1. This chapter is based on [27].

4.1.1 Simple mathematical models

Hysteresis and eddy-current create heat in the iron yoke. This heat is often also called "AC loss".

Table 4.1: Used Symbols

parameter	
ρ_d	density of steel
H_c	coercive force
μ_{max}	maximum permeability
M_s	magnetisation saturation
W_h	specific hysteresis losses
ρ	electric resistivity

Hysteresis losses

Hysteresis occurs due to non-linearities and differences in the magnetisation and demagnetisation of all ferromagnetic materials. When the magnetisation curve is taken through a complete loop the B-H envelope represents the hysteresis energy loss per unit volume that is dissipated as heat in the material per cycle time t_c

$$W_h = \int_{t_c} H \, \mathrm{d}B \tag{4.1}$$

This formula shows that hysteresis losses are proportional to the area of the hysteresis loop of the B-H curve. In general, the hysteresis losses are proportional to B_{max}^n for a definite iron material, where B_{max} is the maximum value of magnetic induction for a given cycle [28]. The index n is purely empirical and has no theoretical basis. It has been found by later experiments that this index varies between 1.5 - 2.5, depending on the quality of the iron material and on the value of the magnetic induction.

Experimental results of measurements of steels, used in the UNK magnets, give $n = 2$ in all range of induction with satisfactory accuracy. Thus the hysteresis loss in a unit volume of material is given by

$$W_h = c_h \, B_{\max}^2 = \underbrace{k_h \, H_C}_{c_h} \, B_{\max}^2 \, . \tag{4.2}$$

c_h is a constant for a given iron type, and depends on B_{max} and H_c, the coercive force. The constant k_h depends on the chosen units system and is in first approximation proportional to the steel's coercive force, which is sufficient to estimate losses of this type. So the AC loss power is proportional to the field amplitude and the field ramp rate $\mathrm{d}B/\mathrm{d}t$:

$$P_h = \frac{1}{2} \, k_h \, H_C \, B_{\max} \, \frac{\mathrm{d}B}{\mathrm{d}t} \, . \tag{4.3}$$

The previous two equations (4.2) and (4.3) show that it is necessary to reduce the coercive force H_C in order to decrease hysteresis losses.

Eddy-current losses.

Eddy-current losses are induced in iron by a varying magnetic field. The resulting B-H curve loop will be larger due to the eddy current effects. The eddy currents dissipate heat, which depends on the specific resistance of the material ρ. The dissipated power per unit volume of iron sheet with thickness d is expressed by [29]

$$P_C = \frac{1}{12\,\rho}\, d^2 \left(\frac{\mathrm{d}B}{\mathrm{d}t}\right)^2 . \tag{4.4}$$

The eddy-current losses per cycle with maximum induction B_{max} and field ramp rate $\mathrm{d}B/\mathrm{d}t$ are

$$W_c = \frac{1}{6\,\rho}\, d^2\, B_{\max} \frac{\mathrm{d}B}{\mathrm{d}t} . \tag{4.5}$$

There are two available parameters: thickness sheet d and specific resistance ρ, which can be used to reduce the eddy-current losses.

Therefore the following steps are required to reduce the loss created by the two effects

1. decrease the coercive field H_c,
2. increase the specific resistance ρ,
3. decease the iron sheet lamination thickness d.

4.1.2 Criterions of steel selection for superconducting magnets

Different steel is appropriate for AC and DC magnets. The magnetic properties of steels depend on their chemical composition, melting procedure, hardening process and heat treatment. The soft magnetic alloys must combine as many as possible of the following characteristics at moderate cost:

1. low hysteresis losses,
2. low eddy current losses,
3. high permeability at low field strength,
4. high saturation magnetisation M_S about 2.1 T,
5. no aging effects.

Some of these requirements are conflicting due to the nature of the steel and thus the optimum compromise must be found. Factors that influence the properties of soft magnetic materials are as follows:

1. alloying elements,
2. mechanical stresses, elastic and plastic strains.

Table 4.2: Dependence of main parameters on Si content (in percent)

parameter	approximation function	unit
saturation magnetisation	$M_s = 2.16 - 0.048 \cdot Si$	T
coercive force	$H_c = 120 - 30 \cdot Si$	A/m
resistivity	$\rho = 0.1 + 0.12 \cdot Si$	$\mu\Omega \cdot m$
density	$\rho_d = 7.865 - 0.065 \cdot Si$	$kg \cdot dm^{-3}$

3. magnetic annealing and heat treatment.
4. operating temperature
5. nuclear radiation.

4.2 Dependence of steel properties on the Si content

4.2.1 Effect on magnetic characteristics

Simplified (linearised) dependencies of density, H_c, M_s and resistivity are summarised in table 4.2 [30] (symbols are listed in table 4.1) The effect of the Si content on the characteristic parameters is presented in Fig. 4.1 [31] and in Fig. 4.2 for the B-H curves [32].

4.2.2 Effect of the Si content on AC losses

An increase of the Si content decreases H_c, which controls the magnetic properties up to the knee, (typically in the range 1.4-1.6 T), increases μ_{max} and reduces the hysteresis losses, but decreases the saturation magnetisation $M_{s,}$ which controls the magnetic properties after the knee. Further the Si content increase results in an increased resistivity ρ, which decreases the eddy current losses, and increases μ_{max} of the dynamic B-H curve (B-H curve higher in B).

The SIS100 dipole models, fabricated in JINR (Dubna) with a design similar to the Nuclotron dipoles, used the anisotropic steels 3413 and 3414 with a Si content in the range 2.8-3.8 % in accordance with Russian Standard (GOST 21427.1-83). These are available with a maximum thickness of 0.5 mm.

The R&D model of GSI001 for SIS200 firstly used isotropic steels fast cycling superconducting magnets, isotropic cold rolled steel M250-50A coated with STABOLIT70. The Si content is 3.3% as in the certificate, the density 7.60 gcm^{-3} and the resistivity 0.6 $\mu\Omega m$ (calculated).

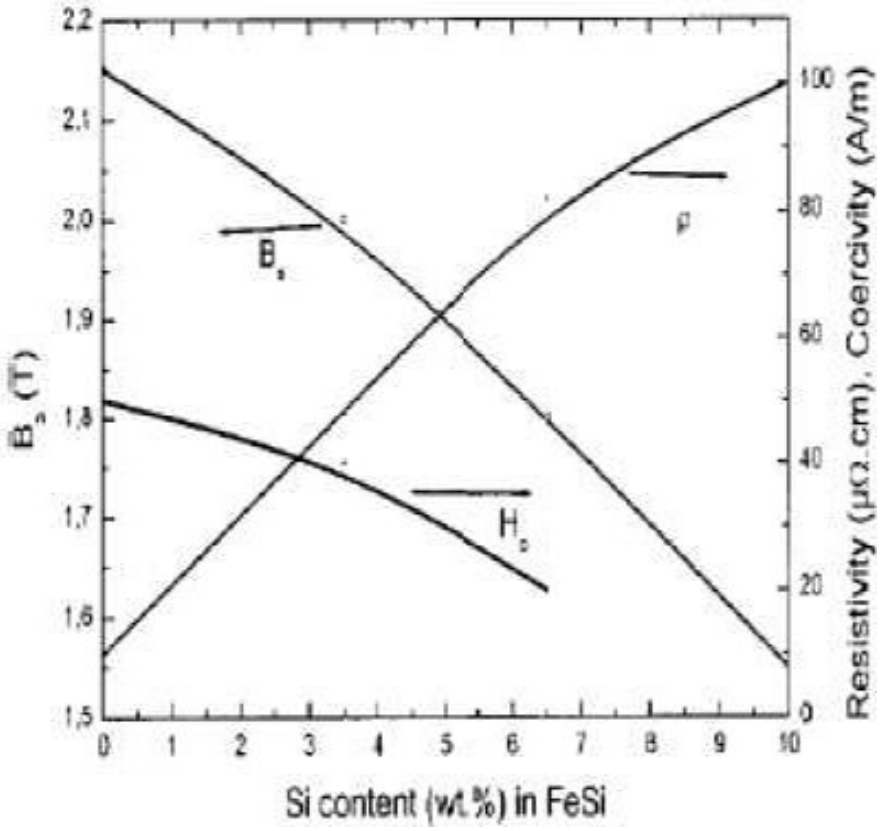

Figure 4.1: The dependence of the characteristic values of steel on the Si content on H A/m.

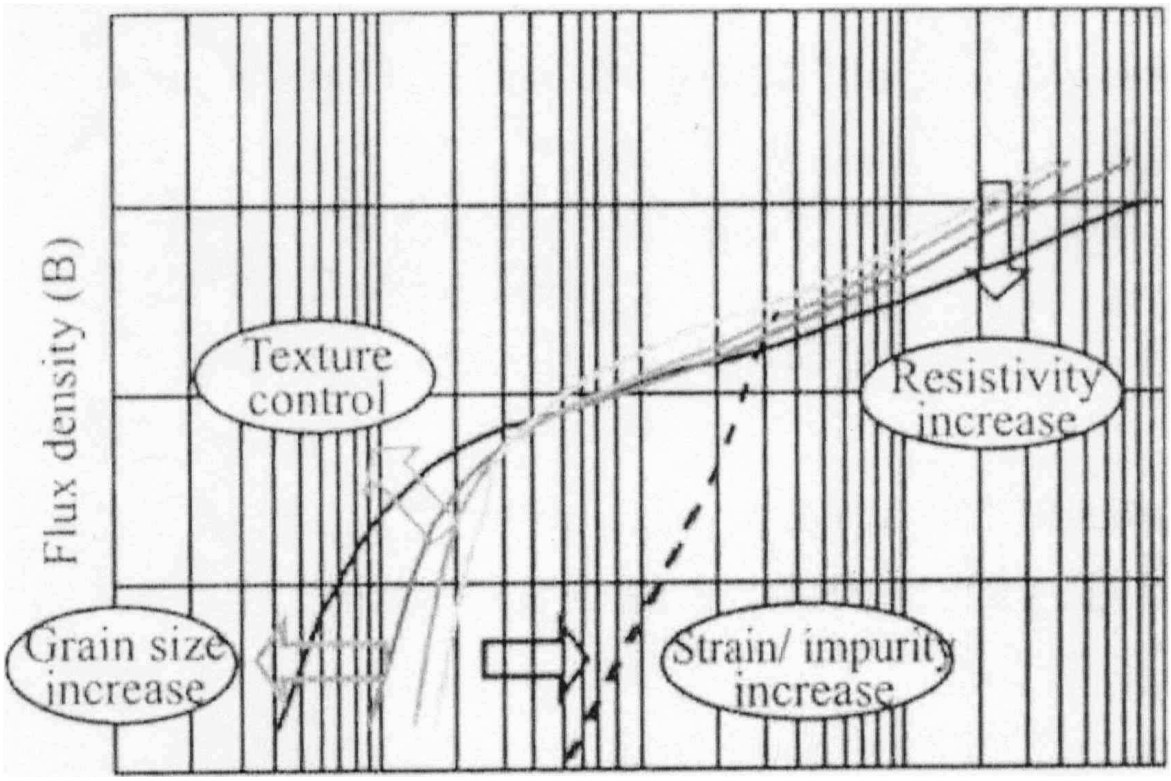

Figure 4.2: Effect of Si content on B-H curves

Table 4.3: Coercive force H_c measured in linear cycles with a frequency of 0.01 Hz. These data were measured with an Epstein frame.

	rolling direction	transverse direction	mixed
ET3413, B_{max} = 1.64 T	16	48	28
ET3414, B_{max} = 1.64 T	26	41	32
Stabocor M250-50A, B_{max} = 1.67 T	30	50	39

Table 4.4: Coercive force H_c at B_{max} = 1.5 T for turned rings.

H_c A / m @	300 K	77 K	4.2 K
ET3413	21.3	20.8	21
ET3414	20.3	19.5	19.5
Stabocor M250-50A	31.5	30.5	30.9

4.3 Comparison of high grade oriented and non oriented Si steels

4.3.1 Comparison H_c and B-H curves of different steels

In Table 4.3 the coercive force of these strips are presented (300K) [33]. One can see that H_c of mixed samples is approximately equal to the average value of the coercive forces of strips along the rolling direction (RD) and normal to the rolling direction (TD). Coercive forces, obtained on small turned rings at different temperatures, are presented in Table 4.4.

B-H curves of anisotropic steels 3413 and 3414

The dependences of B(H) obtained on small turned rings for steels 3413 and 3414 are presented in Fig. 4.3(a) [34, 35]. The difference is small at B $<$ 1.0 T, the ET3414 has higher permeability at B $<$ 1.0 T in accordance with the lower H_c (20.3 A/m versus 21.3 A/m of ET3413), the difference is small at B $<$ 1.0 T and the curves coincide practically at B $>$ 1 T.

B-H curves of isotropic steel M250-50 and anisotropic steel 3413

The dependences of B (H), obtained on small turned rings for steels M250-50A and 3413 are presented in Fig. 4.3(b). It should be noted that the B-H curve of isotropic steel with higher H_c lie above the B-H curve of anisotropic steel with lower inte-

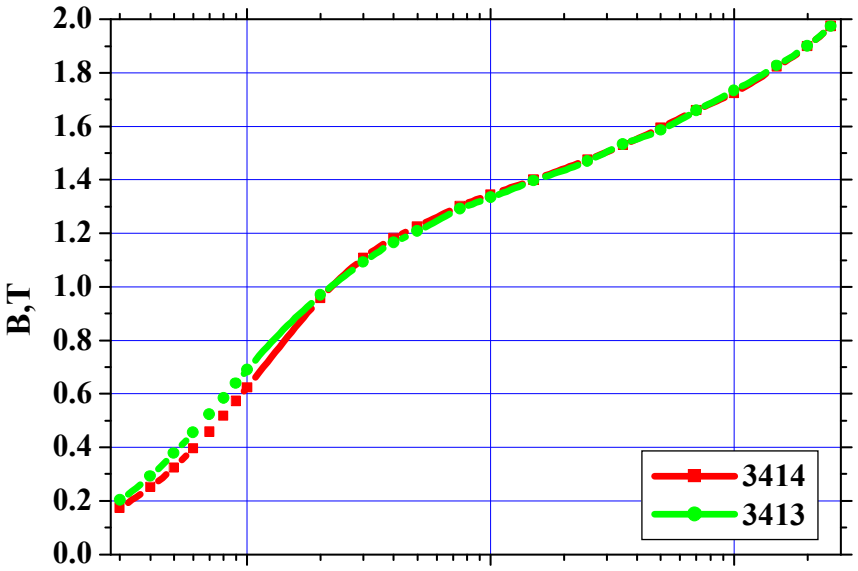

300 K, turned rings

(a) anisotropic

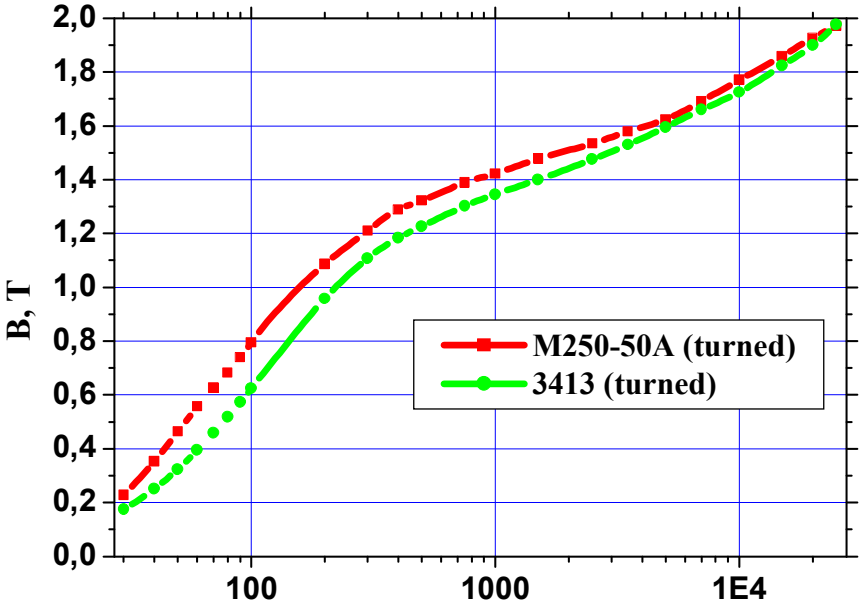

300 K

(b) anisotropic vs isotropic

Figure 4.3: B-H curves of the anisotropic ET3413 and ET3414 steels as well as a comparison of the B-H anisotropic ET3413 to the isotropic M250-50A

Table 4.5: Hysteresis and coercive force of selected isotropic steels

Steel	ET3413	M250-50	M600-100	M700-100
M_s [T]	2.055	2.035	2.035	2.1
H_c [A/m]	20 - 30	30 - 33	30 - 33	35 - 40
Si content %	3.3	3.0	2.4	2.8

grated H_c. But above 1.6 T, when the saturation magnetisation determines the magnetic properties, both curves differ only by a small value.

4.3.2 Comparison of hysteresis losses of different steels

The hysteresis losses, measured in non-oriented steels (M250-50A and 2412) and oriented steels 3413 and 3414 in unipolar cycles at 4.2 K are shown in Fig. 4.4. The three steels M250-50A, ET3413 and ET3414 have similar losses up to 1.5 T, with different but small enough coercive forces (31.5 A/m, 21.3 A/m and 20.3 A/m respectively), measured on the small turned rings. Contrary the steel ET2412, with H_c = 42 A/m (may be due to higher carbon content and lower Si content than M250-50A) will produce larger losses. But above 1.5 T the curves are close and even intersect, with a value spread of approximately 10% (35 mJ/kg). It means that these steels will produces equivalent hysteresis losses in magnets, where the maximum fields in the iron will be in the region of 1.5-2.2 T. This applies also for the iron yoke of Nuclotron type magnets, made up to now, where the magnetic flux vector continuously changes its orientation with respect to rolling direction.

4.3.3 Isotropic steels

The performance of the isotropic steel M250-50A is similar to the performance of anisotropic steels. Next to this also M600-100 was considered, given that its hysteresis losses are similar at room temperature (see Table 4.5). The static B-H curves and coercive forces are presented in Fig. 4.5. One can see that ET3413, M250-50 and M600-100 are comparable. The steel M700-100 provides a slightly higher saturation magnetisation M_s but its coercive force H_c is considerably larger.

4.3.4 Material – components – device

Rings, made by the same technology from isotropic M250-50A and anisotropic ET3413, have different coercive forces (31 A/m and 21 A/m), but close hysteresis

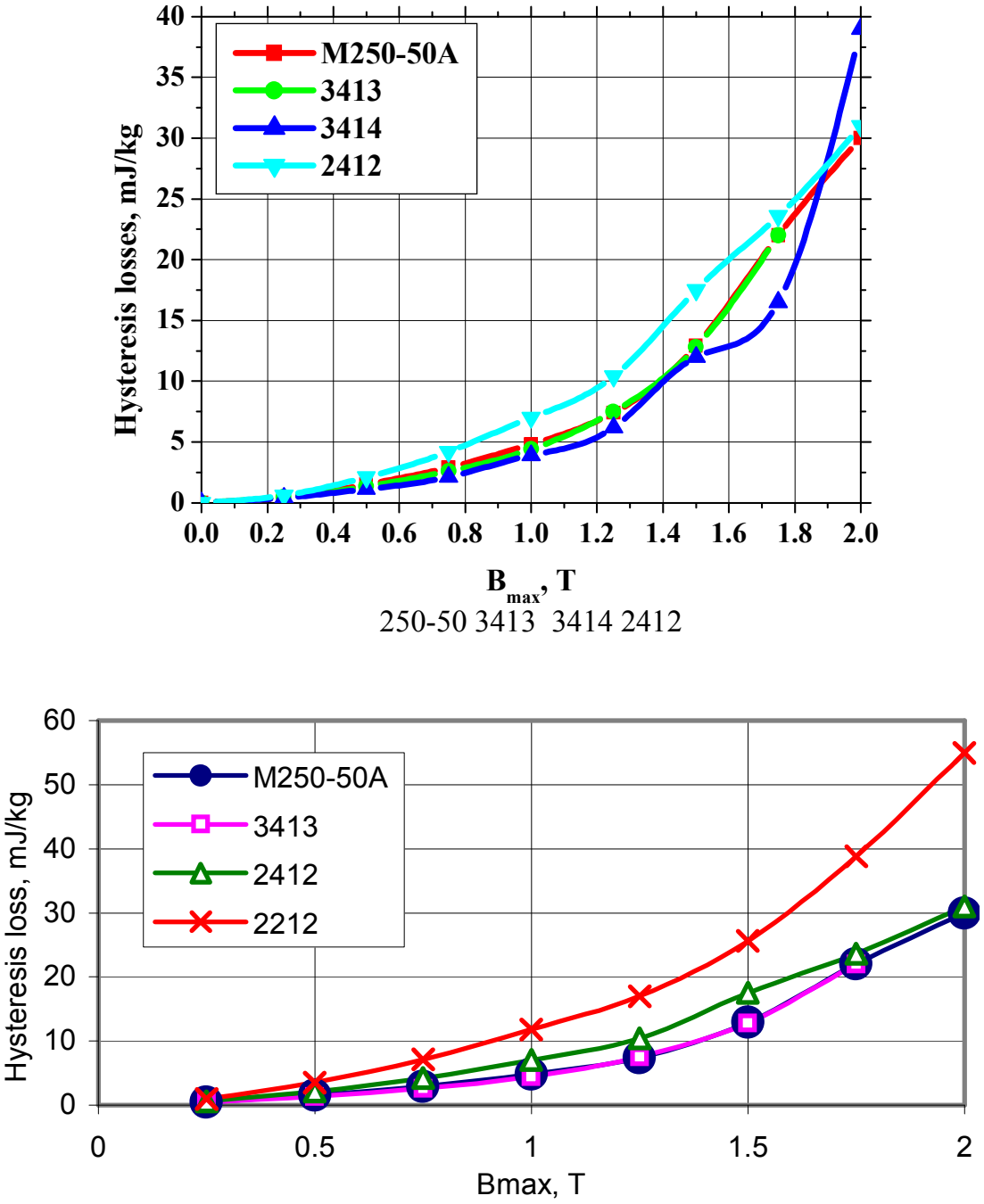

Figure 4.4: Hysteresis losses in unipolar cycles 0-B_{max}. unipolar cycles at 4.2 K in steels

losses for cycles with $B_{max} > 1.5$ T especially at B_{max} near 2 T. It confirms the fact, that the coercive force is good for primary estimations. The eddy current losses are close to each other for M250-50A and ET3413 and negligible small due to the lamination thickness and the low frequency.

The original properties of the steel lamination sheets are influenced by the tech-

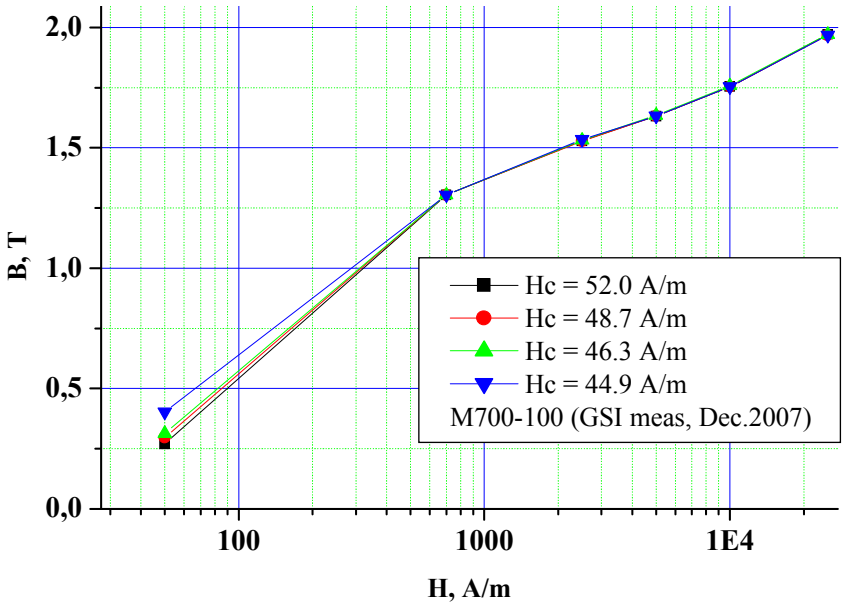

Figure 4.5: The B-H curve of the isotropic steel M700-100. Measurement data courtesy of F. Klos

nological effects, design of the real magnet yoke and operation conditions: laminated compound, manufacturing technology and field parameters (maximum field, cycle frequency, field direction within the steel).

It should be noted that the B-H curve of isotropic steel with higher H_c are above the B-H curve of anisotropic steel with lower averaged H_c. But for B $>$ 1.6 T, when the saturation magnetisation determines the magnetic properties, the curves differ only by a small value (The low induction part and the approach to saturation in the anisotropic steel in the ring sample differ from the ones for isotropic steel).

1. There are large uncertainties in magnetic properties of steels and one should be very careful when optimising the 2D cross section:

   (a) measurement method (strip, rings, static (low frequencies) or 50 Hz);

   (b) anisotropy;

   (c) technology (production, stamping, turning);

   (d) operating temperature;

   (e) tension.

2. An approved agreement about correct use is required by users of the B-H data and its recalculation for different cases.

3. Accurate test measurements and detailed recalculations are required to obtain a high resolution magnetic field description.

4.4 Selecting the steel

The choice of the electrical steel, best appropriate for the operation parameters of the main SIS100 magnets, is crucial for an optimal adjustment of the requirements to achieve high field quality, minimum AC losses in the yoke and a safe, reproducible production technology.

The search for this was made in both principle possible directions, i.e. analysing the intrinsic properties of the Si-donated Fe system as well as the available commercial steel. In the latter case also the impact of the technological and real application effects was discussed.

The conclusions are the following:

1. The development of new steel, outperforming the existing commercial ones is extremely time consuming and costly, i.e. could be reasonable if at all only for very large projects. Moreover, the probability to develop a new modification significant better than the existing commercial steels is quite low, due to the principal physical properties of the Fe-Si system and negative technological consequences (lower B_s, brittleness, long time instability etc.).

2. The application of the more expensive anisotropic (grain oriented) steel is not an advantage compared to the available isotropic steel because the field direction rotates within the transversal lamination planes of the accelerator magnet. Its preferred magnetic properties are effective only in a narrow spectrum of the local field vectors.

3. The detailed R&D had shown that the magnetic and AC loss properties of isotropic and anisotropic steels with 3% Si are close under the given design conditions.

4. The best choice for 0.5 mm lamination thickness will be M250-50A (or the equivalent ET2414 or the anisotropic ET3414, as their hysteresis losses are similar). Utilising the technological advantages of thicker lamination, the 1.0 mm thick sheets of M600-100A should be used with similar properties at low AC frequencies around 1Hz.

5. At the time, the first full size dipole was manufactured, steel was hard to get. The steel M700-100A, readily available at the time of manufacturing, was used for the full scale magnet. The other two existing full size dipoles are manufactured using the anisotropic steel ET3414 with a lamination thickness of 0.5 mm. Their measured field quality and AC loss will provide important information for the final steel selection.

6. The finally used steel will also depend on the requirements of the series production, e.g. well controlled material properties.

Chapter 5

Magnetic field design

5.1 Field representation

5.1.1 Coordinate system

The axis y points upwards. z points along the magnet and x is used such that one forms a right hand x, y, z coordinate system.

Calculations in three dimensions produce a lot of data, thus a reduction is necessary to represent the main issues. The field on a elliptical cylinder with appropriate diameters was extracted from the grid and then elliptical multipoles were calculated [36, 37, 38, 39, 40, 41]. Out of these data circular multipoles with a reference radius of 40 mm were calculated.

5.1.2 Circular multipoles

The classical circular multipoles

$$\mathbf{B}(\mathbf{s}) = \sum_{n=1}^{\infty} \mathbf{C_n} \left(\frac{\mathbf{s}}{R_{Ref}} \right)^{n-1} \tag{5.1}$$

are used and appropriate to describe the magnetic field in the area of interest. Here $\mathbf{B}(\mathbf{s}) = \mathbf{B}\,(x + \mathtt{i}y) = B_y + \mathtt{i}B_x$ with x and y the Cartesian 2D coordinates and R_{Ref} the reference radius. The higher order harmonics $\mathbf{c_n} = b_n + \mathtt{i}a_n$ are given by

$$c_n = \frac{C_n}{C_m} 10^4 \tag{5.2}$$

with m the main multipole ($m = 1$ for the dipole).

5.1.3 Elliptic multipoles

The field within the elliptic beam aperture is described using elliptic multipoles for elliptic coordinates of the type

$$x = e\cosh\eta\cos\psi \qquad y = e\sinh\eta\sin\psi \tag{5.3}$$

$$0 \le \eta \le \eta_0 < \infty \qquad -\pi \le \psi \le \pi \tag{5.4}$$

with x and y the Cartesian coordinates and η and ψ the elliptic coordinates. The field $\mathbf{B} := B_y + iB_x$ can be described within the whole ellipse using

$$\mathbf{B}(\eta,\psi) = \sum_{q=0}^{M} \mathbf{E}_q \frac{\cosh[q(\eta+i\psi)]}{\cosh(q\eta_0)}, \tag{5.5}$$

with $\eta_0 = \tanh^{-1}(b/a)$ the reference ellipse and a and b its half axes [39, 41] (here $a = 45\,mm$ and $b = 17\,mm$). These $\mathbf{E}_q$ can be recalculated to circular multipoles using an analytic linear transformation [41].

5.1.4 Toroidal multipoles

In the gap of a curved magnet a torus segment ($-\varphi_0 \le \varphi \le \varphi_0$) is used as reference volume. Dimensionless local toroidal coordinates ρ, ϑ, φ are defined by

$$X + iY = R_c\, h\, e^{i\varphi},\ \ Z = R_{Ref}\sin\vartheta,\ \ h = 1 + \epsilon\rho\cos\vartheta, \tag{5.6}$$

with R_{Ref} (R_c) the minor (major) radii of the torus and $\epsilon := R_{Ref}/R_c < 1$ the inverse aspect ratio describing the magnitude of the curvature effects. The centre of the fundamental Cartesian system (X, Y, Z) coincides with that of the torus, Z is normal to the equatorial plane. The quasi-radius $\rho \cdot R_{Ref}$, $0 \le \rho \le 1$, is the normal distance of the field point from the centre circle $Z = 0$, $\sqrt{X^2+Y^2} = R_c$; the poloidal angle $-\pi \le \vartheta \le \pi$, is around the centre circle; the toroidal angle $-\pi \le \varphi \le \pi$ agrees with the common azimuth. Only toroidally uniform fields are considered; their field components B_x, B_y are confined to the planes φ = const. and are independent of φ. (x, y) are local Cartesian coordinates in these planes; the $x-$, $(y-)$ axes are parallel to the $X-$, $(Z-)$ axes. The potential equation for toroidally uniform fields

is (neglecting a constant factor)

$$\left[\frac{\partial^2}{\partial\rho^2}+\frac{1}{\rho}\frac{\partial}{\partial\rho}+\frac{1}{\rho^2}\frac{\partial^2}{\partial\vartheta^2}+\frac{\epsilon}{h}\left(\cos\vartheta\,\frac{\partial}{\partial\rho}\;-\frac{\sin\vartheta}{\rho}\,\frac{\partial}{\partial\vartheta}\right)\right]\Phi$$
$$=h^{-1/2}\left[\frac{\partial^2}{\partial\rho^2}+\frac{1}{\rho}\frac{\partial}{\partial\rho}+\frac{1}{\rho^2}\frac{\partial^2}{\partial\vartheta^2}+\frac{\epsilon^2}{h^2}\right]\left(h^{1/2}\,\Phi\right)\;=\;0, \tag{5.7}$$

with the first three terms in the square brackets the Laplacian in plane polar coordinates ρ, ϑ. The last term, due to the curvature, introduces contributions which may be represented as a power series in the inverse aspect ratio ϵ. Approximate toroidal multipoles accurate to order ϵ can be obtained by (see second line of (5.7)):

$$\Phi_m(\rho,\vartheta)=h^{-1/2}\,\rho^{|m|}\,e^{im\vartheta}+O(\epsilon^2), \tag{5.8}$$
$$\approx\rho^{|m|}\,e^{im\vartheta}-\tfrac{\epsilon}{4}\,\rho^{|m|+1}\left(e^{i(m+1)\vartheta}+e^{i(m-1)\vartheta}\right).$$

The multipoles are orthogonal to order ϵ w.r.t. the scalar product

$$\left(\Phi_m,\Phi_k\right):=\int_{-\pi}^{\pi}\Phi_m^*(1,\vartheta)\Phi_k(1,\vartheta)\;h\;d\vartheta=\;2\pi\;\delta_{mk}.$$

$h=1+\epsilon\cos\vartheta$. The expansion coefficients τ_m of a given potential

$$\Phi(\rho,\vartheta)=\sum_{m=-\infty}^{\infty}\tau_m\,\Phi_m(\rho,\vartheta) \tag{5.9}$$

are defined by values given along the reference circle $\rho=1$:

$$\tau_m=\;\left(\Phi_m(1,\vartheta),\Phi(1,\vartheta)\right)/(2\pi) \tag{5.10}$$

This theory can be extended to vector fields (required e.g. to interpret rotating coil measurements in a curved magnet) [42].

5.2 2D design

The AC losses (in the order of 80 – 100 W for the triangular cycle) as well as the required cooling power demanded a single layer coil for the dipole [43, 44, 45]. A magnet design with the minimal required magnet aperture also allows reducing the required yoke size and was thus favoured in the beginning. The magnet design was made [46] and the field deterioration analysed. The sextupole of the "minimal design" is much larger at even medium fields than for the double layer version [46].

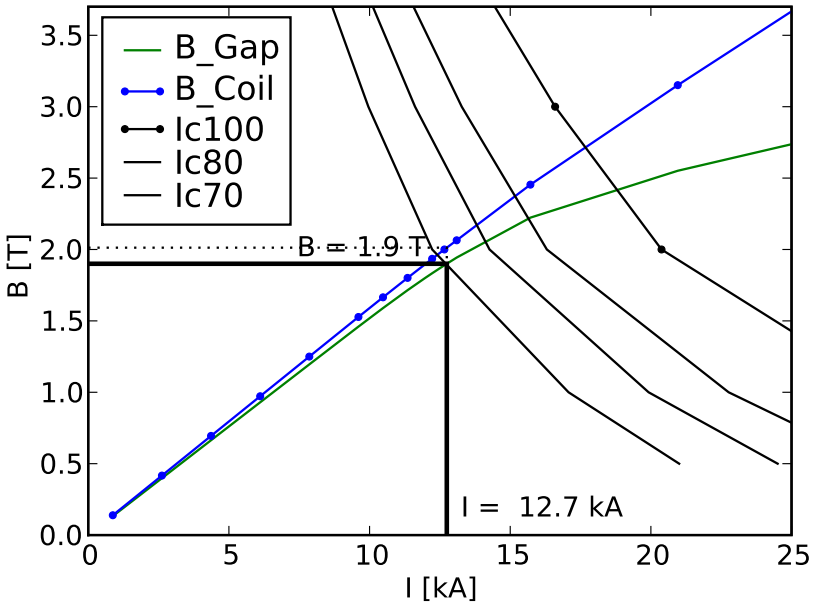

Figure 5.1: The high current cable for the single layer dipole

Thus the free aperture in the coil was increased from 130 to 140 mm (option "CSLD") to obtain a sextupole and a decapole ($b_3 = 240\,ppm$, $b_5 = -100\,ppm$) comparable to the curved double layer dipole ($b_3 = 280\,ppm$, $b_5 = 20\,ppm$). This design also provides space for the vacuum chamber ribs as well as an space margin for the beam cross section.

The designed lamella is presented in Fig. 2.7 page 18. The load line and critical current is given in Fig. 5.1 and the first allowed harmonics (2D Field) in Fig. 5.2 for $R_{Ref} = 40\,mm$.

5.3 3D design

The magnet was modelled together with its coil in TOSCA and the field was calculated and an appropriate Rogowsky end was designed. Calculations were also performed for an rectangular end as well. This calculation revealed (see Fig. 5.3) that the integral transfer function $t_f = C_1/I$ decreases much more than the length. Therefore the integral strength linearity is not much improved using a Rogowsky profile. The obtained magnetic field characteristics are given in Fig. 5.3(c) (b_3) and in Fig. 5.3(d) (b_5). We found that the integral magnetic field strength varies by 4% while the effective length varies only by 1% and the Rogowsky profile improves the length variation only by 0.5 %. So the integral transfer function $t_{fi} = \int_{-\infty}^{\infty} B(l)\mathrm{d}l/I$

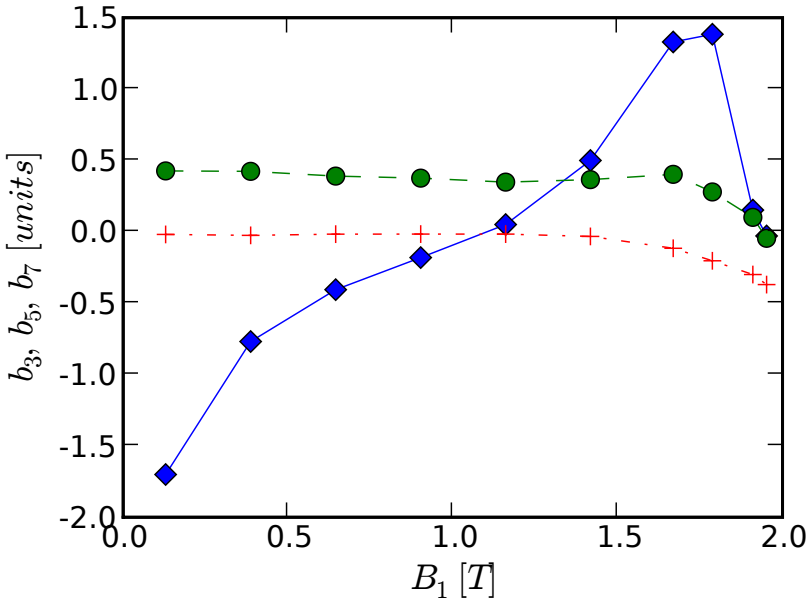

Figure 5.2: The static 2D field harmonics: sextupole b_3 . . . blue, b_5 . . . green, b_7 . . . red.

non linearty is created mainly by the iron steel non linearity. So the impact of an rectangular end (i. e. the changed field quality) on the beam will be studied carefully as this option simplifies the magnet and reduces the AC losses [10] (see also section 6.4.2 page 74).

5.4 Calculation quality and measurement results

The curved single layer dipole has not yet been built; so all data presented above are based on calculations. But the first dipole, built by BNG [15], was measured thoroughly including the magnetic field [7, 3, 9, 10] using a mole [47, 48] as well as a mapper with a 3D hall probe. The multipoles were calculated as presented in [41].

The measured and calculated field strength and quality are given in Fig. 5.4 and Fig. 5.5. One can see that the measured and calculated multipoles match nicely and thus prove that the methodical work is correct and the above presented calculations reliable [48, 41].

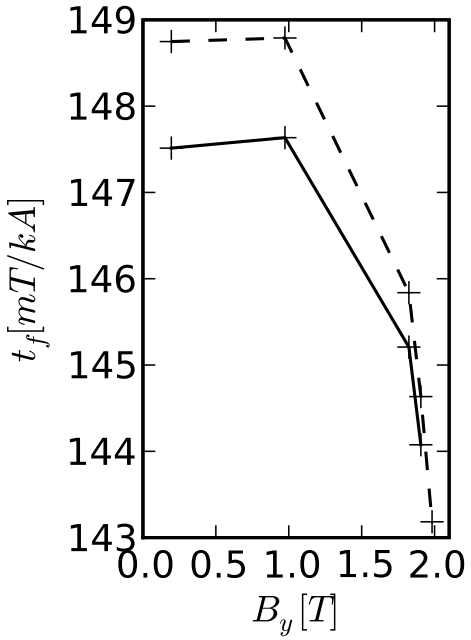

(a) transfer function

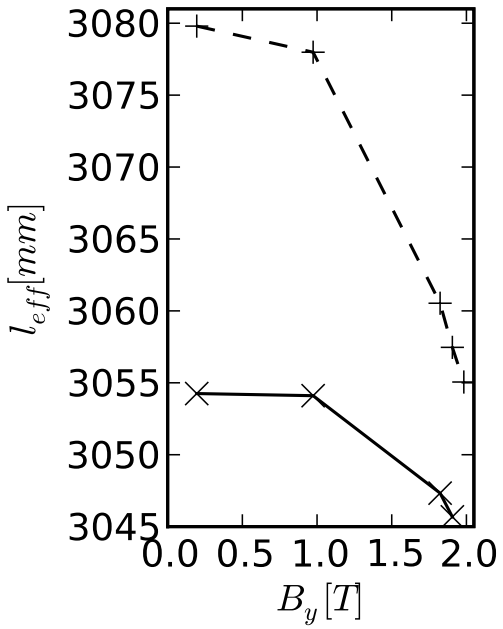

(b) length

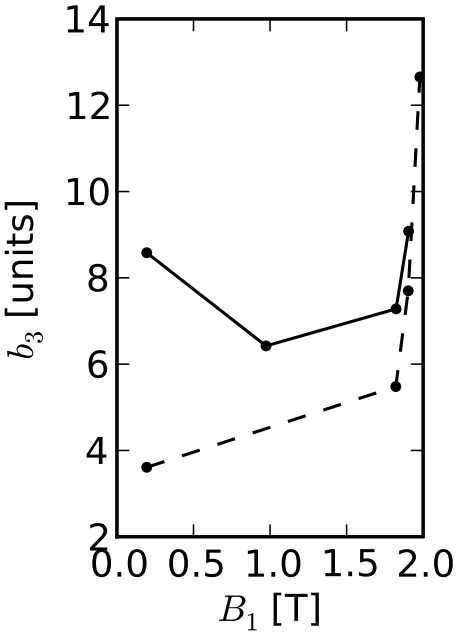

(c) b_3

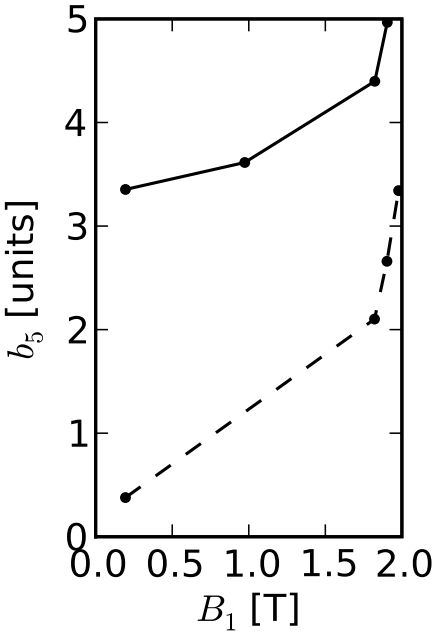

(d) b_5

Figure 5.3: Calculated characteristics of the CSLD. The transfer function is given for the centre (x) and for the integral divided by a fixed length of 3054 mm (x . . . central field, + . . . Rogowsky profile · . . . rectangular end) as well as the magnetic length. The sextupole and dekapole are given as well (solid line . . . Rogowsky profile, dashed line . . . rectangular ends, ∘ . . . transient Elektra calculations for the Rogowsky profile)

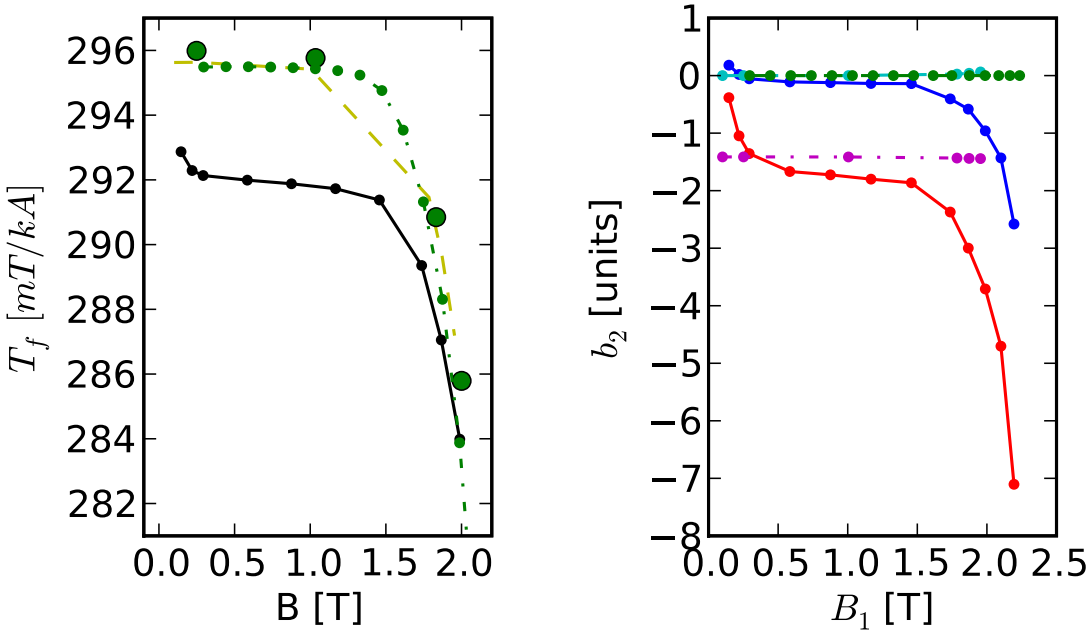

(a) centre, transfer function

(b) end, b_2

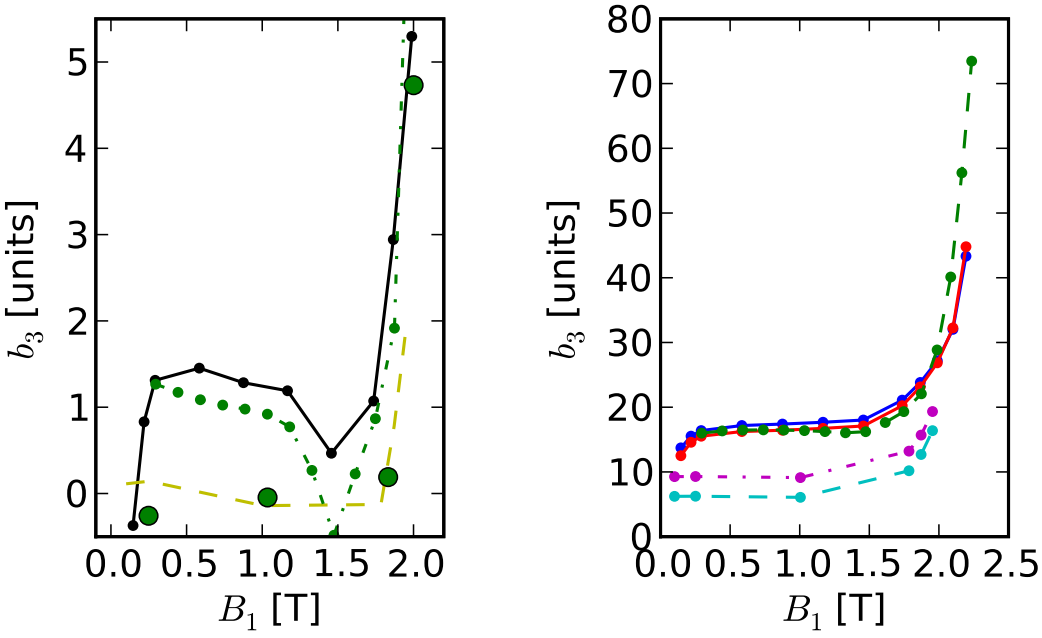

(c) centre, b_3

(d) end, b_3

Figure 5.4: The measured and calculated transfer function and the b_2 and b_3. centre: black line . . . measured, yellow line . . . TOSCA, green circles . . . TOSCA rectangular end, green line . . . ANSYS; end: connection side: blue line . . . measured, cyan line . . . TOSCA, non connection side: red line . . . measured, mangenta line . . . TOSCA,

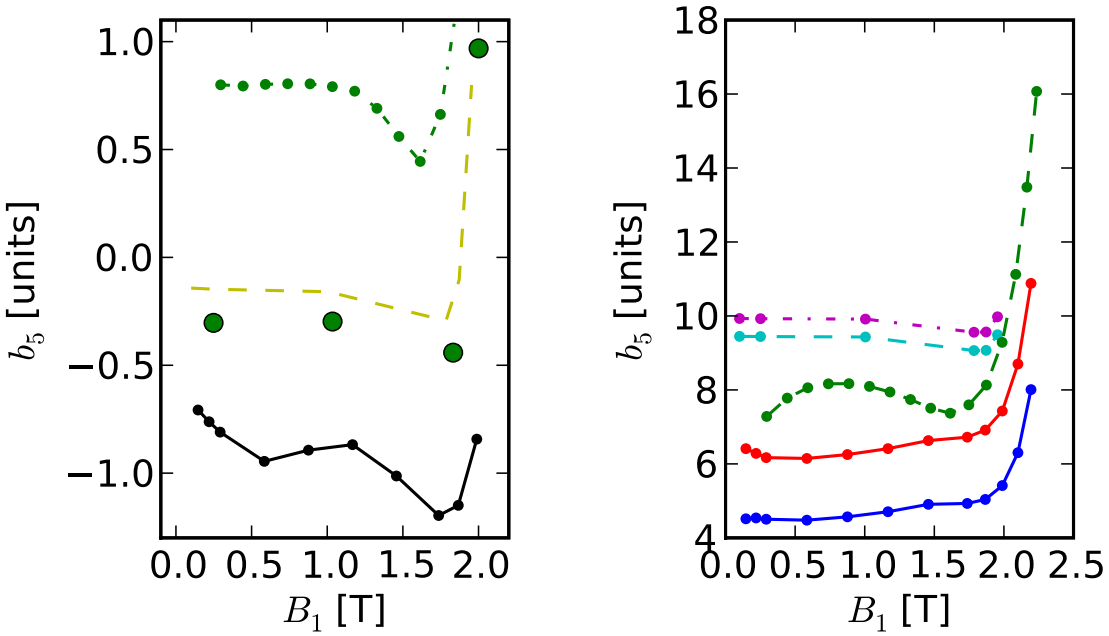

(a) centre, b_5

(b) end, b_5

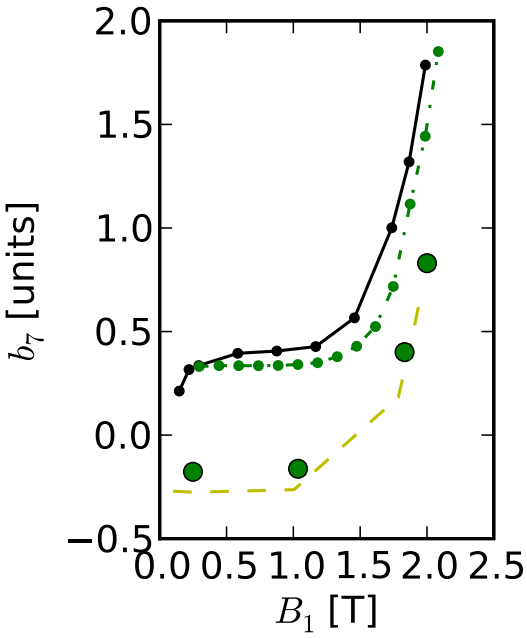

(c) centre, b_7

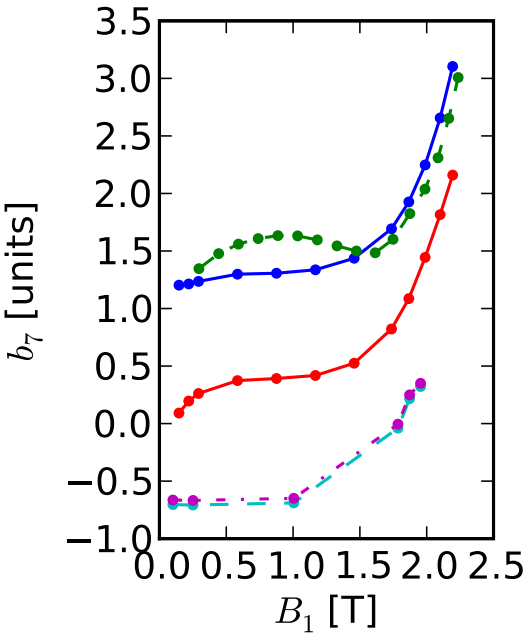

(d) end, b_7

Figure 5.5: The measured and calculated b_5 (dekapole) and b_7. centre: black line . . . measured, yellow line . . . TOSCA, green circles . . . TOSCA rectangular end, green line . . . ANSYS; end: connection side: blue line . . . measured, cyan line . . . TOSCA, non connection side: red line . . . measured, mangenta line . . . TOSCA,

Chapter 6

Losses and hydraulic limits

6.1 R&D on model magnets

At the original Nuclotron magnets large AC losses occur during continuously cycling with a ramp rate up to 4 T/s and B_{max} = 2 T in the iron yoke, in the structural elements and in the cable with 70 % coming from the cold yoke and 30 % from the coil. Further heat is created by the eddy currents in the beam pipe. To reduce the load on the cryogenic supply system and the operational costs of SIS100 all the significant heat sources were identified and reduced to the technological minimum [49]. The brackets and the end plates holding the lamination together were replaced with stainless steel (SS) ones and the laminations near the yoke ends were slit to suppress the eddy current generation by the longitudinal field component $\mathrm{d}B_z/\mathrm{d}t$ (see Fig. 2.8 page 19). The coil ends were modified to fit the beam pipe as closely as possible to reduce the field spreading into the yoke. A Nuclotron-type cable based on wire with a filament size of 4.1 μm (”EAS” wire [50]) reduced the losses even further.

6.2 Operation cycles and cooling limits

The practical test of the cooling conditions on the full size magnets is an important research goal defining the main operation parameters of the SIS100. The cooling limit of the magnets, given by the two phase helium cooling, has to be adjusted with the heat loads of the various operation cycles and with the hydraulic resistance of the coil to guaranty a stable two-phase helium flow and a sufficient temperature margin for the superconductor. But the hydraulic resistance of the coil should not be

reduced too much, otherwise the energy efficiency for cooling the low loss modes would degrade.

6.2.1 Estimation of the cooling limits for the straight dipole

The actual proposed SIS100 cycles [11] are given for the straight dipole version in table 1.1 page 10 (see also Fig. 1.1 page. 10). The injection requires a field of 0.24 T over 0.8 seconds. Then the magnets are ramped up with 4 T/s to the maximum field B_{max}, followed by a flat top time of t_f. The expected dynamic loss per cycle and the average loss power values Q_d, P_d are extrapolated from measurements on short model dipoles.

More then 80% of the AC loss at 4.5 K, created in the magnet, are coming from the iron yoke due to the large cross section. Q_q and P_q are the respective parameters for the quadrupole. Hydraulic calculations had shown that the most intensive cycle 2c should be close to the upper cooling limit [51]. In addition also the low loss limit should be considered in more detail to provide a stable forced flow cooling for all requested operation cycles. The correctness of these estimations were verified testing the first full size magnets [6, 8, 10].

6.2.2 Operation test on an equivalent dipole system

A full length equivalent dipole system was tested to estimate the limits for the cycles. This model dipole consisted of a serial combination of the standard Nuclotron dipole and an optimised short model magnet, both individually tested before. The sum of the AC loss of both 1.4 m long models was close to the total loss expected for the 2.8 m straight dipole. The cooling scheme of the tests is given in Fig. 6.1. The coils of the magnets were connected in series with respect to the helium flow and the supply current. For these measurements the cryostat and the power supply system were redesigned at the JINR magnet test facility.

In these measurements the mass flow rate was adjusted for $x_6 \approx 1$, i.e. the mass vapour content at T6 was always close to the critical line of the two-phase helium region. The loss data are in adequate agreement with the values obtained for the individual magnets [52] and confirm our estimations of the cooling limits for the full length dipole. The quench current of the system reached 7916A without preliminary training. The genuine cycle 2c could not be realized, the pause between the ramping had to be increased at least to a cycle period of 2.2s (cycle 2c'). The results are summarised in Fig. 6.2. The measured helium pressure drop ΔP dependence on

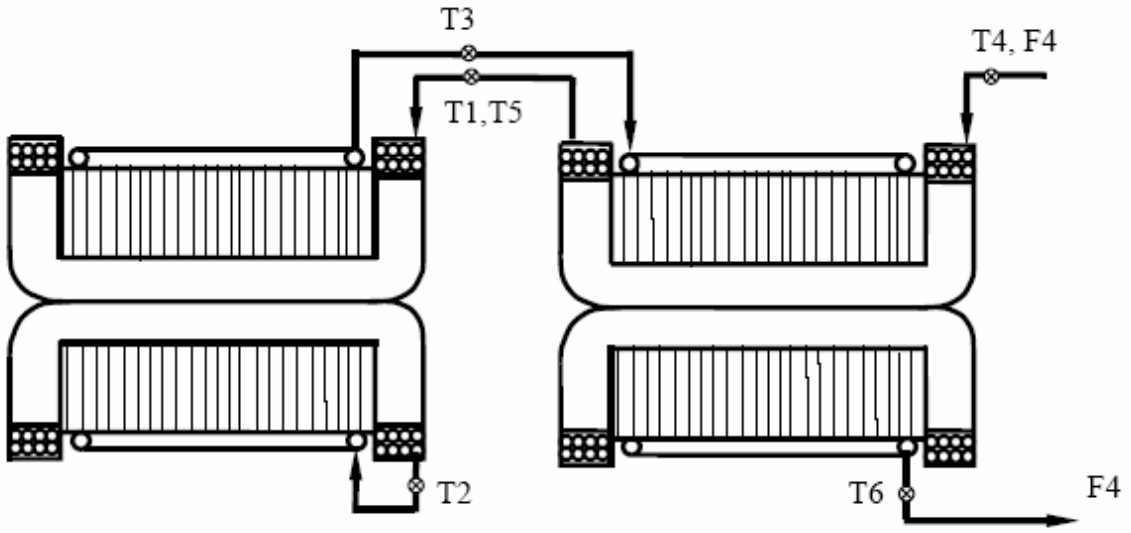

Figure 6.1: Cooling schema of the equivalent dipole model: T1, T2,... T6 - temperature measurement points, F4 - measured helium flow. The two-phase helium flow enters the laminated yoke after cooling the two short coils all connected in series.

the corresponding time averaged heat loss Q_a in the model dipole is plotted for the cycles given in Table II. A two parameter fit for

$$\Delta P = c_0 \cdot Q_a^n \tag{6.1}$$

defines $n = 1.733$ and c_0. The parameter $n = 1.75$ is the well know mass flow rate exponent describing the pressure rise due to friction, so $c_0 = 0.00153$ is the only adjusted coefficient. The results for cycle 2c' had shown, that under the given cooling conditions and ramp rates the upper limit for stable cycle operation is defined by $Q_{aL+} = 35\,W$. Using this characteristic value and introducing the maximum pressure drop ΔP_0 we obtain

$$\Delta P = \Delta P_0 \left(\frac{Q_a}{Q_{aL+}} \right)^{1.75} \tag{6.2}$$

with $\Delta P_0 = 0.77$ bar, the microscopic description of these parameters is given in detail in [53]. For the stable cycle 2b (ΔP = 0.15 bar) and the unstable cycle 3b (ΔP =0.10 bar) the loss values could not been measured and was calculated using the fit line. The experimentally obtained stability limit was closer to cycle 3b so we can estimate it as $P_{min} = 0.12$ bar or $Q_{aL-} = 12W \approx 1/3 Q_{aL+}$.

More intensive cycles require to increase Q_{L+}. This can be achieved by changing the yoke outlet temperature T6 into the vapour area, but assuring $x_2 < 1$ at the outlet

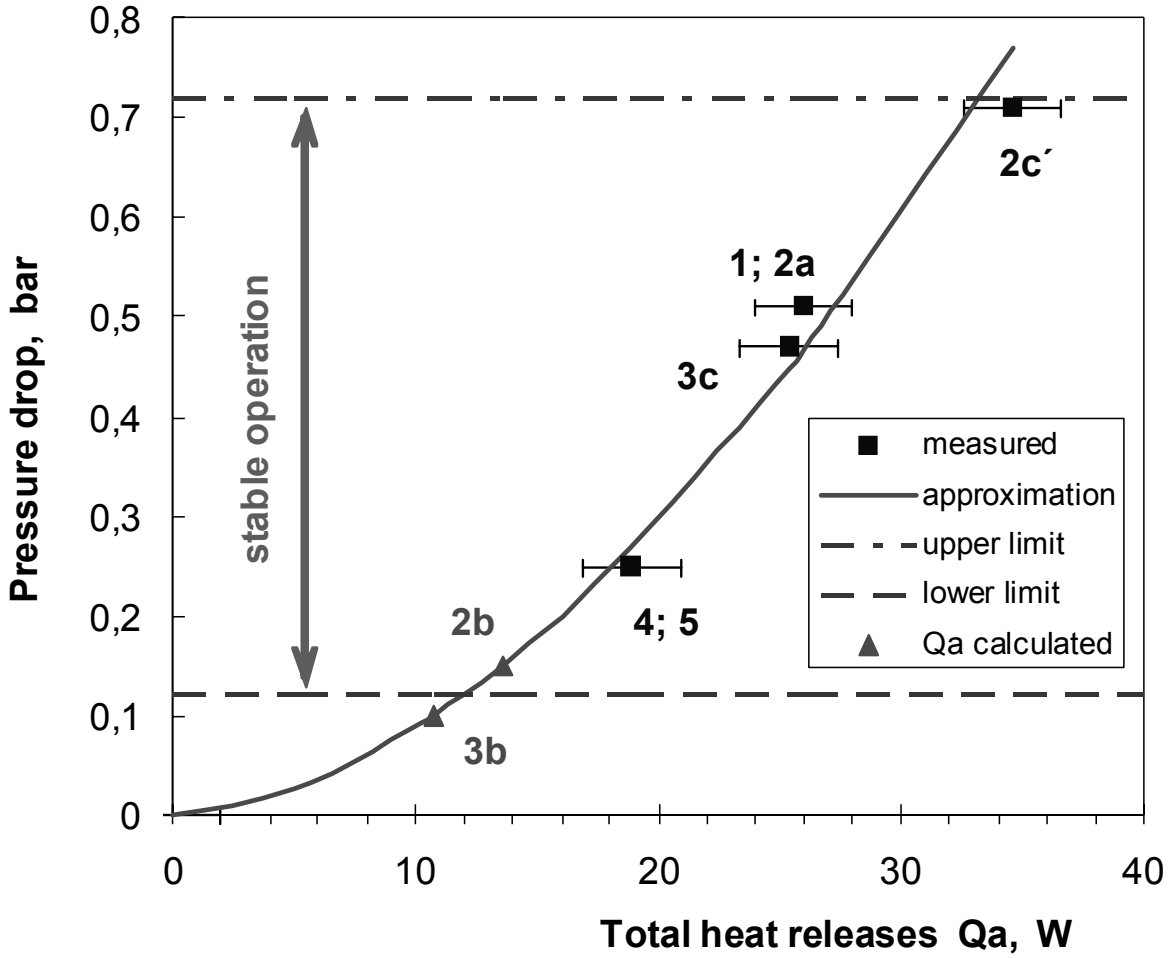

Figure 6.2: Cryogenic stability range of the 2.8 m long equivalent model dipole. The cycle names are plotted near their data points.

of the coil. The method is demonstrated in Fig. 6.3 showing the results obtained for the composite dipole, tested this way in a stable triangular cycle with a heat load of 50.5 W, i.e. 50% above QL+ . In this operation mode the pressure drop spread is reduced by a factor of two (the higher values are calculated). For a cooling scenario with T6 = 4.4 K (x6 = 1) we have ΔP = 1.39 bar, i.e. an impossible mode, but the high load cycle was demonstrated with ΔP = 0.627 bar choosing T6 = 8.45 K. The same ideas could be applied to extend the SIS100 magnets operation to higher intensities, i.e. for continuous triangular cycles, not shrinking the main cycle limits defined in Fig. 6.2. This means, that the magnet design should be optimised for cycle 2c, the more intensive cycles can be provided as shown in this section.

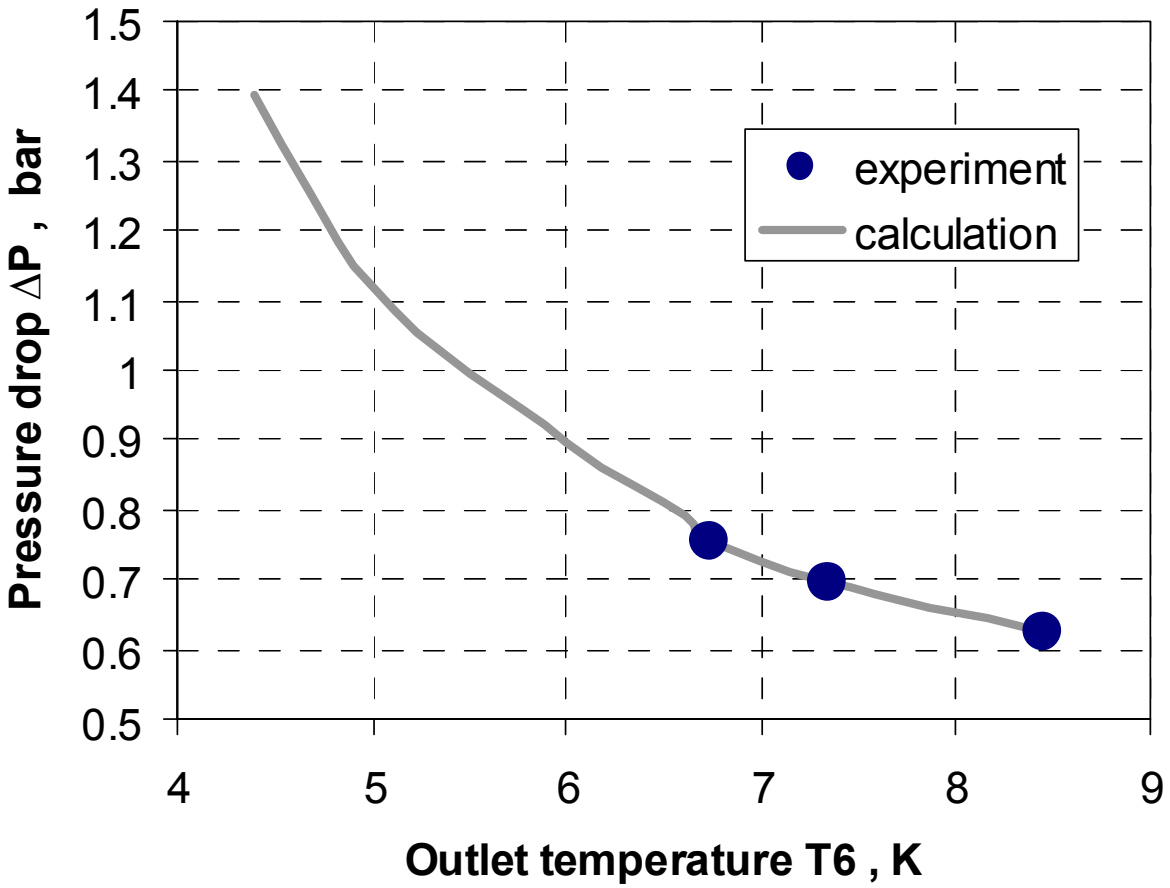

Figure 6.3: The pressure drop versus the yoke outlet temperature at the equivalent model dipole tested and calculated for a stable triangular cycle with the total heat load of 50.5 W.

6.3 Reducing the hydraulic limit

Currently the cycles generating the biggest heat load are the triangular cycle $/\backslash$ and the cycle 2c (see Table 7.1). The wide spread of more or less intensive ramped operation modes requires a clever adjustment of the hydraulic resistance of the coil with an optimal operation scenario for all the specific cycles. So the magnet design was optimised for the cycle 2c and the stable operation modes were stretched up to the triangular cycle to exploit the temperature margin of the iron yoke. Similar techniques were already tested on Nuclotron magnets for a long time during calorimetric measurements [54], i.e. the method is very effective for such measurements for a two phase helium flow without void fraction recording. Fig. 6.4(a) and 6.4(b) illustrates the T-S diagrams in both situations for the straight dipole. It is clear that, even cooling the yoke completely gaseous, the magnet would match the instability area. This estimations include no heat load margin and no cooling of the vacuum chamber.

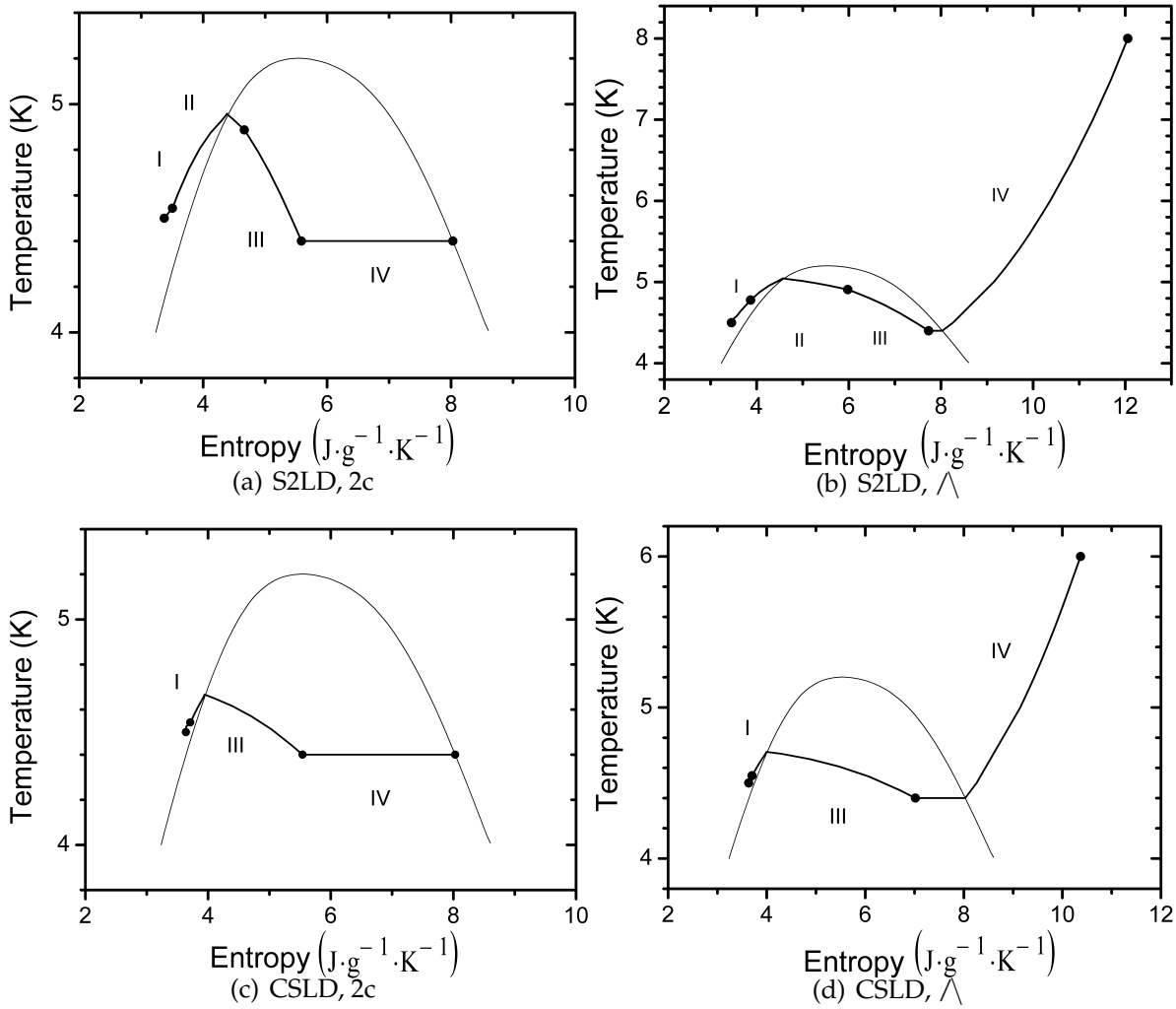

Figure 6.4: Temperature versus the entropy of the helium flow through the bus bars I, the inner II and outer III layer of the coil and the iron yoke IV for the two most demanding cycles: 2c and the triangular cycle /\. The top row represents the state for the straight double layer dipole (S2LD) described in Table I left column, and the bottom row for the curved single layer dipole (CSLD).

The heat load on the curved prototype dipole is reduced due to its smaller cross section, but it is still not operated in a stable regime. To reduce the hydraulic resistance of the coil by a factor of two, the original Nuclotron geometry of the cable must be changed to a larger inner diameter of the cooling channel from 4 mm to 4.7 mm. The consequences for the overall magnet design were discussed and various options are investigated considering cooling conditions [43] as well as concerning field quality arguments [55, 56, 36, 37, 38, 39]. The curved two layer option C2LDa [45] was designed to fulfil also a stable triangular cycle reducing the aperture size to a minimum. This ”minimal solution” had to be compared with other design

Table 6.1: The average power loss measured on the first straight full size dipole. TM08 ... coil in the middle of the magnet, on the lower side, TM09 ... on the yoke, in the middle of the magnet on the lower side, TM11 ... on the yoke (moved 200mm off the connection side end plate), TM12 ... on yoke surface in the middle of magnet.

dB/dt $[T/s]$	B_{max} $[T]$	t_d $[s]$	f $[Hz]$	$\bar{P}$ $[W]$	T_{out} $[K]$	dP $[mbar]$	$TM08$ $[K]$	$TM09$ $[K]$	$TM11$ $[K]$	$TM12$ $[K]$
1	2.1	0	0.23	30	6	640	6.5	7.6	6.4	6.1
1.5	1.4	0	0.51	30	5.75	658	6.34	7.5	6.2	5.9
1.5	1.6	0	0.44	33	6.49	667	6.9	7.8	6.8	6.5
1.5	1.9	0	0.31	35	7.12	674	7.4	8.1	7.3	7.0
1.5	2.1	0	0.33	37	7.8	691	7.9	8.4	7.9	7.5
2	1.9	0	0.49	43	9.6	735	9.2	9.4	9.2	8.9
2.5	2.1	0.8	0.37	41	8.9	740	8.8	9.1	8.9	8.5
3	1.9	0.8	0.45	43	9.2	780	9.0	9.3	9.1	8.7
3.5	1.9	0.8	0.49	43	9	775	8.9	9.1	9.0	8.5
4	1.9	1.6	0.37	40	8.4	733	8.3	8.7	8.4	8.0
4	2.1	1.5	0.39	43	8.08	793	8.1	6.9	8.3	7.7

versions providing high enough margins to guaranty save cooling and a high field quality for all requested operation modes without any doubt.

6.4 Full size dipole test results

The first SIS100 full size dipole, built and delivered by BNG [15], was tested thoroughly on the test station at GSI. Different cycles were tested and any continuous triangular cycle could be run as long as the total dissipated power was less than $\approx 45\,W$ [6, 8] (see also section 6.4.1 and table 6.3).

6.4.1 AC losses

The main goal of the measured AC loss data is to see if the load is acceptable as well as to provide a parameterised description for predicting the required cryogenic cooling power based on the cycles planned for SIS100. (The measured AC loss and temperature are listed in table 6.1)

The location of the temperature sensors(TM) is described in Fig. 6.5.

So the magnet (with and without installed vacuum chamber) was ramped with continuous triangular cycles with different ramp rates $dB/dt = \dot{B}$ as well as for different maximum fields B_{max}. For ramp rates close to the nominal ramp rate $\dot{B} = 4\ T/s$ as well as for maximum fields close to the nominal $B_{max} = 2\ T$ the

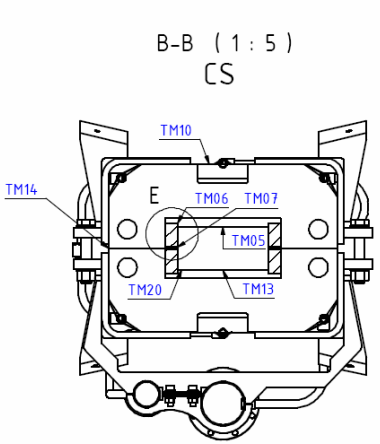

(a) connection side

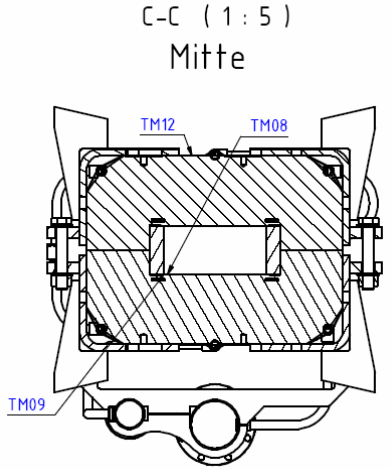

(b) middle

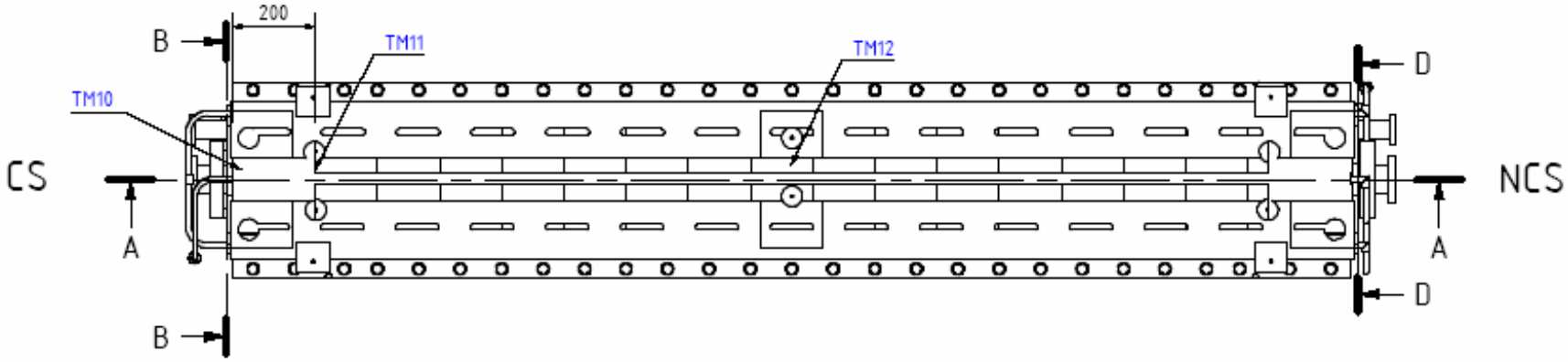

(c) side

Figure 6.5: Location of the temperature sensors. TM04 ... cooling tube at return flow from yoke, TM08 ... coil in the middle of the magnet, on the lower side, TM09 ... on the yoke, in the middle of the magnet on the lower side, TM11 ... on the yoke (moved 200mm off the connection side end plate), TM12 ... on yoke surface in the middle of magnet.

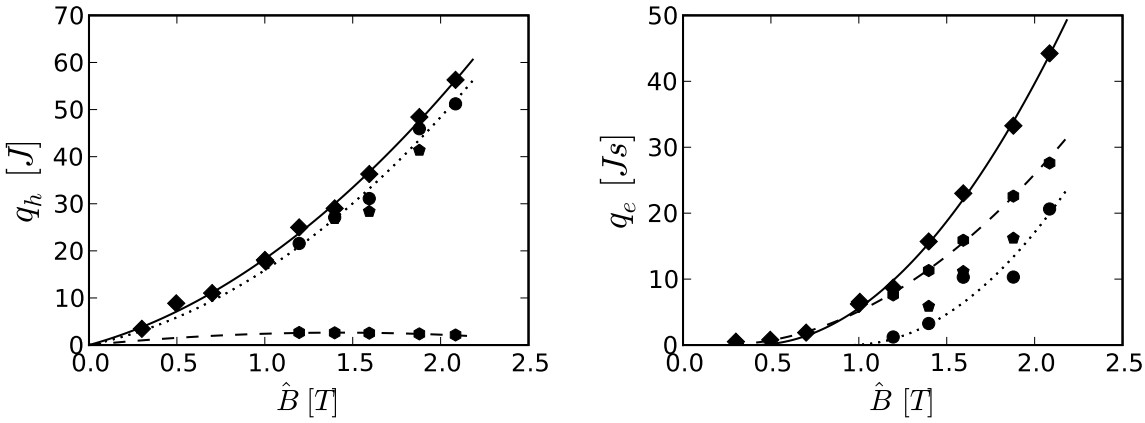

(a) q_h (b) q_e

Figure 6.6: AC loss model parameters. dotted line – magnet, dashed line the – vacuum chamber and solid line – magnet with vacuum chamber.

dissipated power was larger than the maximum cooling power, which is limited by the maximum pressure of < 2.3 bar for the two phase helium flow and by the hydraulic resistance of the magnet's coil. It was found to be close to 45 W and thus in good agreement with the predictions [43]. So delays were added for cycles above this limit (even for the requested originally most intensive cycle "2c" [11]).

In a first step the equivalent dynamic heat load for a pure triangular cycle $P_{\wedge}$ was calculated by scaling the measured average dynamic heat load $\bar{P}$ as well as its measurement error $\Delta\bar{P}$ using

$$P_{\wedge} = \bar{P}\frac{\tau_{cyc}}{\tau_{\wedge}} \quad \tau_{\wedge} = 2B_{max}/\dot{B} \quad \tau_{cyc} = \tau_{\wedge} + t_d \quad \Delta P_{\wedge} = \Delta\bar{P}\frac{\tau_{cyc}}{\tau_{\wedge}}. \tag{6.3}$$

with t_d the used delay, assuming that the measurement is dominated by an absolute measurement error.

The data were then sorted for the different used ramp rates (0.5 - 4 T/s with 0.5 T steps) and were fitted with the function

$$P_{\wedge} = q_h(B_{max})f + q_e(B_{max})f^2 \quad f = 1/\tau_{\wedge} \tag{6.4}$$

to the data $P_{\wedge}$ using $1/\Delta P_{\wedge}$ as weights (see FIGURE 6.6). We found that the linear and quadratic q_h, q_e can be described with sufficient accuracy for all curves with

$$q_h = h_a\, B_{max} + h_b\, B_{max}^2 \qquad q_e = \begin{cases} 0 & B_{max} < B_{th} \\ e_a\,(B_{max} - B_{th})^2 & B_{max} \geq B_{th} \end{cases} \tag{6.5}$$

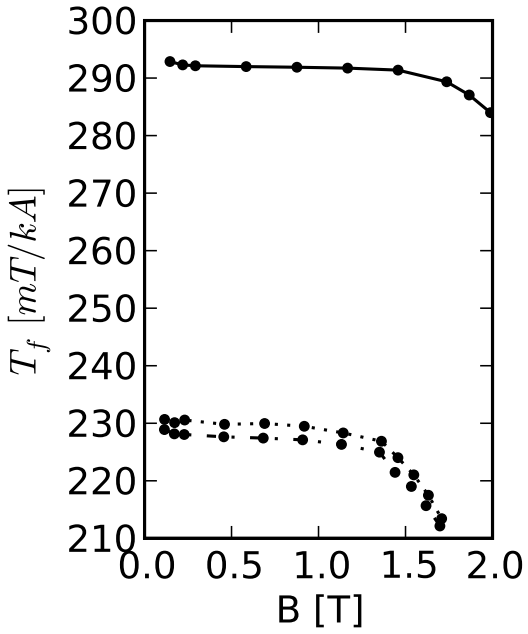

Figure 6.7: The transfer function of the magnet for the centre (solid line) versus the ends (dashed line)

Table 6.2: AC loss model coefficients

Component	h_a	h_b	e_a	B_{th}
Magnet	7.6	8.3	15.5	0.95
Vacuum Chamber	3.7	-1.3	8.0	0.2
Total	10.3	8.3	15.5	0.4

with B_{th} the threshold field (see TABLE 6.2). B_{th} describes that the eddy currents are mainly created in the yoke when the ends start to saturate (also visible in the fall of the transfer functions $t = B/I$ for the ends at around 1.2 T, Fig. 6.7) and thus a field component perpendicular to the lamination is created [22] asserting that the lamination thickness does not influence the eddies for the used frequencies. The average power for an arbitrary cycle can now be calculated with the coefficients by the following procedure. The Q_{max} energy is calculated for a ramp from 0 to the maximum field B_{max} as well as the energy Q_{min} for a ramp from 0 to the minimum field B_{min} for the cycle of interest using the formulae (6.4) - (6.5). The energy of this cycle $Q_c = Q_{max} - Q_{min}$ must now only be divided by the cycle time. The losses for the standard FAIR cycles [11] were estimated (all with $B_{min} \approx 0.25\,T$, see TABLE 6.3) and compared to the separate measurements of the magnet ($\bar{P}_{VI}$ electrical and P_C calorimetric). The location of the temperature sensors listed in table 7.1 is shown in Fig. 6.5. The difference is typically only 2-4 W with the model

Table 6.3: Estimates and Measurements for the FAIR cycles with the flat top time t_f and the cycle frequency f_c. The dissipated average power $\bar{P}$ and the loss per cycle Q is predicted for the whole assembly $\bar{P}_t$, for the vacuum chamber $\bar{P}_v$ and the magnet $\bar{P}_m$. The measured temperatures are given as well ($TM08 \ldots TM12$). TM08 ... coil in the middle of the magnet, on the lower side, TM09 ... on the yoke, in the middle of the magnet on the lower side, TM11 ... on the yoke (moved 200mm off the connection side end plate), TM12 ... on yoke surface in the middle of magnet.

cycle	$B_{max}[T]$	$t_f[s]$	$f_c[Hz]$	$\bar{P}_t[W]$	$Q_t[J]$	$\bar{P}_v[W]$	$Q_v[J]$	$\bar{P}_m[W]$	$Q_m[J]$	$\bar{P}_{VI}[W]$	$\bar{P}_C[W]$	$TM08[K]$	$TM09[K]$	$TM11[K]$	$TM12[K]$
1	1.2	0.1	0.71	26.8	40.4	10.7	15.9	14.6	22.7						
2a	1.2	0.1	0.71	26.8	40.4	10.7	15.9	14.6	22.7	16.4	18.	6.45	7.59	6.42	6.0
2b	0.5	0.1	1.00	4.8	7.8	3.5	4.4	3.6	5.9						
2c	2.0	0.1	0.55	49.1	92.3	14.9	28.1	34.7	65.5						
3a	1.2	1.3	0.38	14.4	40.4	5.8	15.9	7.8	22.7	9	12.	7.28	8.06	7.33	6.9
3b	0.5	1.0	0.53	2.5	7.8	1.8	4.4	1.9	5.9						
3c	2.0	1.7	0.29	26.3	92.3	8.0	28.1	18.6	65.5	23	24.				
4	2.0	0.1	0.20	17.9	92.3	5.4	28.1	12.6	65.5	15	17.	7.67	8.22	7.8	7.3
5	2.0	0.1	0.20	17.9	92.3	5.4	28.1	12.6	65.5						
$/\backslash$	2.1	0	1.05	96.7	101.7	29.4	30.9	69.6	73						

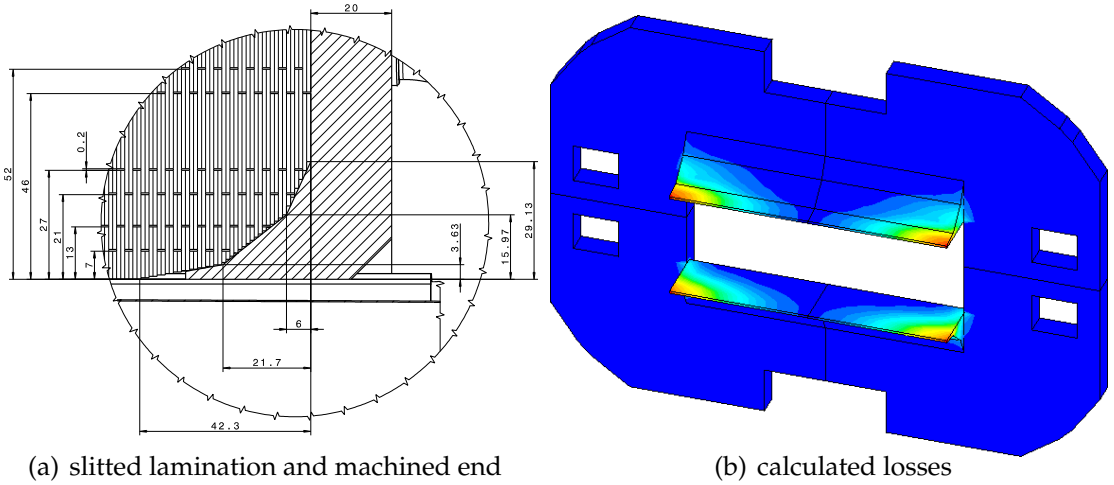

(a) slitted lamination and machined end (b) calculated losses

Figure 6.8: The Rogowsky end profile support structure and losses in the supporting nose of the end plate

estimate offsets comparable to the measurement errors. Cycles with large AC loss permitted to measure the heat removal inside the coil and inside the yoke separately. While the coil loss was measured to be approximately 25 W, data scaled from the measurements of the wire give approximately 15 to 16 W indicating that at this ramp rate the yoke deposes around 10 W into the coil.

6.4.2 Losses in the end profile

The magnet end was chamfered (see Fig. 6.8(a) and the endplate was machined with a "nose" to support these end lamella. As the field penetrates this nose perpendicular additional eddy currents are created leading to significant large AC losses of about 7 W (see Fig. 6.8(b)). So a rectangular end would result in less losses. The field for the CSLD with an rectangular end design was calculated and it was found that the integral field strength varies mainly due to the iron non linearity (see section 5.3 page 58). Therefore the simpler, cost efficient, energy saving rectangular end is favoured by the authors.

6.4.3 Extrapolation to the curved single layer dipole

The following changes are foreseen for the curved single layer dipole:

- The cable will be built of low loss wire [57], which saves $\approx$ 10 W for the triangular cycle $/\backslash$.
- The yoke steel will be made of M600-100 instead of M700-100, which saves around 12 W.
- If the vacuum chamber can be cooled by conduction cooling, the additional losses occurring in the cooling pipes (see section 7.1.1 page 76) can be saved resulting in an additional reduction of $\approx$ 6 W.

Therefore we expect that each single layer dipole requires a cooling power of $\approx$ 75 $\pm$ 5 W, if operated continuously in the cycle $/\backslash$.

Chapter 7

Vacuum chamber and temperature fields

7.1 Vacuum chamber temperature

Given that the surface temperature of the beam pipe is a major issue for the cryopump performance of the vacuum chamber, first calculations were directed to verify that the temperature is below 15 K, a temperature which was estimated to be cold enough to reduce the residual gas pressure to an acceptable limit [58].

7.1.1 Calculated temperature distributions

For the central part of a magnet, the magnetic field and other parameters are typically calculated using a 2D solver (i. e. the part were the magnet's field is independent from the longitudinal coordinate z and thus $B_z = 0$). For calculating the field on the ramp and for the dissipated power the vacuum chamber must be included into the model. The vacuum chamber is made of an elliptical tube with a thickness of 0.3 mm. Ribs, 3 mm thick, soldered to the tube, reinforce it, so that it can withstand the ambient air pressure. Cooling tubes, soldered to the ribs, cool the vacuum chamber surface to support cryopumping. Therefore a small 3D slice (see Fig. 7.1) starting from the middle of a rib to the middle between two ribs was created [59].

The end of the magnet's pole is chamfered to Rogowsky profile and narrow horizontal slits are cut into the laminations in the end to reduce the eddy currents induced by the varying B_z component. Due to these many components of small dimension (compared to the total magnet length of 3m), a short end model was created enforcing $\mathrm{d}B_z/\mathrm{d}z = 0$ as boundary condition, to obtain a model which can be

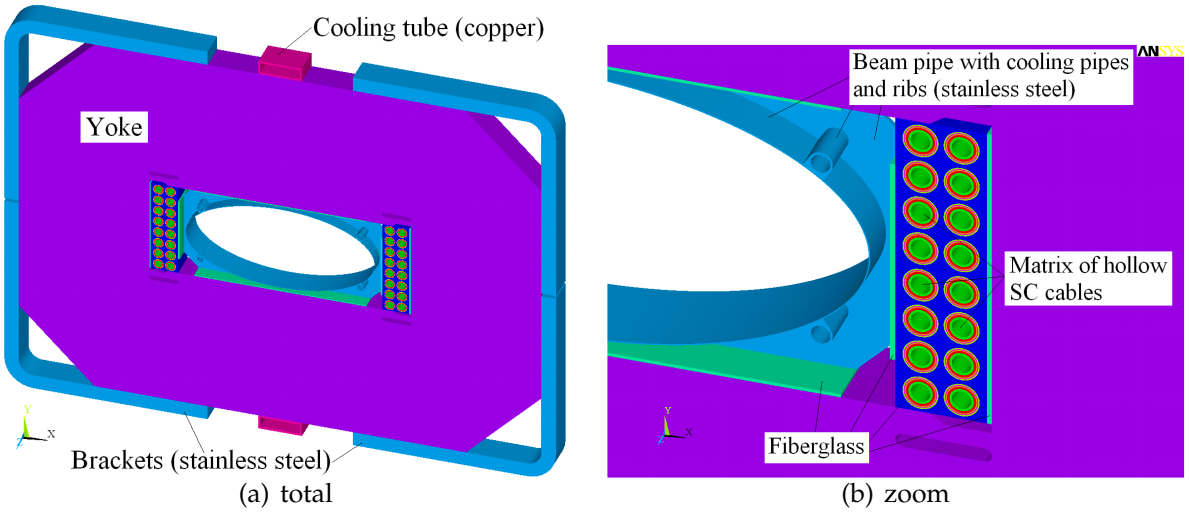

Figure 7.1: The model of the magnet and the vacuum chamber. The model represents the 2D section of the magnet and one full period of the vacuum chamber.

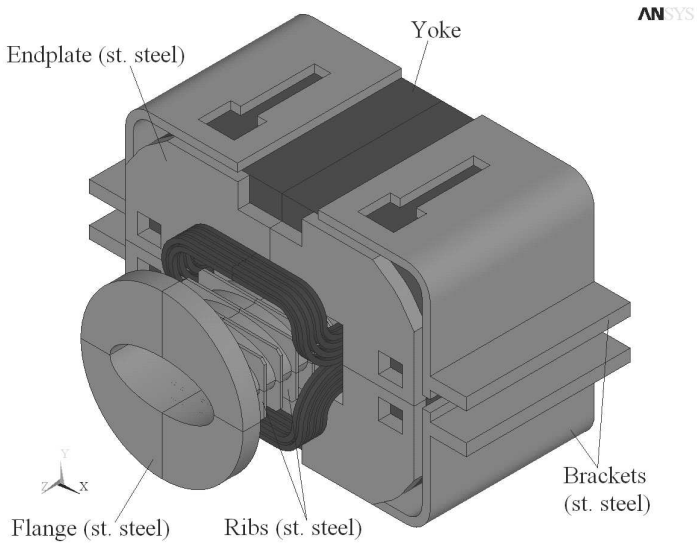

Figure 7.2: The model of the end section of the dipole magnet and the vacuum chamber. The vacuum chamber is supported by ribs. The separate cooling tubes of the yoke were not modelled.

solved within reasonable time (see Fig. 7.2) [22].

The central model was also used to see the impact of the different parts of the vacuum chamber on the cooling (see Fig. 7.3). The top row shows the magnet and vacuum temperatures while the bottom row shows the temperature inside the vacuum chamber along the ellipse. One can see that the left row (vacuum chamber as designed and built by BNG) gives the lowest temperatures while the vacuum chamber temperature only increases by a few Kelvin along the chamber. If the ribs are

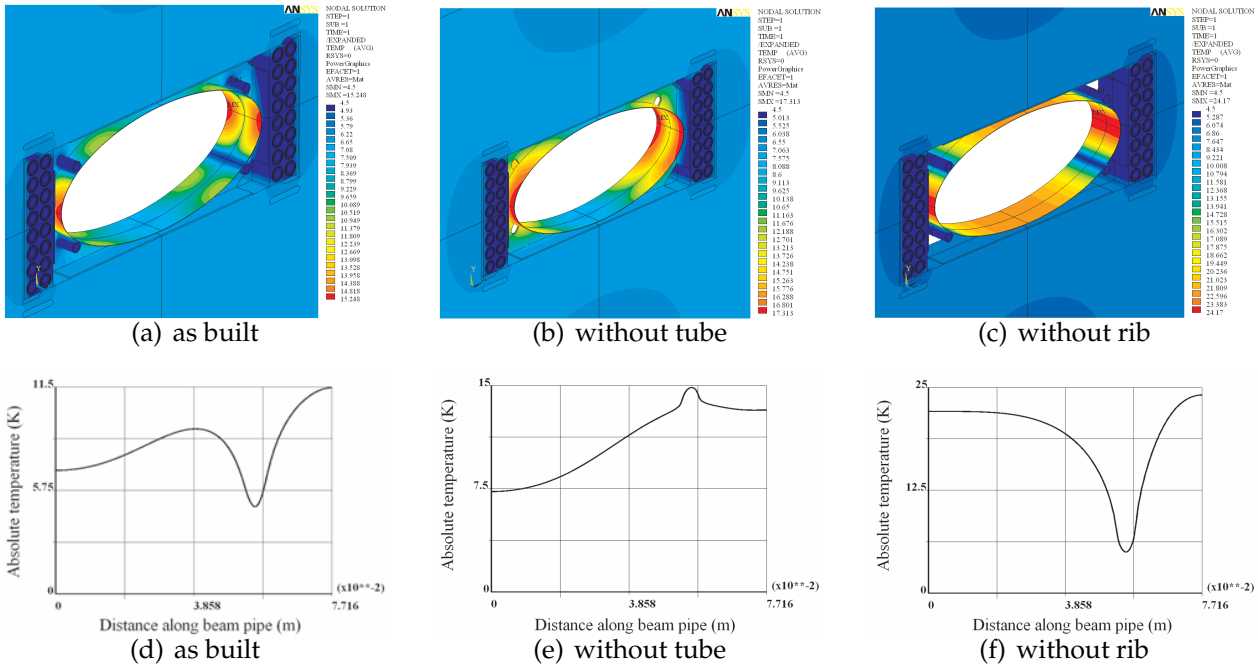

(a) as built (b) without tube (c) without rib

(d) as built (e) without tube (f) without rib

Figure 7.3: Calculated temperatures. The model with the magnet and yoke temperature is shown for the different configurations in the top row. The temperature along the beam pipe (one quater starting from the top (small axis) to the right is shown in the bottom row.

left out the temperature increases even more, indicating that a considerable cooling power is provided over the coil pack as well as over the magnet's yoke, reducing the cooling power available for cooling the magnet itself. The effect of this heat transfer (see Fig. 7.3(b) and 7.3(e)) gives a temperature profile not significantly increased with respect to the temperature field including the effect of the cooling tubes. The power dissipated in the different parts is listed in Table 7.1 with the different cycles listed in Table 7.2. These results strongly depend on the given model. Here an optimal thermal contact between the ribs, yoke and coil via 0.7 mm thick G11 plates was assumed, negelecting the thermal contact resistance.

7.1.2 Measured temperature distributions

The vacuum chamber was inserted into the magnet and the magnet was operated in the different possible FAIR cycles [11] and its loss was measured [8]. The vacuum chamber was also equipped with temperature sensors on the inlet and outlet of the helium flow and on different positions on the chamber. All sensors on the chamber were below the outlet temperature, but close to it and thus only these two are presented in Table 7.2. The measured temperatures are thus close to the ones calculated.

Table 7.1: The calculated average power (in Watts) dissipated in the different components for the different cycles. H – hysteresis loss, E – eddy loss

cycle	2a		2b		2c		/\	
	H	E	H	E	H	E	H	E
magnet central part								
yoke	0.6	0.1	3.6		11.8	0.3	23.7	0.6
magnet end part								
brackets				0.4		0.7		1.2
endplates		1.1		3.3		3.8		8.0
yoke		0.4	0.8	1.5	2.2	3.0	4.0	5.3
beam pipe central part								
pipe		1.7		4.7		6.7		13.9
tubes		0.7		1.9		2.7		5.6
ribs		0.1		0.2		0.3		0.6
beam pipe end part								
pipe		0.3		0.7		0.9		1.9
Total								
magnet								
centre		0.7		3.9		12.2		24.5
end		1.8		6.0		9.7		18.5
coil		6		1		8		16
total		8.5		10.8		29.5		57.0
vacuum chamber								
		2.8		7.6		10.6		22.2
total load								
		11.2		18.4		40.5		79.1

Table 7.2: The temperature of the vacuum chambers for the different FAIR cycles at helium mass flow of 0.1 g/s. B_{min} ... injection field, B_{max} ... maximum field dB/dt ramp rate, t_f ... flat top time (at B_{max}), t_p ... injection time, (at B_{min}), t_c ... cycle time

	B_{min} [T]	B_{max} [T]	dB/dt [T/s]	t_f [s]	t_p [s]	t_c [s]	T_{in} [K]	T_{out} [K]
2a	0.24	1.2	4.0	0.1	0.70	1.408	5.12	15.46
3a	0.24	1.2	4.0	1.3	0.70	2.608	5.09	10.03
3c	0.24	2.0	4.0	1.7	0.68	3.408	5.14	12.66
4	0.24	2.0	4.0	0.1	3.88	5.008	5.09	9.84
2b	0.24	2.0	4.0	0.1	1.	1.4	magnet can not	
2c	0.24	2.0	4.0	0.1	0.7	1.82	be operated	
/\	0	2.0	4.0	0	0	1	in these cycles	

7.2 Impact of the vacuum chamber design on the magnetic field

7.2.1 FEM calculations

The model presented in 7.1.1 also allows calculating the field within the vacuum chamber. The calculations showed that the field is significantly distorted by the eddy currents within the chamber [22]. The distortion is larger than the magnet distortion itself at the injection field of approximately 0.25 T.

All calculations in 7.1.1 were presented for the now tested straight dipole magnet with a double layer coil (S2LD, see also Fig. 2.2). As this magnet can not provide the cycles, finally requested for FAIR, the magnet was redesigned to a curved dipole with a single layer coil (Curved Single Layer Dipole, CSLD) [43, 60]. see Fig. 2.9 page 19). This design was selected as the main dipole for SIS 100 [61]. The same calculations as done with ANSYS were performed using Electra 2D and 3D for the CSLD. The 3D model was similar to the ANSYS model. The difference of the multipoles b_3 and b_5 for the transient field, calculated with ELEKTRA 3D, to the static field, calculated with TOSCA 3D, quite match the ones found for the straight dipole (see Fig. 7.4). In the 2D model the rib was not modelled. The ELEKTRA 2D model predicts smaller distortions (see Fig. 7.4(c) and 7.4(f)) which is to be expected as the eddy currents taking the path over the rib are missing in this calculation. This indicates further that cutting this path can reduce the field distortion considerably.

7.2.2 Analytical model

In the next step towards series production the first single layer magnet for SIS 100 shall be built together with the vacuum chamber [43, 3, 57]. So the authors decided to invest the time to make a model of the vacuum chamber which can be solved semi analytically as it is much faster in evaluation and thus easier to handle to optimise the layout.

The vacuum chamber itself is too complicated to model it in one single formula. But the eddy currents can be seen as flowing in the following loops

1. the tube itself (see figure 7.5(a))

2. two of the 4 cooling pipes short circuited by the rib (see figure 7.5(b))

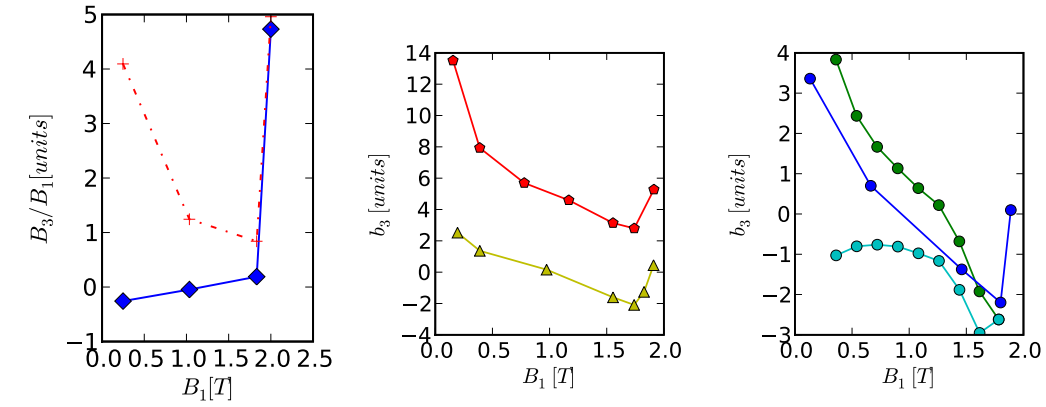

(a) b_3 ANSYS, S2LD (b) b_3 OPERA 3D, CSLD (c) b_3 OPERA 2D, CSLD

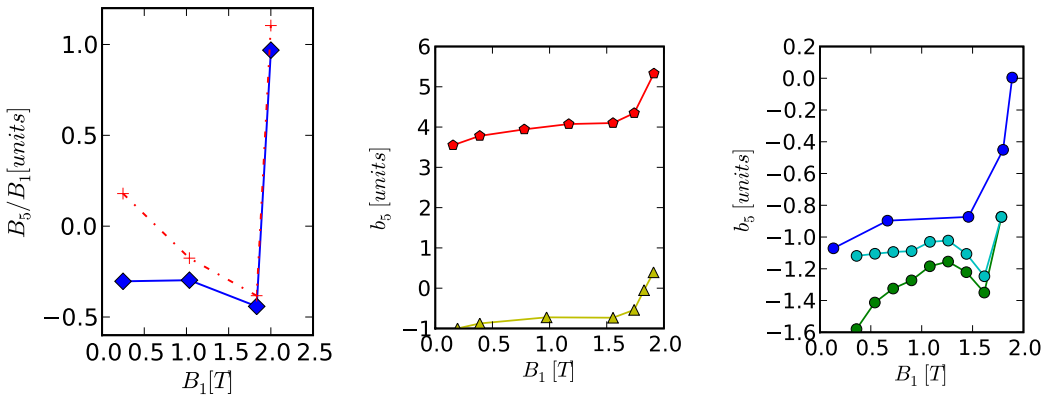

(d) b_5 ANSYS, S2LD (e) b_5 OPERA 3D, CSLD (f) b_5 OPERA 2D, CSLD

Figure 7.4: The effect of the vacuum chamber on the sextupole and dekapole versus the main field for static and transient mode. S2LD with ANSYS: blue – static, red – transient ramp up, CSLD static with TOSCA: blue – 2D, yellow – 3D, CSLD transient with ELEKTRA: green – 2D ramp up, cyan – 2D ramp down, red – 3D ramp up.

3. one cooling pipe electrically connected to the vacuum chamber over the rib (see Fig 7.5(c)).

These calculations are based on the following assumptions:

- the external field is a perfect dipole
- the external field is not disturbed by the eddy currents in the loops
- the specific conductivity σ is uniform throughout the vacuum chamber
- the field penetrates the full chamber as the skin depth $\delta = c/\sqrt{2\pi\sigma\omega}$, $\Delta << a, b, \delta$ (c . . . speed of light, ω . . . $2\ \pi\nu \approx 2\pi$)

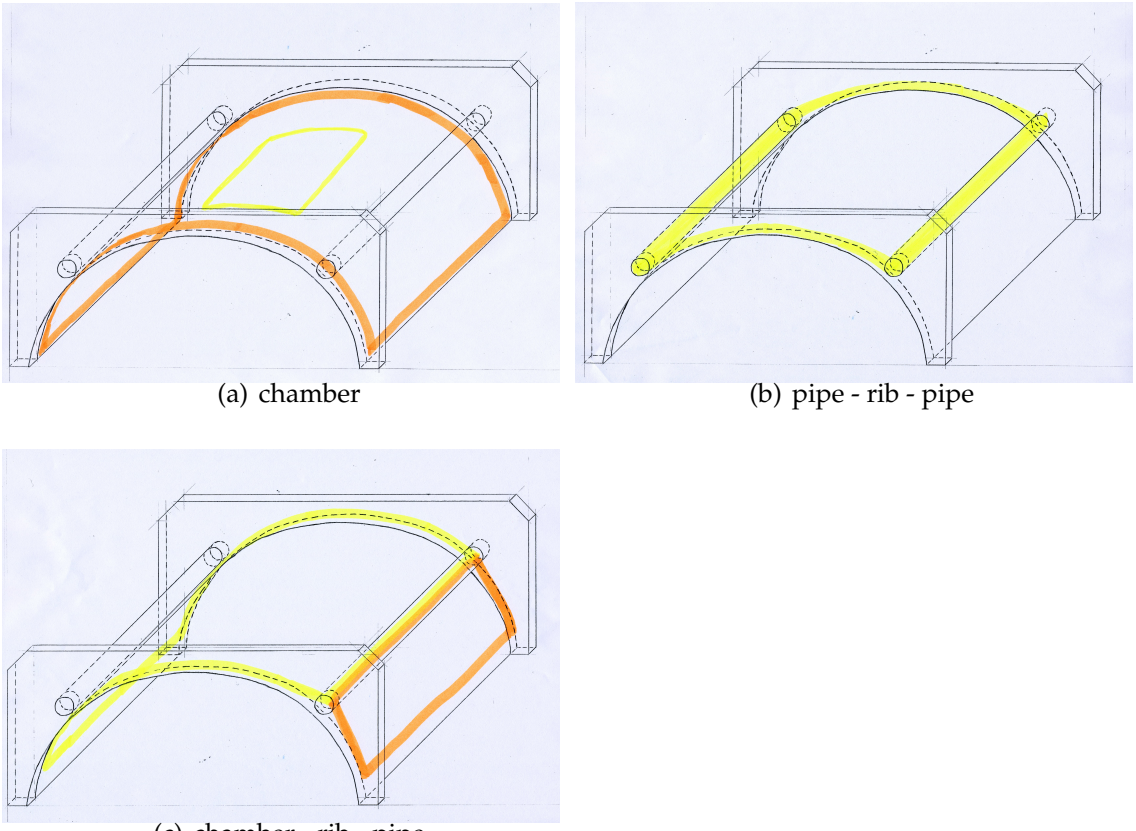

(a) chamber (b) pipe - rib - pipe

(c) chamber - rib - pipe

Figure 7.5: Eddy currents induced in the different loops of the vacuum chamber. These are induced in the elliptic vacuum chamber itself (a), in the ribs shorted by the cooling pipes and in the cooling pipe and the vacuum chamber shorted by the ribs.

Table 7.3: Parameters of the vacuum chamber

Parameter		Value	Dimension
specific conductivity	σ	0.5	$\mu\Omega m$
elliptic tube			
thickness	Δ	0.3	mm
major half axis	a	65	mm
minor half axis	b	30	mm
cooling pipes			
inner radius	r_i	2	mm
outer radius	r_o	3	mm
ribs			
thickness	b	3	mm
distance	l	20	mm

Table 7.4: Resistance of different components and the losses in the 4 cooling pipes.

Part	decay constant τ	current	resistance	$loss_{pipes}$
chamber	22 μs		5 $m\Omega/m$	
tubes	5 μs		27 $m\Omega/m$	
Loop 1		0.1 A	30 $m\Omega/m$	2 mW/m
Loop 2		2.7 A	variable	0.8 W/m
Loop 3		1.7 A	265 $m\Omega/m$	0.3 W/m

7.2.3 Comparison to FEM results

In table 7.4 the eddy current power dissipated in the cooling pipes due to the different loops is $\approx 1.1W$ and roughly 3 W if taking this value for the full magnet length of 2.756 m. This difference could be attributed to the fact that the ANSYS model took solder contacting the pipes and the vacuum chamber into account while the analytical calculations only use the resistance of the cooling pipe.

7.3 Cooling options for the vacuum chamber

The results presented above show that not only the vacuum chamber itself, but in addition its special cooling tubes create large eddy currents if not properly insulated. Furthermore these tubes require their own, extra cooling circuit making the complex cooling scheme of the accelerator more complicated and less reliable.

To avoid these consequences, the vacuum chamber can be cooled indirectly via heat conduction to the cold mass of the magnet, i. e. the iron yoke and the sc coil. The FEM investigations presented in 7.1.1 show that such an design is feasible, if the contact resistance can be neglected using an appropriate technical solution.

First ideas and layouts were presented in [62, 63, 64]. The problems of the chambers impedance characteristics and manufacturing technology still have to be solved. In addition the cooling power of the magnet must be sufficient to deal with the significant heat flow coming from the vacuum chamber too. This is an important, qualitative advantage provided by the recently optimised design version CSLD [45, 43, 60] as the hydraulic resistance of the coil is only a quater of the current magnet's coil for the forced two phase helium flow. An other version of the contact cooling could be a solution similar to that shown in Fig. 7.6 using the stabilising ribs as contact springs.

In any case the optimal beam pipe design minimises the thermal contact resistances between the vacuum chamber and the magnet within the aperture near to

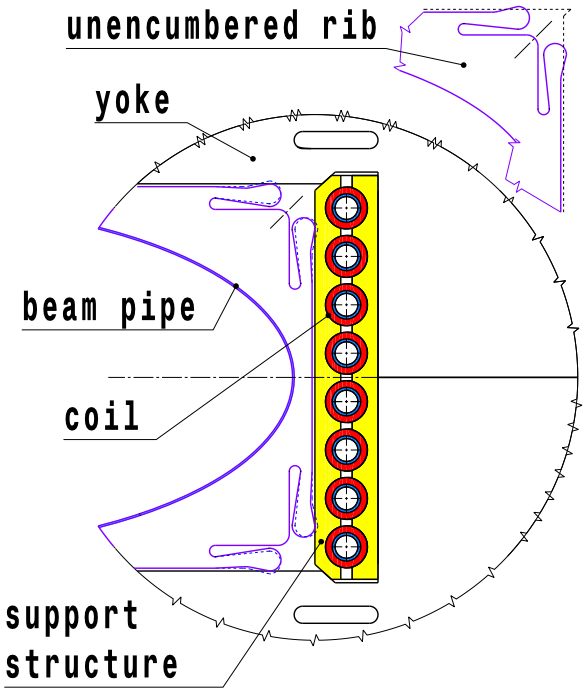

Figure 7.6: The spring rib for contacting the vacuum chamber to the yoke.

the physical limit. The final chamber design must be mechanically stable during the complete life time of the magnet, which has to be carefully analysed too.

7.4 Summary

The sources of losses are well understood and need only to be known to a precision of one Watt. The field quality has to be described with an accurcay of ≈ 100 ppm. Thus further steps are required to backup the calculations.

Taking into account that the field created by the eddy currents induced into the vacuum chamber is small compared to field, created by the magnet, the following further steps are being done

1. The field within the magnet's aperture is measured without the vacuum chamber, which quantifies the accuracy of the calculation.

2. The FEM model is adjusted until it reproduces the measured field with sufficient quality adjusting the BH curve and the measured mechanical properties of the magnet.

3. The vacuum chamber is placed within a conventional magnet of good field quality. Then the field is measured within the vacuum chamber which is now

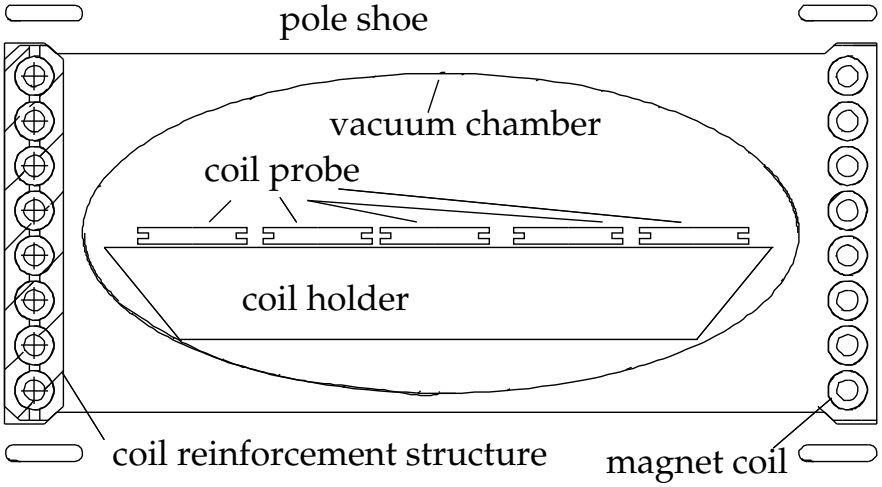

Figure 7.7: The woodlouse within the vaccuum chamber in the magnet.

easily accessible. The conventional SIS 18 magnet available at GSI provides a field of appropriate quality and can be ramped faster than SIS 100 and thus eddy currents with the same strength can be produced thus compensating the change of resistivity of stainless steel, which is roughly 3 time higher at room temperature than at cryogenic temperature.

4. At last the vacuum chamber is installed in the magnet and the field is sampled within the chamber with a "woodlouse" (see Fig. 7.7) at different ramp rates at cryogenic conditions and the quality of the model prediction asserted. These final data provide a reliable field information on a geometric extent not reachable by magnetic field probes with the equipment available to the authors.

Considerable currents are created within the cooling tubes, which disturb the magnetic field. These currents have to be compared to the $\approx 8 \cdot 750A$, which are required for the injection field of $\approx 0.22\,T$. So one gets a ratio between the eddy currents in the tube and the current in the magnet coil of $\approx 7.3 \cdot 10^{-4}$. So an influence is expected and was shown by the FEM calculations.

In a last steps the distortion fields of the different components of the vacuum chamber have to be calculated and compared to the ones obtained with FEM models. Then the cooling layout of the vacuum chamber for the single layer dipole has to be optimized using the analytical formulae and finally crosschecked by a sound ANSYS model as well as by measurements.

Chapter 8

Milestones towards a curved single layer dipole

The now to be built curved single layer dipole builds on a long history of design ideas, calculations and experimental tests. It started with the decision to develop a high current cable, which should be applied for Nuclotron type magnets with larger apertures and higher ramp rates, and which should lower the total AC loss [65].

2002 A first design of a high current cable based on the Nuclotron cable was considered and first test pieces fabricated [66].

2003 Its cooling power was calculated and compared to other proposed cable versions [67, 53]. Strands of the high current cable were tested [68] and designs based on these cable for up to 4 T were made [69].

2004 Based on the high current cable design, a dipole magnet with a single layer coil (thus only half the number of turns), was designed and tested [70, 4, 5]. Further it was shown that the Nuclotron cable can be also built with the conductor in direct contact with helium [71].

The high current Nuclotron type cable was also presented at CERN [72].

2005 A magnet design was made for an aperture of 52 mm radius for fields up to 4 T [73]. Besides the cooling concept of SIS100 was reviewed [74].

2006 The required beam aperture was increased and the pure triangular cycle (1 Hz instead of 0.58 Hz of cycle 2c) was added to the operating cycles.

Calculations of the hydraulic limits showed that the full size magnet will not be able to provide the requested cycles [51]. This year the first full size mag-

nets were to be ordered and thus the magnet design to test was discussed internally. At this occasion the limited cooling capacity of the 2 layer design was reemphasised and it was stressed that the single layer dipole is a solution for this problem [75, 76].

2007 A dedicated test was made at JINR/DUBNA, connecting two model magnets hydraulically in series, which allowed simulating the hydraulic conditions of a full size dipole for SIS100 [77, 52, 60]. Therefore again the single layer dipole was presented as the solution to this problem [43, 45, 10] along with a field design [46, 37], matching the field quality of the 2 layer dipole [78]. Further a quadrupole design was made based on the high current cable for operating cycles of up to 10 Hz [79].

A cable machine was produced by BNG already with flexibility in mind (see also Fig. 2.11 page 21). It can be adapted to the requirements of the high current cable and other modifications [25].

The development of a new wire for the cable of the curved single layer dipole was started within the INTAS framework [80].

2008 The status of the SIS100 magnets, its cooling limits and their solutions were presented at WAMSDO at CERN [1] as well at the Applied Superconductivity Conference [60, 22].

2009 The first measurement results of the double layer straight dipole confirmed the predictions that this magnet design can neither be operated in cycle 2c nor in the triangular cycle [15, 6, 8, 81]. The superconducting wires for the high current cable and short cable pieces were fabricated and their AC losses were measured [82, 83].

So it was finally decided that a single layer dipole shall be ordered and tested.

2010 This report is presented to the machine advisory committee.

Chapter 9

Conclusion

The first SIS100 prototype dipole was intensively tested. The magnet training, the intensive long-term ramping stability, the measured current, the magnetic field characteristics as well as the AC-loss and cooling parameters have proven the preliminary design estimations and show that the applied production technologies are working well and ready for series production. These tests will be completed on a second straight dipole, a curved dipole utilising a two layer coil and on a prototype quadrupole with 6 coil per pole. The results obtained on the first prototype dipole confirm that our methodical design work is correct and the optimised curved single layer dipole is expected to fulfil all operation requirements for the SIS100 accelerator. This curved single layer dipole, while not yet built, is based on a sound R&D conducted over several years (see chapter 8 page 86). The next step toward final series production of the main magnets will be constructing and testing a curved dipole with a single layer coil made of high current superconducting cable.

Chapter 10

Bibliography

[1] E. Fischer, P. Schnizer, A. Akishin, H. Khodzhibagiyan, A. Kovalenko, R. Kurnyshov, P. Shcherbakov, G. Sikler, and W. Walter. Manufacturing of the first full size model of a SIS100 dipole magnet. In *WAMSDO Workshop*, number ISBN 978-92-9083-325-3, pages 147–156. CERN, January 2009.

[2] E. Fischer, R. Kurnishov, and P. Shcherbakov. Finite element calculations on detailed 3D models for the superferric main magnets of the FAIR SIS100 synchrotron. *Cryogenics*, 47:583–594, 2007.

[3] E. Fischer, P. Schnizer, H. Khodzhibagiyan, A. Kovalenko, R. Kurnyshov, P. Akishin, A. Mierau, B. Schnizer, P. Shcherbakov, and K. Sugita. Common design aspects for fast ramped superconducting accelerator magnets. Third Special Workshop on Magnet Simulations for Particle Accelerators, May 2009.

[4] H. G. Khodzhibagiyan, V. Alexeev, S. Averichev, V. Drobin, A. Kovalenko, A. Smirnov, A. Starikov, N. Vladimirova, G. Moritz, E. Fischer, L. Potanina, A. Shikov, and G. Vedernikov. Design and test of a hollow superconducting cable based on keystoned NbTi composite wires. *IEEE T. Appl. Supercond.*, 15(3):1529–1532, June 2005.

[5] A. Kovalenko, N. Agapov, H. Khodzhibagiyan, and A. Smirnov. Design concept of superconducting synchrotron magnets with pulse repetition rate up to 20 hz. *IEEE T. Appl. Supercon*, 15(2):1167–1170, June 2007.

[6] E. Fischer, A. Mierau, P. Schnizer, C. Schroeder, A. Bleile, E. Floch, J. Macavei, A. Stafiniak, F. Walter, G. Sikler, and W. Gärtner. Fast ramped superferric prototype magnets of the FAIR project, first test results and design update. In *PAC 09, Vancouver 2009*, May 2009.

[7] E. Fischer, P. Schnizer, P. Akishin, R. Kurnyshov, A. Mierau, B. Schnizer, and P. Shcherbakov. Measured and calculated field properties of the SIS100 magnets described using elliptic and toroidal multipoles. In *PAC 09, Vancouver 2009*, 2009.

[8] E. Fischer, A. Mierau, P. Schnizer, A. Bleile, W. Gärtner, O. Guymenuk, H. Khodzhibagiyan, C. Schroeder, G. Sikler, and A. Stafiniak. Thermodynamic properties of fast ramped superconducting accelerator magntes for the FAIR project. In *Accepted for publication in Advances in Cryogenic Engineering*, June 2009.

[9] A. Mierau, E. Fischer, P. Schnizer, P. Akishin, R. Kunyshov, B. Schnizer, and P. Shcherbakov. FEM analysis of fast ramped superconducting synchrotron magnets and comparison to experimental results. In *8th International Symposium on Electric and Magnetic Fields*, May 2009.

[10] E. Fischer, P. Schnizer, A. Akishin, R. Kurnyshov, A. Mierau, B. Schnizer, S. Y. Shim, and P. Sherbakov. Superconducting SIS100 prototype magnets design, test results and final design issues. Accepted for publication to IEEE. T. Appl. Supercon, 2009.

[11] P. Schütt. Operation modes of the new accelerator complex for ions and antiprotons. Report on EMAC II, GSI, Darmstadt, October 2003.

[12] P. Spiller. SIS100 system design. Presented at Machine Advisory Comittee, March 2009.

[13] S. Wilfert and K. Keutel. Die kryogenen Vakuumkammern der supraleitenden magnete der SchwerIonenSynchrotron-Ringe SIS 100/300. Technical report, Otto-von-Guericke-Universität, 2004.

[14] H.G. Khodzhibagiyan and A. Smirnov. The concept of a superconducting magnet system for the Nuclotron. In *Proc. of the 12th Int. Cryogen. Eng. Conf. ICIC12*, pages 841–844, 1988.

[15] G. Sikler, W. Gärtner, A. Wessner, E. Fischer, E. Floch, J. Macavei, P. Schnizer, C. Schroeder, F. Walter, and D. Krämer. Fabrication of a prototype of a fast cycling superferric dipole magnet. In *PAC 09, Vancouver 2009*, 2009.

[16] E. Fischer, P. Schnizer, K. Weiss, A. Nyilas, A. Mierau, and G. Sikler. Critical mechanical structure of superconducting high current coils for fast ramped accelerator magnets with high repetition rates in long term operation. In *12 European Conference on Cryogenics and applied superconductivity*. Journal of Physics: Conference Series, september 2009.

[17] A. Kalimov. SIS-100 dipole magnet. Technical report, Gesellschaft für Schwerionenforschung, Planckstrasse 1, 64291 Darmstadt, Germany, February 2007.

[18] E. Fischer, J. Macavei, A. Mierau, and P. Schnizer. The straight SIS100 dipole S2LD. parameters and calculations. Technical report, GSI Helmholtzzentrum für Schwerionenforschung mbH, 2008.

[19] K.P. Weiss and A. Nyilas. Technische Details zu "Spezifikation Mechanische Tests NC-spule". Technical report, Forschungszentrum Karlruhe, April 2007.

[20] K.P. Weiss and A. Nyilas. Messresultate der mechanischen tests an NC-spulen komponenten. Technical report, Forschungszentrum Karlruhe, Germany, October 2006.

[21] E. Bobrov. High cycle fatigue and fracture mechanics evaluations of the conductor for the fast cycling SIS100 synchrotron. Technical report, GSI Helmholtzzentrum fr Schwerionenforschung mbH, 2006.

[22] E. Fischer, P. Schnizer, R. Kurnyshov, B. Schnizer, and P. Shcherbakov. Numerical analysis of the operation parameters of fast cycling superconducing magnets. In *Applied Superconductivity Conference ASC08*, volume 19 of *IEEE Trans. On Appl. Supercon.*, pages 1266–1267, June 2009.

[23] R. Kurnyshov, P. Shcherbakov, and E. Fischer. Report on finite element r&d. Technical report, Elektroplant Moscow, December 2007.

[24] G. Moritz, E. Fischer, H. Khodzhibagiyan, A. Kovalenko, A. Nyilas, R. Burgmer, D. Krischel, W. Schmidt, P. Gärtner, M. Gehring, W. Walter, and A. Wessner. Mechanical coil structure of the FAIR SIS100 magnets. *IEEE Trans. Appl. Supercond.*, 17(2):1169– 1172, 2007.

[25] G. Sikler et al. Full size model manufacturing and advanced design status of the SIS100 main magnets. WAMSDO at CERN, June 2008.

[26] A. Nyilas, A. Portone, and C. Sborchia. "cryogenic investigations on cyclic properties of type 316LN and incoloy 908 alloys for superconducting magnet applications. In *Fatique 2002*, volume 4, pages 2581–2586, 2002.

[27] P. Shcherbakov, E. Fischer, P. Schnizer, and A. Mierau. Electrosteel for fast ramped superconducting magnets. Technical report, Institute for High Energy Physics, to be published.

[28] C. B. Rasmussen. *Iron Losses and Material Properties of Soft Magnetic Materials for Use in Electrical Machines.*

[29] F. Harfoush et al. The design of large aperture high field dipole. Technical Memorandum, FNAL, Dec 1989.

[30] Druzhinin V.V. *Magnetic properties of electric steels*. Energy, 2 edition, 1974.

[31] Fabbricatore P. Steel choice. presentation, May 2007.

[32] Japan book on steel.

[33] P. Shcherbakov, E. Fischer, P. Schnizer, and M. Mierau. Electrosteel for fast ramped superconducting magnets. Technical report, Institute for High Energy Physics, Protvino, Russia, 2010.

[34] I. Bogdanov, S. Kozub, P. Shcherbakov, and L. Tkachenko. Study of magnetic properties of steels for iron yoke of SIS-100 and 300 dipoles. Technical report, Institute for High Energy Physics, Protvino, Russia, 2004.

[35] I. Bogdanov, S. Kozub, P. Shcherbakov, L. Tkachenko, E. Fischer, F. Klos, G. Moritz, and C. Muehle. Study of electrical steel magnetic properties for fast cycling magnets of sis100 and sis300 rings. In *The proceedings of EPAC 2004, Lucerne Switzerland*.

[36] P. Schnizer, B. Schnizer, P. Akishin, and E. Fischer. Field representation for elliptic apertures. Technical report, Gesellschaft für Schwerionenforschung mbH, Planckstraße 1, D-64291 Darmstadt, February 2007.

[37] P. Schnizer, B. Schnizer, P. Akishin, and E. Fischer. Magnetic field analysis for superferric accelerator magnets using elliptic multipoles and its advantages. In *The 20^{th} international conference on magnet technology*, volume 18 of *IEEE Trans. Appl. Supercon.*, pages 1605–1608, June 2008.

[38] P. Schnizer, B. Schnizer, P. Akishin, and E. Fischer. Field representation for elliptic apertures. Technical report, Gesellschaft für Schwerionenforschung mbH, Planckstraße 1, D-64291 Darmstadt, January 2008.

[39] P. Schnizer, B. Schnizer, P. Akishin, and E. Fischer. Theoretical field analysis for superferric accelerator magnets using plane elliptic or toroidal multipoles and its advantages. In *The 11^{th} European Particle Accelerator Conference*, pages 1773 – 1775, June 2008.

[40] P. Schnizer, B. Schnizer, P. Akishin, and E. Fischer. Plane elliptic or toroidal multipole expansions within the gap of straight or curved accelerator magnets. In *13^{th} International IGTE Symposium*. Institut für Grundlagen und Theorie der Elektrotechnik, Technische Universität Graz, Austria, September 2008.

[41] P. Schnizer, B. Schnizer, P. Akishin, and E. Fischer. Theory and application of plane elliptic multipoles for static magnetic fields. *Nuclear Instruments and Methods in Physics Research Section A: Accelerators, Spectrometers, Detectors and Associated Equipment*, 607(3):505 – 516, 2009.

[42] P. Schnizer, B. Schnizer, P. Akishin, and E. Fischer. Plane elliptic or toroidal multipole expansions for static fields. applications within the gap of straight and curved accelerator magnets. *The International Journal for Computation and Mathematics in Electrical Engineering (COMPEL)*, 28(4), 2009.

[43] Egbert Fischer, Hamlet Khodzhibagiyan, and Alexander Kovalenko. Full size model magnets for the FAIR SIS100 synchrotron. In *The 20^{th} international conference on magnet technology*, volume 18 of *IEEE Trans. Appl. Supercon.*, pages 260–263. IEEE, June 2008.

[44] E. Fischer, H. Khodzhibagiyan, and A. Kovalenko. SIS100: Magnet design options to minimize the energy losses, investment and operation costs. GSI Internal Note, August 2006.

[45] E. Fischer and H. Khodzhibagiyan. SIS100 dipole alternatives. GSI FMT Internal Note, June 2007.

[46] P. Akishin, E. Fischer, and P. Schnizer. A single layer dipole for SIS100. Technical report, Gesellschaft für Schwerionenforschung mbH, Planckstraße 1, D-64291 Darmstadt, July 2007.

[47] P. Schnizer, H. R. Kiesewetter, T. Mack, T. Knapp, F. Klos, M. Manderla, S. Rauch, M. Schöncker, and R. Werkmann. Mole for measuring pulsed superconducting magnets. In *The 20th international conference on magnet technology*, volume 18 of *IEEE Trans. Appl. Supercon.*, pages 1648–1651, June 2008.

[48] P. Schnizer, E. Fischer, H. Kiesewetter, F. Klos, T. Knapp, T. Mack, A. Mierau, and B. Schnizer. Commissioning of the mole for measuring SIS100 magnets and first test results. Accepted for publication in IEEE. T. Appl. Supercon, 2009.

[49] A. Kovalenko, N. Agapov, E. Fischer, H. Khodzhibagiyan, G. Kuznetsov, G. Moritz, and A. Smirnov. New results on minimizing AC power losses in a fast cycling 2T superferric dipole with a cold yoke. *IEEE Trans. Appl. Supercond.*, 16(2):338–341, 2006.

[50] European advanced superconductor. http://www.advancedsupercon.com.

[51] E. Fischer, H.G. Khodzhibagiyan, and A Kovalenko. SIS100 dipole cooling limits. Internal Note, May 2007.

[52] E. Fischer. FAIR: SIS100 synchrotron R&D status main magnets and full length models. miniTAC sc Magnets and Cryogenics, May 2007.

[53] H.G. Khodzhibagiyan, A. Kovalenko, and E. Fischer. Some aspects of cable design for fast cycling superconducting synchrotron magnets. *IEEE Trans. Appl. Supercond.*, 14(2):1031–1034, 2004.

[54] N.N Agapov, E.I. D'yachkov, H.G Khodzhibagiyan, V.V. Krylov, Yu.V. Kulikov, E.K. Kuryatnikov, V. N. Kuzichev, L. G. Makarov, P.I. Nikitaev, N. M. Sazonov, A. A. Smirnov, V. V. Stekol'shchikov, and A. G. Zel'dovich. A pulsed dipole magnet made from a hollow composite superconductor with a circulatory refrigeration system. *Cryogenics*, pages 345–348, June 1980.

[55] P. Schnizer, P. Akishin, E. Fischer, T. Knapp, H.R. Kiesewetter, P. Kurnyshov, T. Mack, G. Sickler, B. Schnizer, P. Shcherbakov, and W. Walter. Superferric rapidly cycling magnets: optimized field design and measurement. In *WAMSDO Workshop*, number ISBN 978-92-9083-325-3, pages 189–196. CERN, January 2009.

[56] P. Schnizer, P. Akishin, E. Fischer, R. Kurnyshov, P. Shcherbakov, G. Sikler, and W. Walter. Magnetic field characteristics of a SIS100 full size dipole. In *The 11th European Particle Accelerator Conference*, pages 2452–2454, June 2008.

[57] H. Khodzhibagiyan et al. Design and study of new cables for superconducting accelerator magnets: Synchrotron SIS100 at GSI and NICA collider at JINR. Presented at EUCAS09, September 2009.

[58] E. Fischer, P. Schnizer, C. Heil, A. Mierau, B. Schnizer, and S. Shim. Impact of the beam pipe design on the operation parameters of the superconducting magnets for the SIS100 synchrotron of the FAIR project. In *12 European Conference on Cryogenics and applied superconductivity*. Journal of Physics: Conference Series, september 2009.

[59] E. Fischer, R. Kurnishov, and P. Shcherbakov. Analysis of coupled electromagnetic-thermal effects in superconducting accelerator magnets. In *8th European Conference On Applied Superconductivity, 16 - 20 September 2007, Brussels, Belgium*, volume 97. IOP Journal of Physics: Conference Series, 2008.

[60] E. Fischer, H. Khodzhibagiyan, A. Kovalenko, and P. Schnizer. Fast ramped superferric prototypes and conclusions for the final design of the SIS100 main magnets. In *Applied Superconductivity Conference ASC08*, volume 19 of *IEEE Trans. On Appl. Supercon.*, pages 1087–1091, June 2009.

[61] FAIR - Facility for Antiprotons and Ion Research, Technical Design Report, Synchrotron SIS100, December 2008.

[62] E. Fischer and H. Khodzhibagiyan. An alternative design for the SIS100 vacuum chamber. Technical report, GSI Helmholtzzentrum für Schwerionenforschung mbH, Planckstraße 64291 Damstadt, Germany, august 2006.

[63] G. Sikler. Alternatives Design für das Vakuumstrahlrohr für SIS100. Technical report, Babcock Noell GmbH, Alfred Nobel Str. 20, 97080 Würzburg, Germany, December 2007.

[64] E. Fischer, K. Macavei, and A. Mierau. Designkonzept für eine Vakuumkammer mit Kontaktkühlung. GSI MT Internal Note: MT-INT-EF-2009-001, October 2009.

[65] E. Fischer, H. Khodzhibagiyan, and A. Kovalenko. Private Communication at Dubna, March 2002.

[66] H. Khodzhibagiyan, V. Alexeev, S. Averichev, V. Drobin, A. Kovalenko, A. Smirnov, A. Starikov, N. Vladimirova, G. Moritz, E. Fischer, L. Potanina, A. Shikov, and G. Vedernikov. Design of new hollow superconducting nbti cables for fast cycling synchrotron magnets. *IEEE Trans.Appl.Supercond.*, 13(2):3370–3373, 2003.

[67] H. Khodzhibagiyan, A. Kovalenko, and E. Fischer. Nuclotron cable and CICC cooling condition analysis. Presented at the NCICC meeting, June 2003.

[68] H. Khodzhibagiyan, A. Kovalenko, A. Agapov, V. Alexeev, V. Drobin, A. Starikov, Yu. Shishov, N. Vladimirova, G. Moritz, E. Fischer, L. Potanina, A. Shikov, G. Vedernikov, and A. Kalimov. Design and test of new hollow high current NbTi cable for fast ramped synchrotron magnets. In *The 6th European Conference on Applied Superconductivity (EUCAS 2003)*, number 181 in Conference Series. Institute of Physics, 2004.

[69] A. Kovalenko, N. Agapov, P. Akshin, A. Butenko, H. Khodzhibagiyan, and V. Mikhailov. Fast cycling 4T dipole magnet based on a hollow high current superconducting NbTi cable. In *The 6th European Conference on Applied Superconductivity (EUCAS 2003)*, number 181 in Conference Series. Institute of Physics, 2004.

[70] E. Fischer, P. Akishin, H. Khodzhibagiyan, A. Kovalenko, G. Kuznetsov, G. Moritz, and A. Smirnov. Minimization of AC power losses in fast cycling window frame 2T superferric magnets with the yoke at T = 4.5 K. presented at ASC 2004, 2004.

[71] E. Fischer, H. Khodzhibagiyan, A. Kovalenko, and G. Moritz. EU-patent Nr. 04009730.5, April 2004.

[72] P. Schnizer et al. Fast ramped superconducting magnets. EDMS document number: 493476 http://edms.cern.ch, 2004.

[73] H. Khodzhibagiyan et al. Progress in the design of a fast-cycling cos-style dipole based on high current hollow superconducting cable. *Journal of Physics: Conference Series*, 43:731–734, 2006.

[74] H.G. Khodzhibagiyan, E. Fischer, and A.D. Kovalenko. New design for the SIS100/300 magnet cooling. *IEEE T. Appl. Supercon.*, 16:411 – 414, 2006.

[75] Egbert Fischer, A. Alfeev, H. Khodzhibagiyan, A. Kovalenko, G. Kuznetsov, G. Moritz, V. Seleznev, and A. Kalimov. Status of the design of a full length superferric dipole and quadrupole magnets for the FAIR SIS100 synchrotron. In *Applied Superconductivity Conference 2006*, volume 17, pages 1078–1082, 2007.

[76] E. Fischer, H. Khodzhibagiyan, and A. Kovalenko. FAIR SIS100 synchrotron status of the design for full length superferric main magnets. Presented at the Internal Review on SIS100 Magnets, October 2006.

[77] Report on research and development contract no. 6 between GSI and JINR Dubna, March 2006.

[78] FAIR baseline technical report. GSI, Darmstadt, Germany, 2006.

[79] H.G. Khodzhibagiyan, N.N. Agapov, V.D. Bartenev, V.M. Drobin, E. Fischer, A.D. Kovalenko, G.L. Kuznetsov, P.I. Nikitaev, L.V. Potanina, A.K. Shikov, A.Yu. Starikov, G.P. Vedernikov, and N.M. Vladimirova. Superferric quadrupole magnet with a pulse repetition rate of 10 hz for high energy particle accelerators. *IEEE T. Appl. Supercon*, 17(2):1181–1184, June 2007.

[80] wire and cable tasks. Minutes of the INTAS Meeting, June 2007.

[81] E. Fischer, P. Schnizer, K. Sugita, P. Akishin, F. Klos, R. Kurnyshov, A. Mierau, B. Schnizer, and P. Shcherbakov. Magnets and magnet R&D status for SIS100. Presented to the machine advisory committee, March 2009.

[82] V. Pantsyrny. Research and development of new design superconducting NbTi wire with low AC losses intended for use in magnet systems of SIS100 and SIS300 synchrotrons of the FAIR accelerator facility. Presented at the INTAS meeting at GSI, June 2009.

[83] L. Potanina, V. Pantsyrny, N. Shikov, A. Salunin, I. Gubkin, V. Korpusov, H. Khodzhibagiyan, A. Kovalenko, E. Fischer, H. Mueller, and G. Moritz. Experimental results on the development of superconducting NbTi/Cu-Mn/Cu wires for magnet systems of SIS100 and SIS300 synchrotrons of fair. *Submitted to IEEE T. Appl. Supercon.*, 2009.

11 List of Figures

12 List of Tables